Простая физика магнитной турбулентности в бесстолкновительной плазме: ударные волны, солнечные вспышки, лазерная абляция

Кочаровский Вл.В.[1], Гарасёв М.А.[1], Емельянов Н.А.[1], Кузнецов А.А.[1], Нечаев А.А.[1], Кочаровский В.В.[1,2]

[1]*Институт прикладной физики РАН, Нижний Новгород, Россия*
[2]*Department of Physics and Astronomy, Texas A&M University, College Station, USA*

Лекция посвящена неравновесным явлениям в анизотропной плазме, связанным с филаментацией токов и генерацией сильных магнитных полей в процессе распада сильных разрывов и/или инжекции высокоэнергичных частиц при наличии неоднородной фоновой плазмы и внешнего магнитного поля.

Namely, we describe transient quasi-magnetostatic structures of the multi-scale z-pinches and current sheets with various orientations, produced by the Weibel-type instabilities in a plasma with hot electrons.

Relativistic shock model of Gamma-Ray Bursts

(an extremely non-equilibrium anisotropic collisionless plasma with a long-living turbulent magnetic field)

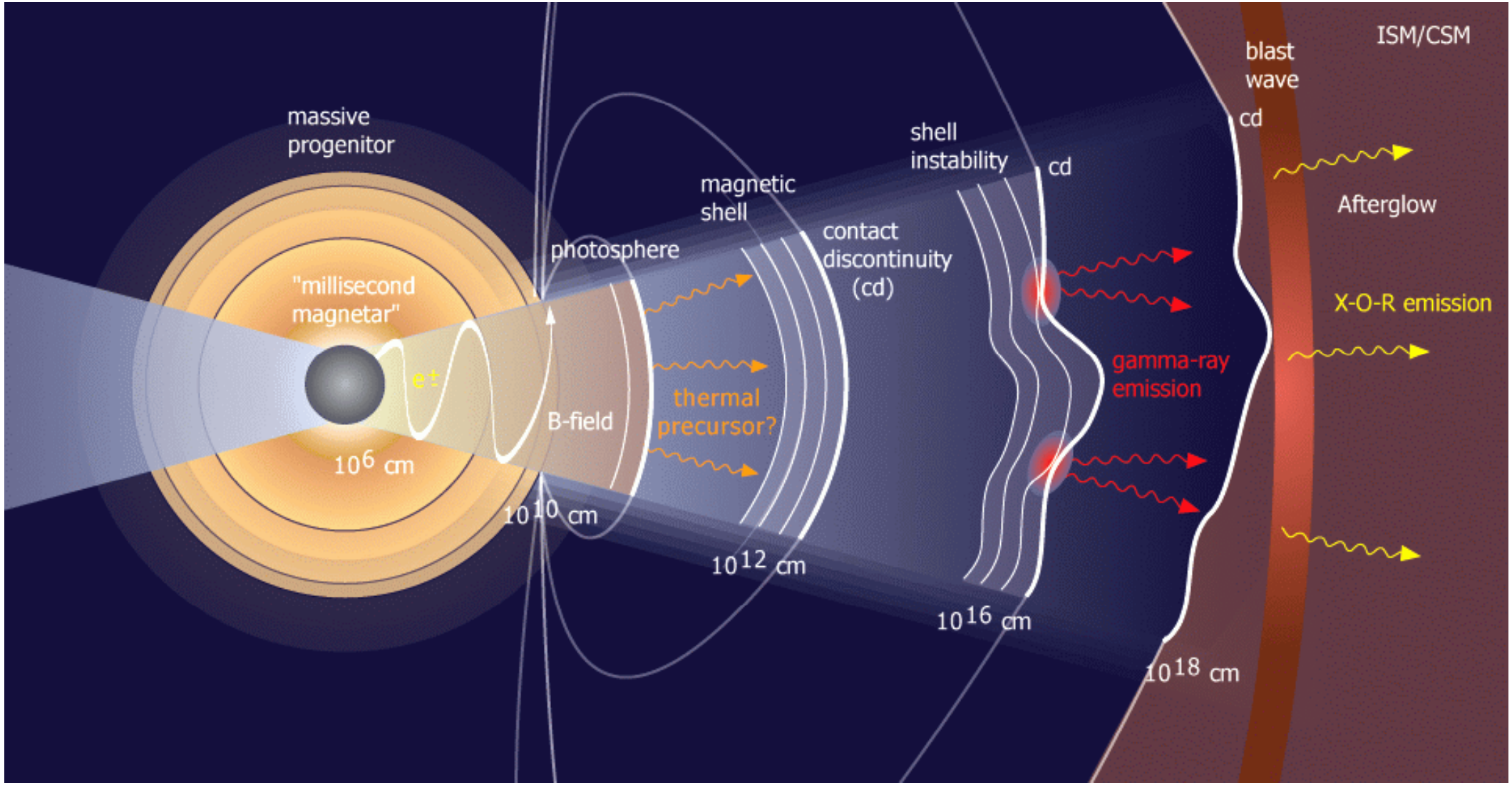

From Wikipedia

Collisionless shock waves in plasma

Strong discontinuity decay in plasma. Weibel-type instabilities.
Weak discontinuity decay: the role of dispersion, nonlinearity and dissipation; superposition of solitons is responsible for the shock-front formation.
The kinetic instabilities, overturning phenomena and turbulence in plasma.

См. Л.А.Арцимович, Р.З.Сагдеев «Физика плазмы для физиков», 1979; Ю.В.Медведев «Нелинейные явления при распадах разрывов в разреженной плазме», 2012.

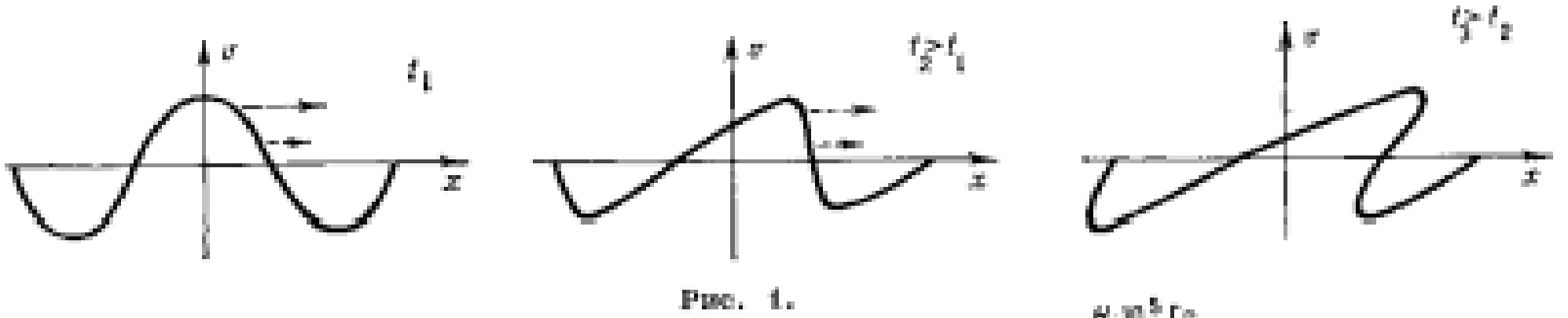

Рис. 1.

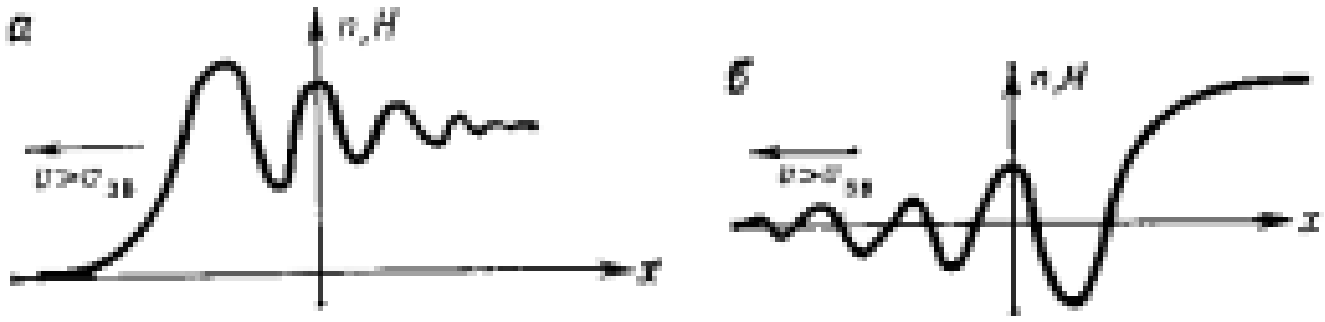

Рис. 2.

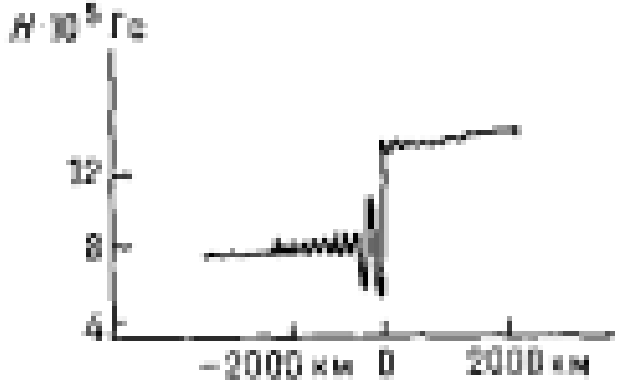

Рис. 3.

Negative dispersion, “ion sound”. Positive dispersion, “magnetic sound”.

The problem of formation and dynamics of the multi-scale magnetic field

Example: *What is its role in the collisionless shock waves and relativistic jets?*

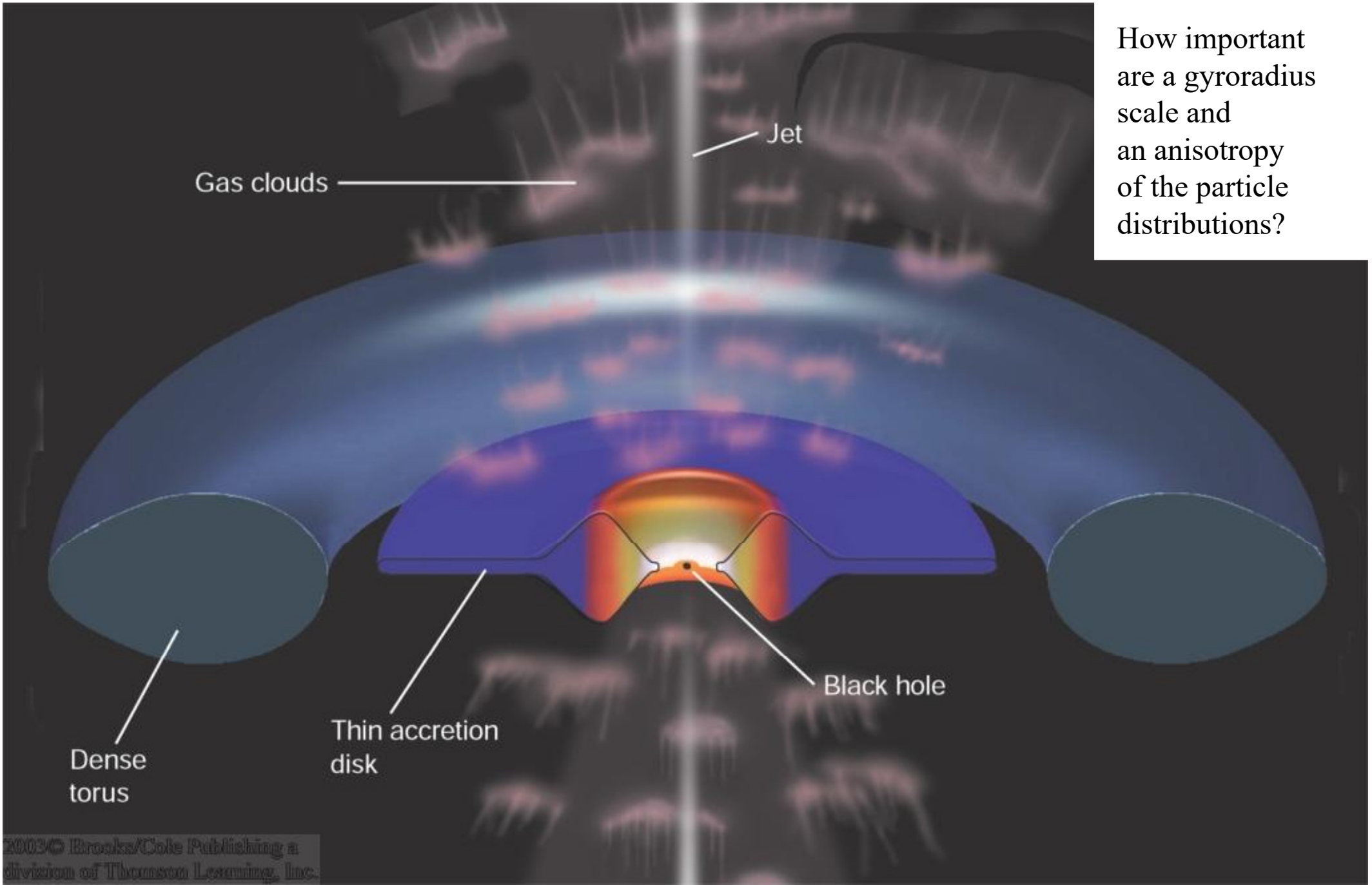

How important are a gyroradius scale and an anisotropy of the particle distributions?

Plasma discontinuity decay and various Weibel-type instabilities due to transient hot-electron flows in *different geometries*

An anisotropic collisionless plasma cloud with hot electrons expands into an inhomogeneous background plasma with an external magnetic field:

(i) a circular or cylindrical form of a hot-electron spot in the cases of an initial-value problem or a finite-time injection of electrons from a target surface,

(ii) inhomogeneous layers of cold background plasma of different densities with a small or large spatial scale,

(iii) an external magnetic field with three orientations: perpendicular to the target or along its surface and directed either across or parallel to the long axis of the hot-electron spot.

For various combinations of the attributes (i)–(iii), we find dynamical regimes of the Weibel-type instabilities related to different types of the anisotropic electron velocity distribution. We discuss applications of the obtained results to laser plasmas as well as space and astrophysical plasmas. ***Simple physics is the small-scale filamentation of the electron-ion currents accompanied by the quasi-magnetostatic, quasi-linear turbulence.***

What is a role of Weibel instability in the non-MHD dynamics of a multi-scale magnetic field in a collisionless anisotropic inhomogeneous plasma? Some answers are expected from the laser-plasma experiments and the long-term PIC-simulations of typical simple problems.

From Wikipedia

See, e.g., A.Balogh, R.A.Treumann "Physics of collisionless shocks", 2013;
A.Marcowith *et al.* 2016 *Rep. Prog. Phys.* **79** 046901 (microphysics of shock waves).

Selected physical problems and new phenomena in a collisionless anisotropic magnetoactive plasma

1. **An electron-ion Weibel instability** and dynamics of the spatial spectra of a turbulent magnetic field and a self-consistent current density.

2. **A quasi-electrostatic shock** accompanied by, first, a plasma density bump formation and, second, a magnetic field generation due to hot electrons.

3. **The coexistence of orthogonal current structures** and the development of different-type Weibel instabilities in adjacent regions of a plasma transition layer with a hot electron flow.

4. A decay of a strong elongated quasi-one-dimensional discontinuity in a plasma with hot electrons in **the presence of an external magnetic field**.

5. **Weibel-instability mechanism of a solar (stellar) flare**: analytical results for the growth rate and the particle-in-cell (PIC) modeling of the nonlinear modification of a coronal-loop magnetic field.

3D3V PIC-simulations, EPOCH code

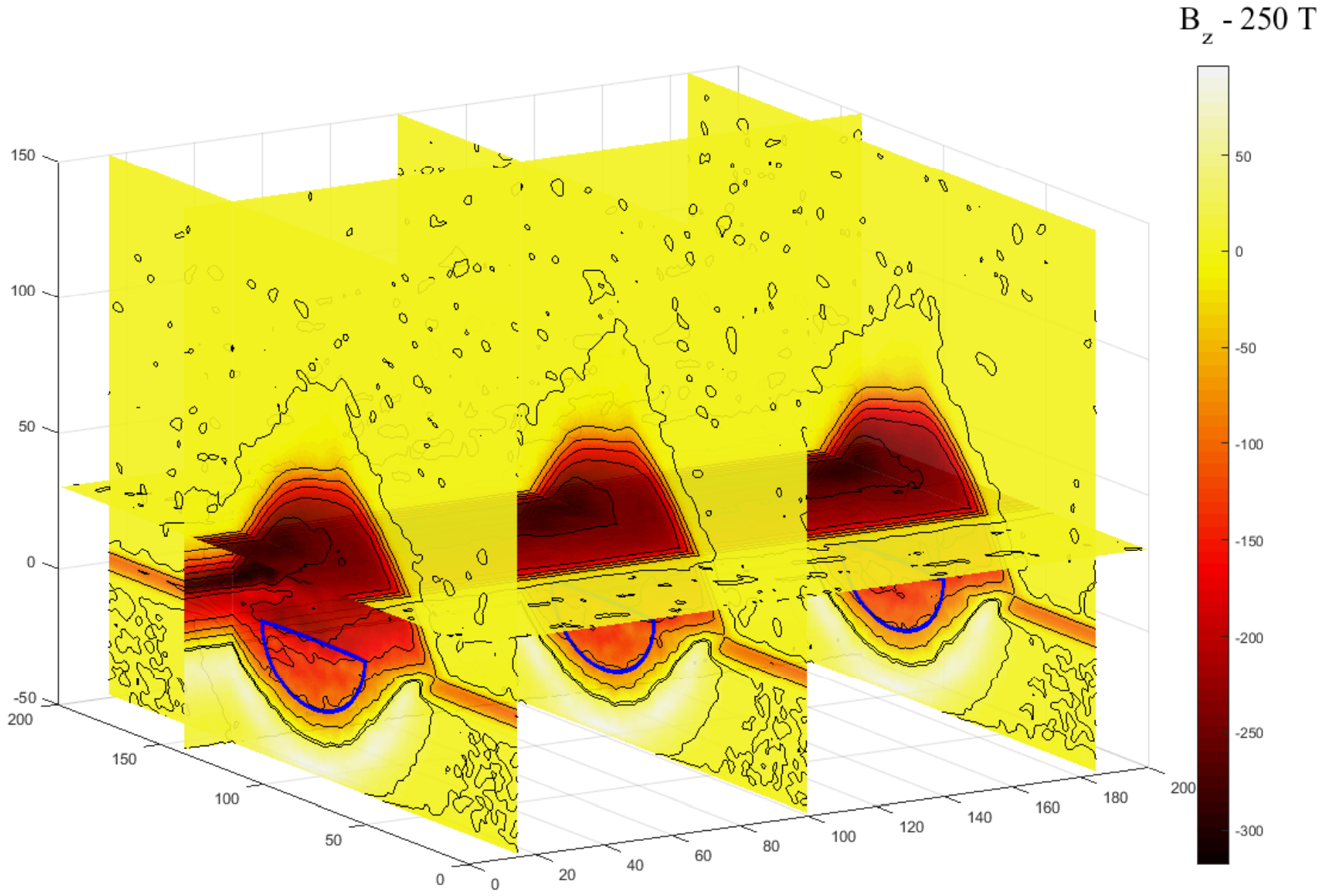

Z-component of the magnetic field generated by the expansion of plasma with hot electrons at t=3 ps.

1. An electron-ion Weibel instability and dynamics of the spatial spectra of a turbulent magnetic field and a self-consistent current density

Let us focus on an evolution of separate spatial harmonics and the whole spatial spectrum of a current density (or a magnetic field), and then discuss kinetics of various particle species.

We assume that **the energy densities of the electrons and the ions (protons) are the same**. For example, it is possible in the stellar (solar) winds.

We began this analysis 5 years ago, see Borodachev L.V., Garasev M.A., Kolomiets D.O., Kocharovsky V.V. et al., *Radiophys. Quant. Electron.* 59 (12), 991 (2017). Although there are a lot of numerical modeling of the turbulent plasma processes, "**despite years of study, an accurate theoretical description of these effects is still lacking**" according to F. Pecora et al. Ion Diffusion and Acceleration in Plasma Turbulence, 2018 (arXiv 1803.09647v1). Sere also D. Perrone, S. Servidio et al. Coherent Structures at Ion Scales in Fast Solar Wind: Cluster Observations, 2017 (ApJ 849: 49), 2017 (PRL 119: 205101), 2018 (Phys. Plasmas 25: 060704) ; A. Stockem Novo, P. H. Yoon et al. Quasilinear saturation of the aperiodic ordinary mode streaming instability, 2015 (Phys. Plasmas 22: 092301; 22: 082122), 2017 (Rev. Mod. Plasma Phys. 1: 4).; etc.

Here, we restrict ourselves with a simplest initial value problem for a homogeneous plasma with **equal strong anisotropy degrees of the distributions of both electrons and protons**.

Initial value problem for the Weibel instability

$$f_\alpha = \frac{m_\alpha^{3/2}}{(2\pi)^{3/2} T_{\perp\alpha} T_{\parallel\alpha}^{1/2}} \exp\left[- \frac{m_\alpha (v_x^2 + v_y^2)}{2T_{\perp\alpha}} - \frac{m_\alpha v_z^2}{2T_{\parallel\alpha}} \right]$$

$A_\alpha = T_{\parallel\alpha}/T_{\perp\alpha} - 1 > 0$ — an anisotropy degree ($A_\alpha \sim 1 - 10$).

For details see a review paper V.Kocharovsky et al. Phys. Uspekhi **59**, 1165 (2016);
L.Borodachev, V.Kocharovsky et al. Radiophysics and Quantum Electronics **59**, 991 (2017).

$B_{x,y} \sim \exp\left(i\vec{k}\vec{r} - i\omega t\right)$

$\vec{k}_\perp = \{k_x, k_y\}$

$$\frac{\partial f_\alpha}{\partial t} + \vec{v}\frac{\partial f_\alpha}{\partial \vec{r}} + \frac{q_\alpha}{m_\alpha}\left(\vec{E} + \frac{1}{c}\left[\vec{v}, \vec{B}\right]\right)\frac{\partial f_\alpha}{\partial \vec{v}} = 0$$

Dispersion equation

$k \equiv k_\perp$

$$\boxed{k^2c^2 - \omega^2 = \sum_\alpha \omega_{p\alpha}^2 [A_\alpha + (A_\alpha + 1)\,\xi_\alpha \varpi(\xi_\alpha)].}$$

α — particle sort. $\quad \xi_\alpha = i\omega/(kc\beta_\perp^\alpha) \quad \beta_\perp^\alpha = \sqrt{2T_{\perp\alpha}/m_\alpha c^2}$

$\overline{w}(\xi_\alpha)$ — plasma dispersion function.

Basic physics of the Weibel instability

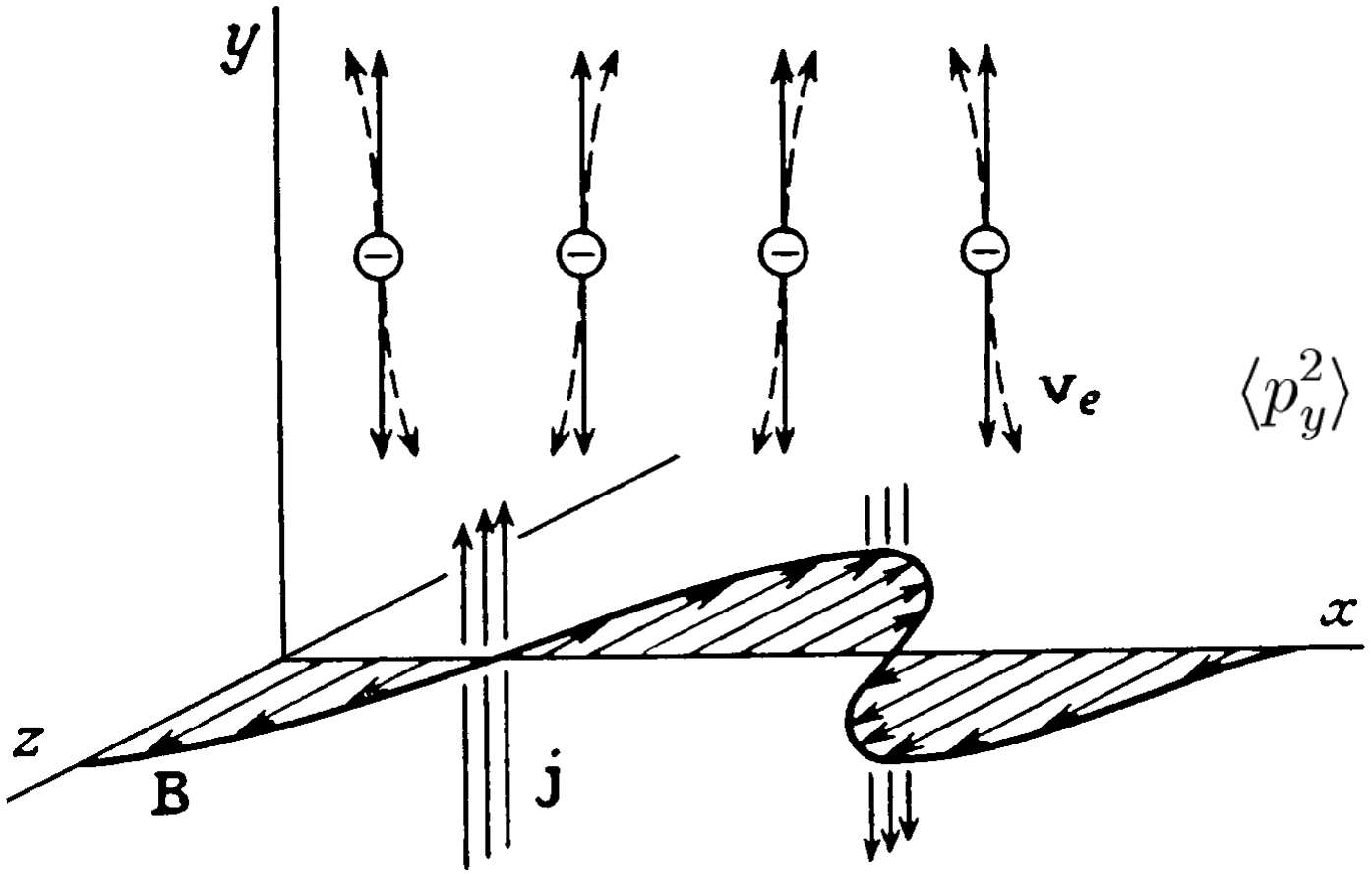

Highly anisotropic velocity distributions are strongly unstable

$$\max(\mathrm{Im}\,\omega) \sim \omega_p/\sqrt{\gamma}$$

Linear stage of the Weibel instability

$$\Omega = \mathrm{Im}\,\omega/\omega_{\mathrm{pe}},\ K = kc/\omega_{\mathrm{pe}}$$

$$\Omega \approx K\,\frac{\beta_{\perp}^{\mathrm{e}}}{\sqrt{\pi}}\,\frac{A_{\mathrm{e}} + A_{\mathrm{i}} m_{\mathrm{e}}/m_{\mathrm{i}} - K^2}{1 + A_{\mathrm{e}} + m_{\mathrm{e}}\beta_{\perp}^{\mathrm{e}}\,(1 + A_{\mathrm{i}})/(m_{\mathrm{i}}\beta_{\perp}^{\mathrm{i}})}$$ — Weibel instability growth rate (linear theory).

$$\Omega_{\max} = \Omega(K_{\mathrm{opt}}) \qquad K_{\mathrm{opt}} = \frac{1}{\sqrt{3}}\,K_{\max} = \sqrt{\frac{A_{\mathrm{e}} + m_{\mathrm{e}}/m_{\mathrm{i}} A_{\mathrm{i}}}{3}}$$

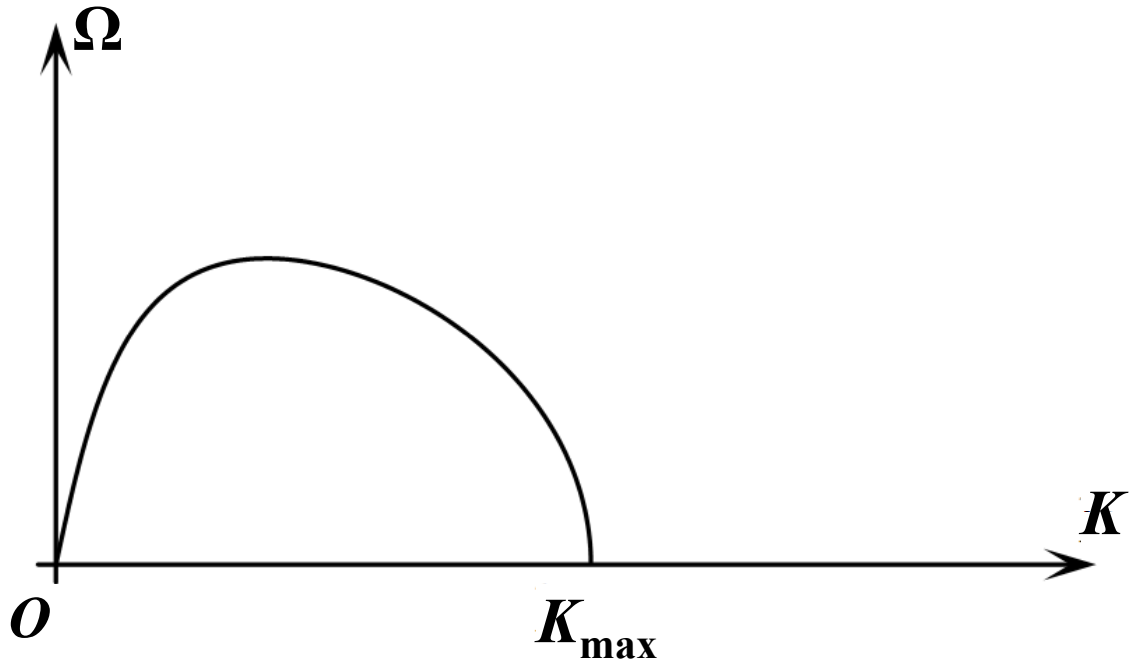

Typical dependence of the growth rate on the wave number *K*

The Vlasov – Maxwell equations

$f_\alpha(\mathrm{r}, \mathrm{p}, t)$ — distribution function, α — particle sort;

E, B (r, t) = E, B[$\{f_\alpha\}$] — electric and magnetic fields.

See, e.g., V.Kocharovsky et al.
J. Plasma Phys. 2022;
RQE 2017, 2020;
JETP Lett. 2017;
Plasma Phys. Rep. 2020, 2022;
Geomag. Aeron. 2022, 2023,
and references therein.

$$\frac{\partial f_\alpha}{\partial t} + \mathbf{v}_\alpha \frac{\partial f_\alpha}{\partial \mathbf{r}} + e_\alpha \left(\mathbf{E} + \frac{1}{c} \mathbf{v}_\alpha \times \mathbf{B} \right) \frac{\partial f_\alpha}{\partial \mathbf{p}} = 0$$

$$\operatorname{rot} \mathbf{B} = \frac{4\pi}{c} \mathbf{j} + \frac{1}{c} \frac{\partial \mathbf{E}}{\partial t}$$

$$\operatorname{rot} \mathbf{E} = -\frac{1}{c} \frac{\partial \mathbf{B}}{\partial t} ,$$

$$\operatorname{div} \mathbf{B} = 0 ,$$

$$\operatorname{div} \mathbf{E} = 4\pi\rho ,$$

$$\rho(\mathbf{r}, t) = \sum_\alpha N_\alpha e_\alpha \int f_\alpha(\mathbf{r}, \mathbf{p}, t) \, \mathrm{d}^3 p ,$$

$$\mathbf{j}(\mathbf{r}, t) = \sum_\alpha N_\alpha e_\alpha \int f_\alpha(\mathbf{r}, \mathbf{p}, t) \frac{\mathbf{p}}{m_\alpha \gamma_\alpha} \, \mathrm{d}^3 p$$

$$\gamma_\alpha = (1 + \mathbf{p}^2 / m_\alpha^2 c^2)^{1/2}$$

Darwin scheme

$$\operatorname{rot}\mathbf{B} = \frac{4\pi}{c}\,\mathbf{j} + \frac{1}{c}\boxed{\frac{\partial \mathbf{E}_\ell}{\partial t}}, \qquad \operatorname{div}\mathbf{B} = 0,$$

$$\operatorname{rot}\mathbf{E}_\mathrm{t} = -\frac{1}{c}\,\frac{\partial \mathbf{B}}{\partial t}\,, \qquad \operatorname{div}\mathbf{E}_\ell = 4\pi\rho,$$

$$\mathbf{E} = \mathbf{E}_\ell + \mathbf{E}_\mathrm{t}, \qquad \operatorname{rot}\mathbf{E}_\ell = 0, \qquad \nabla\mathbf{E}_\mathrm{t} = 0.$$

PIC-code DARWIN (2D3V)

$m_\mathrm{i}/m_\mathrm{e} = 36$ $\quad L_x = L_y = 100c/\omega_\mathrm{pe}$ $\quad$ 512 × 512 cells, $2.4\cdot10^9$ particles

$$T = 22\,000/\omega_\mathrm{pe}$$

$m_\mathrm{i}/m_\mathrm{e} = 100$ $\quad L_x = L_y = 100c/\omega_\mathrm{pe}$ $\quad$ 768 × 768 cells, $2.4\cdot10^9$ particles

$$T = 8\,000/\omega_\mathrm{pe}$$

Borodachev L. V., Kolomiets D. O. // *J. Plasma Physics.* 2011. V. 77, n. 2. P. 277.

Numerical simulations of the nonlinear stage of Weibel instability

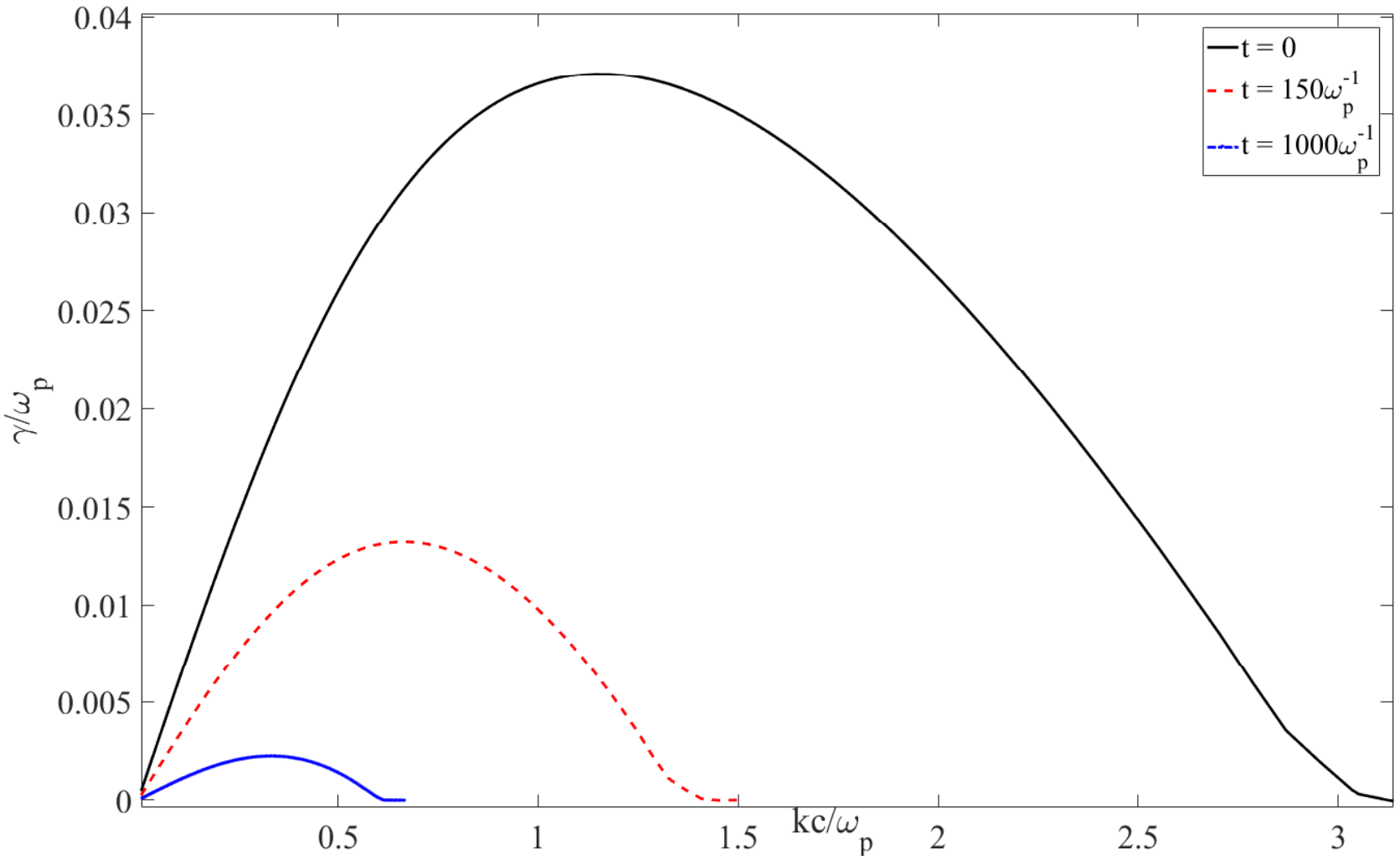

Linear growth rate as a function of a wavenumber *K* calculated for the anisotropy degree values taken at t = 0, 150, and 1000 ω_p^{-1}, with due account for a nonlinear decay of the particle anisotropy.

A preview

We consider, for the first time to our knowledge, the nonlinear stage of the Weibel instability in **a two-component plasma with strong temperature anisotropy and equal initial energies of electrons and ions** on the basis of numerical simulation with the 2D3V PIC-code DARWIN.

The Maxwellian distributions of particles for each velocity projection were initially set, but with different temperatures along and across the z or x axis, with the longitudinal temperature being the greater, so that the development of the instability led to the formation of current filaments or sheets along either z or x axis. The simulations, carried out in the plane orthogonal to the z or x axis, made it possible to investigate the long-term evolution of a quasi-stationary magnetic field and current filaments created first by the electrons and then jointly by the electron and ion fractions.

In the process of saturation and non-linear power-law decay, the small-scale magnetic field created by the electron currents of the Weibel instability induces an electric field that generate the ion currents. These ion currents determine the long-term slow evolution of the large-scale magnetic field perturbations.

Over time the electrons become isotropic and a significant part of them becomes magnetized or trapped by the strong magnetic field lines. It ”freezes” the evolution of magnetic fields, eliminating or delaying the ion Weibel instability, which could otherwise develop due to remaining for a long time an anisotropy of ion temperatures.

Saturation of the Weibel instability

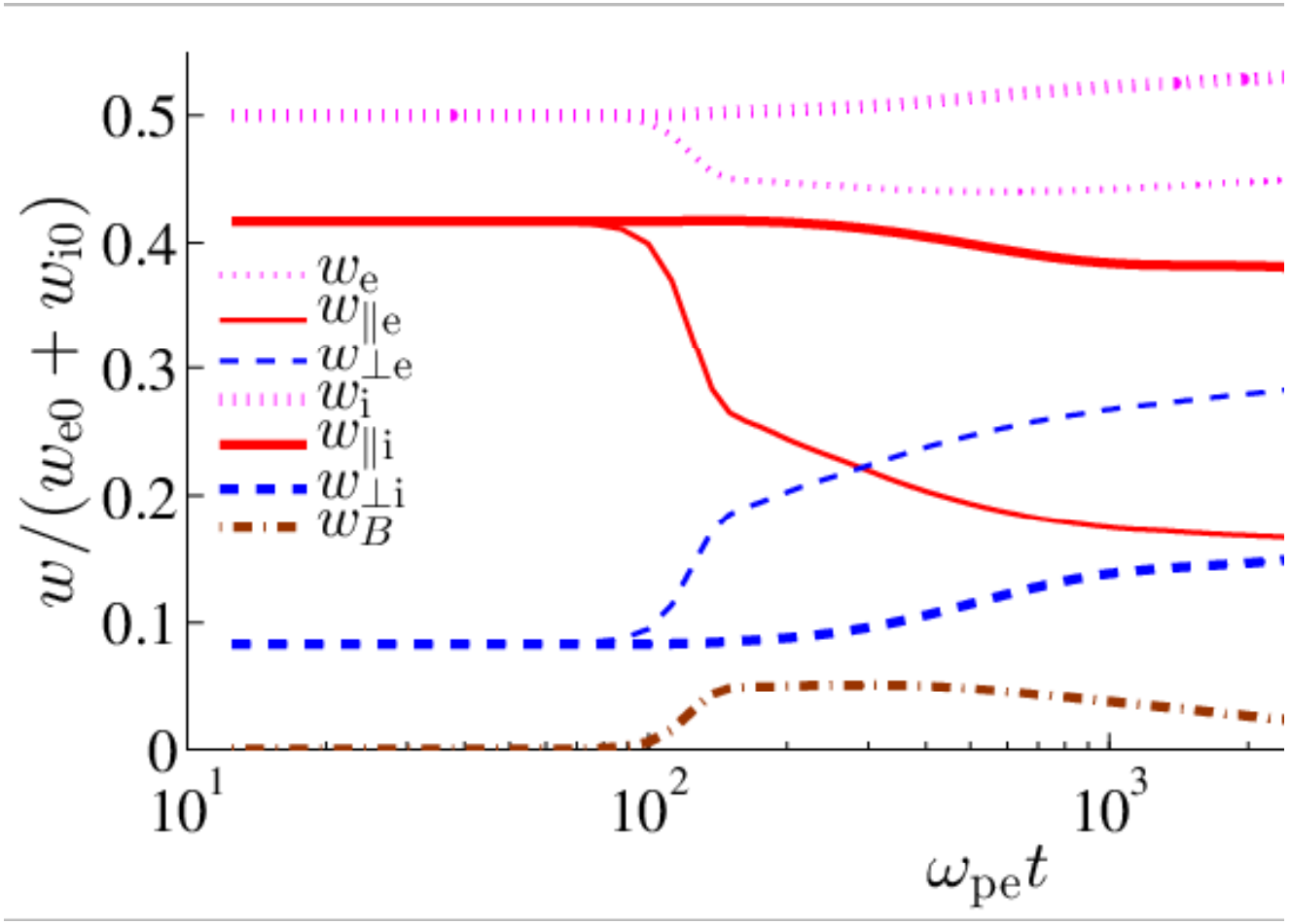

Figure 1. Total energy of ions, electrons and the magnetic field normalized to the initial total particle energy.

On the time interval from 2 000ω_{pe}^{-1} or 4 000ω_{pe}^{-1} to 10 000ω_{pe}^{-1} (for m_i/m_e = 36 or 100, respectively) the large-scale ion currents dominate the electron ones and determine the long-term dynamics of the magnetic field.

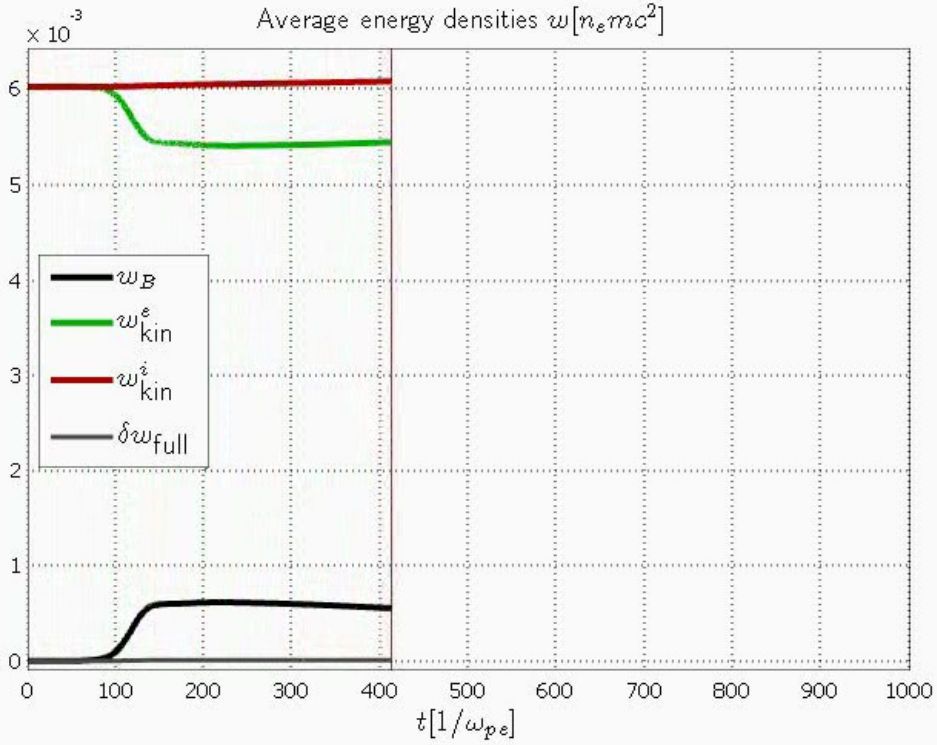

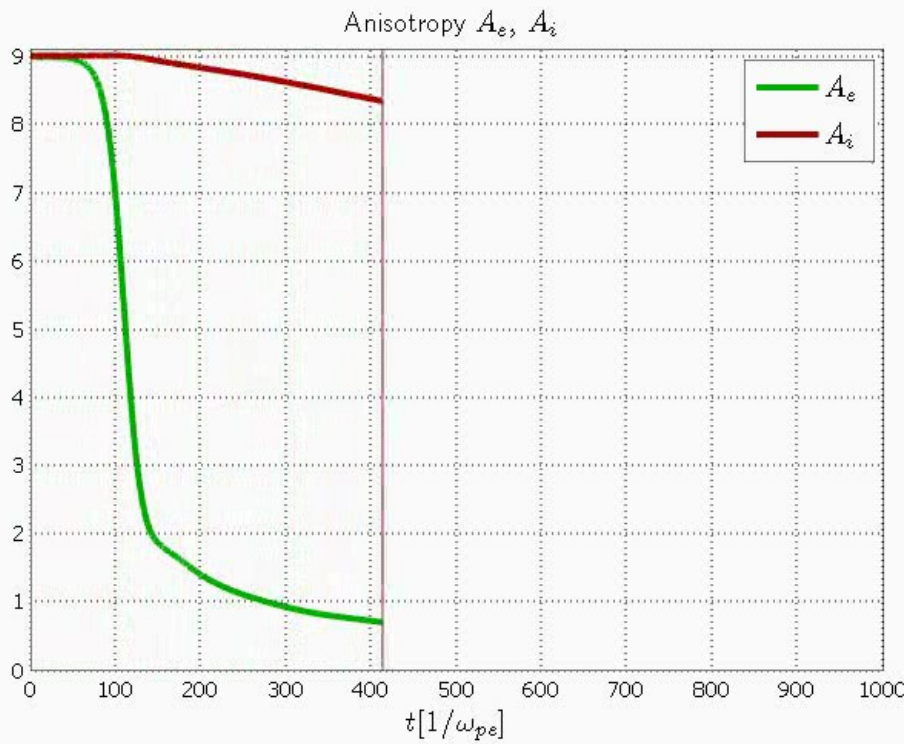

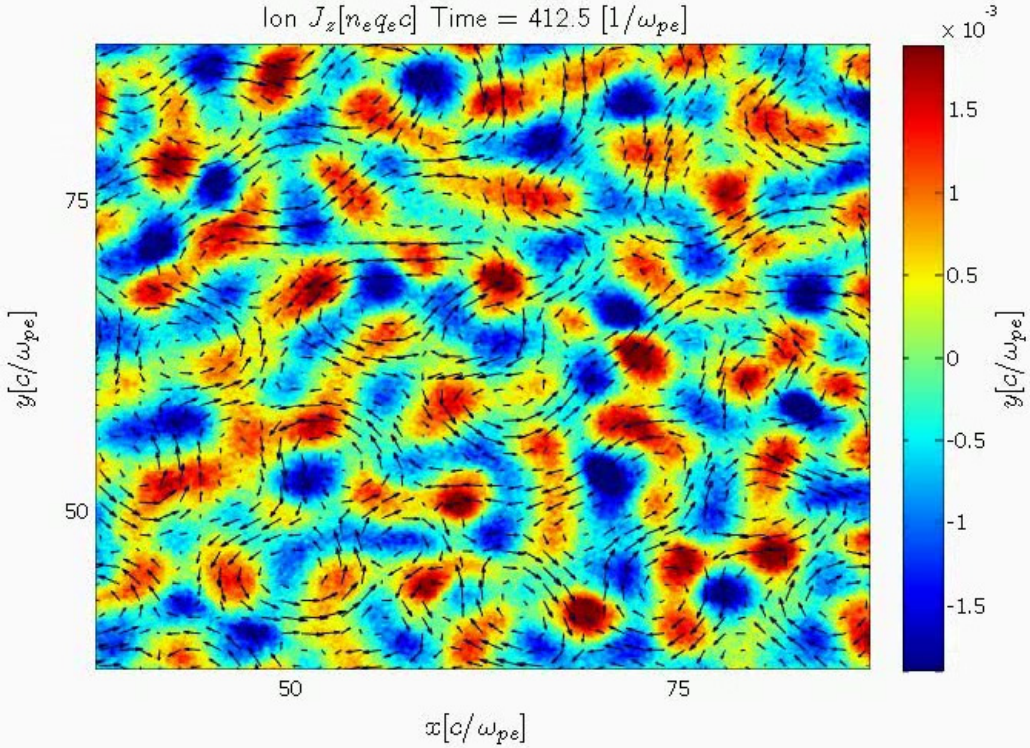

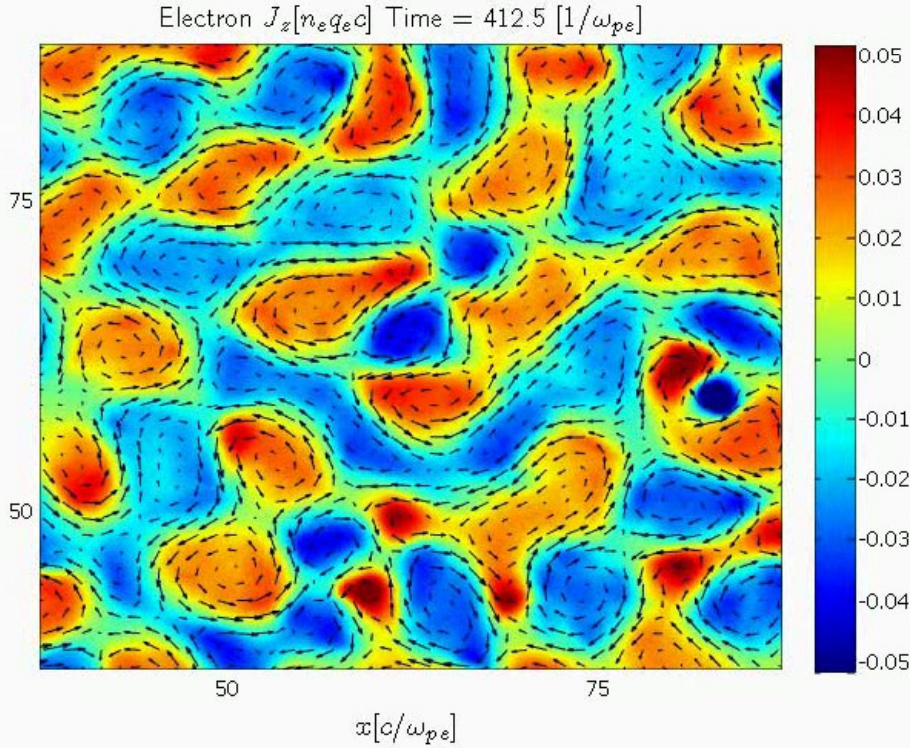

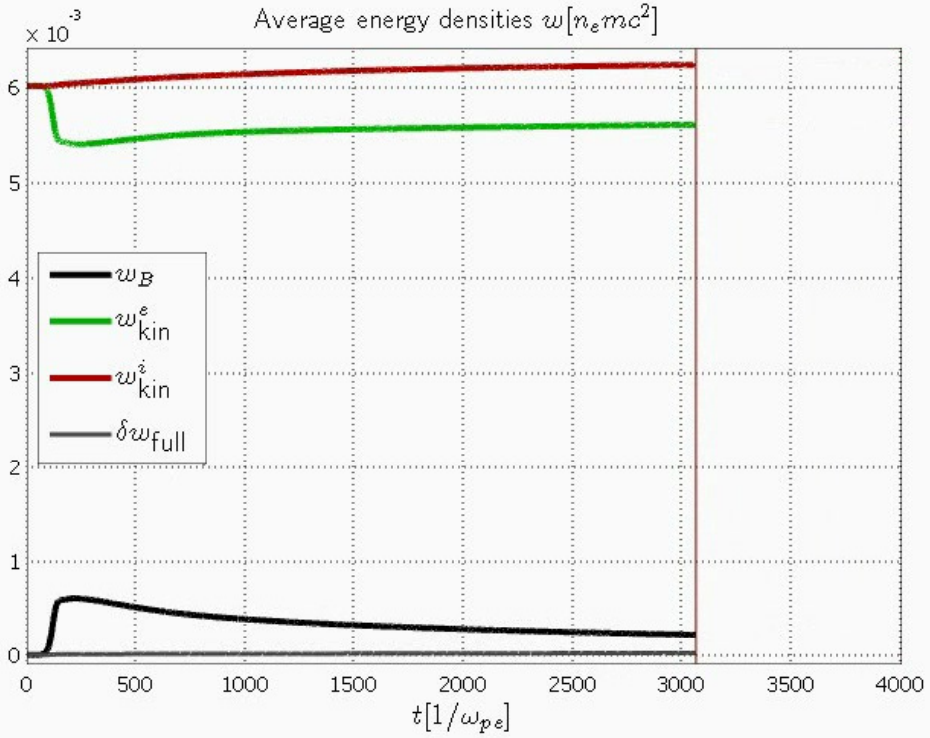

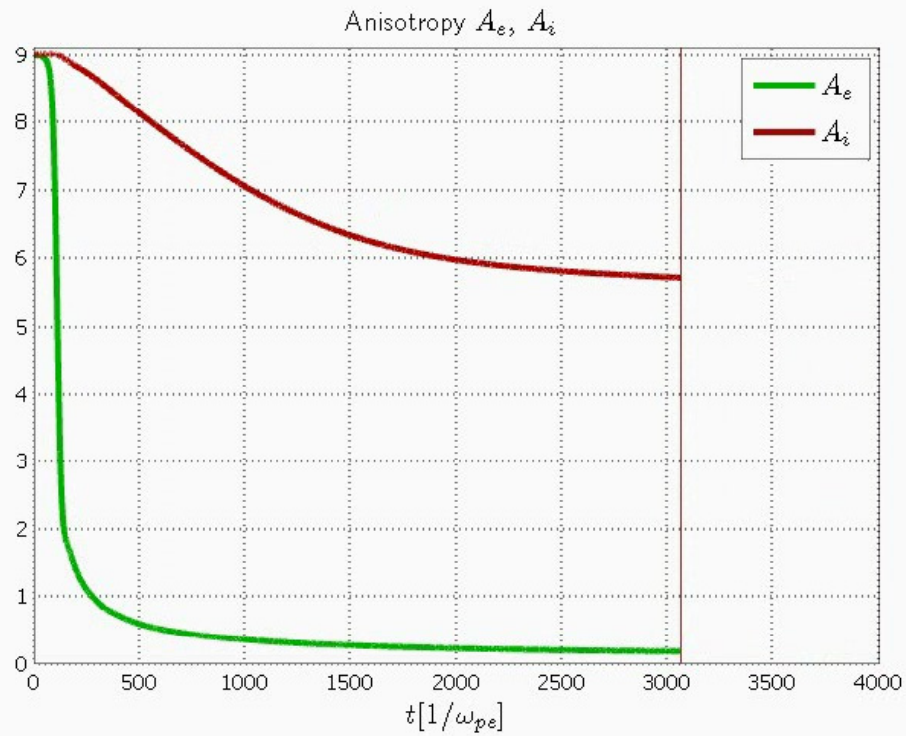

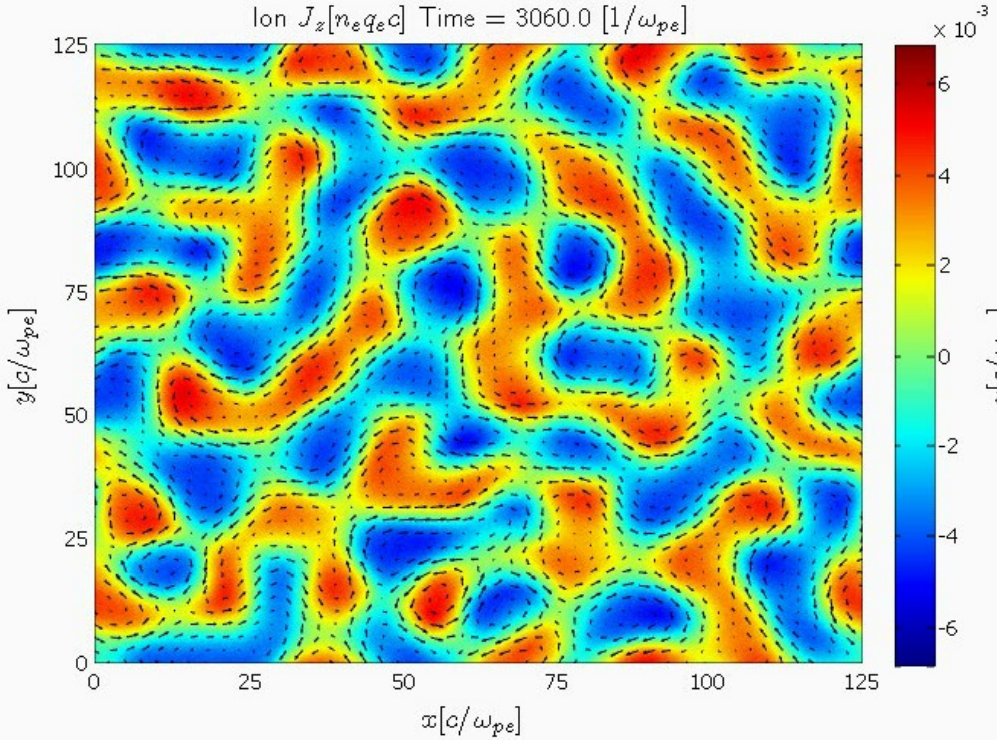

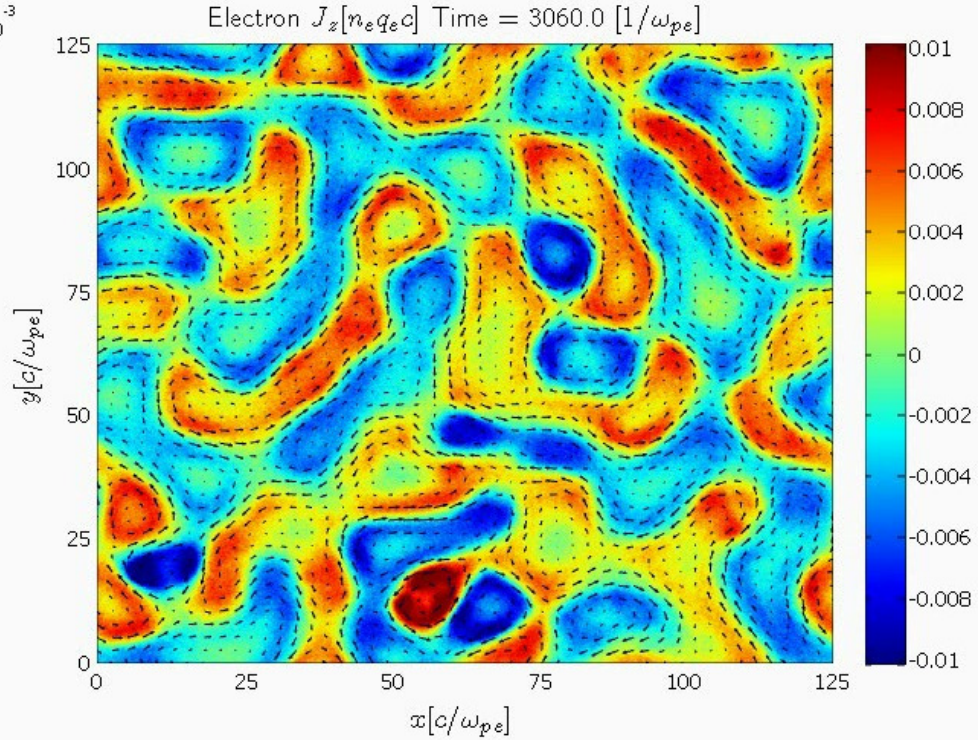

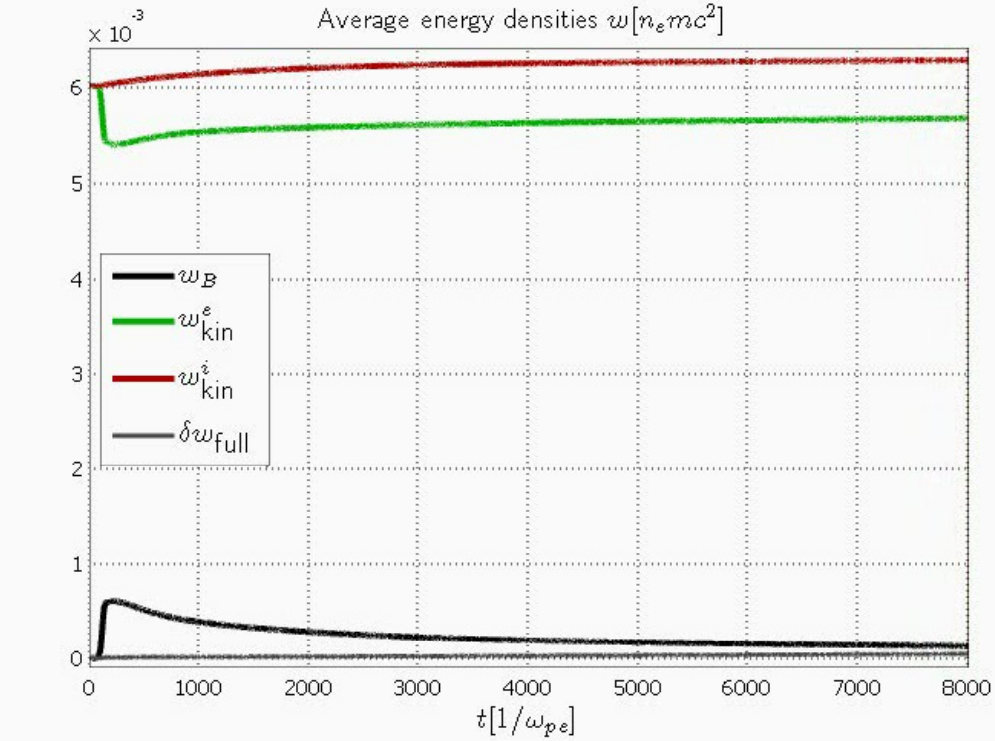

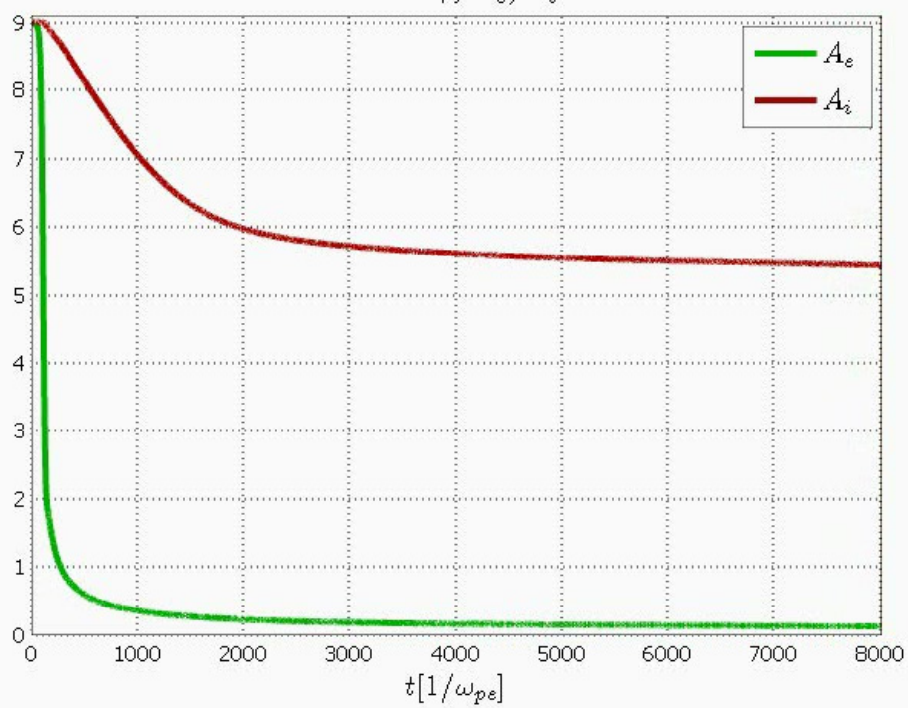

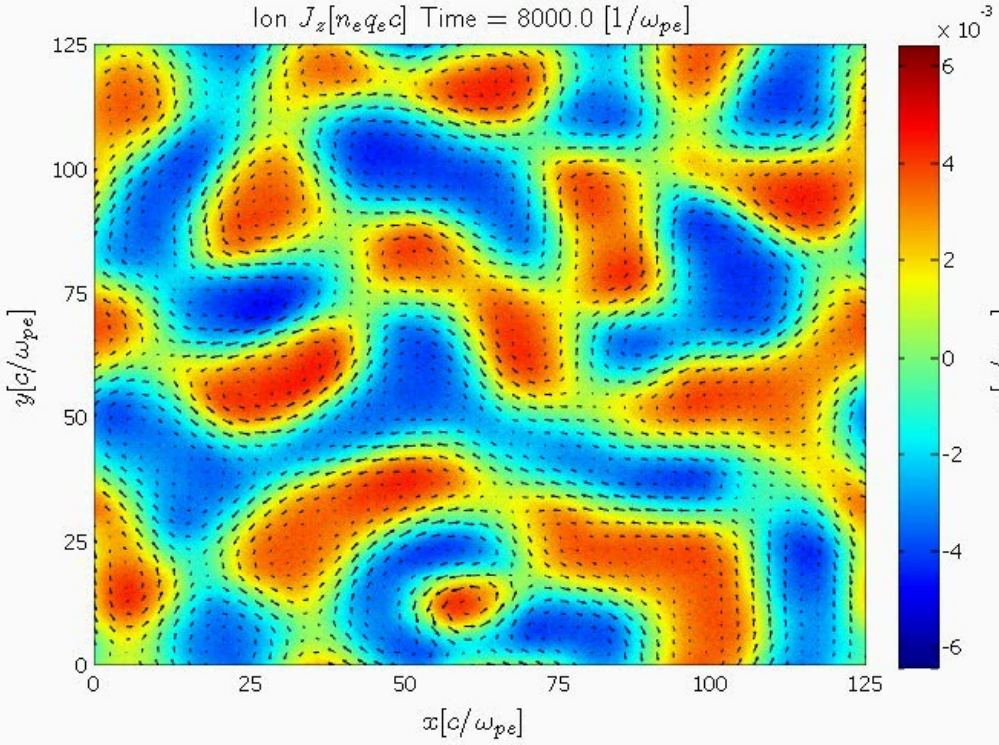

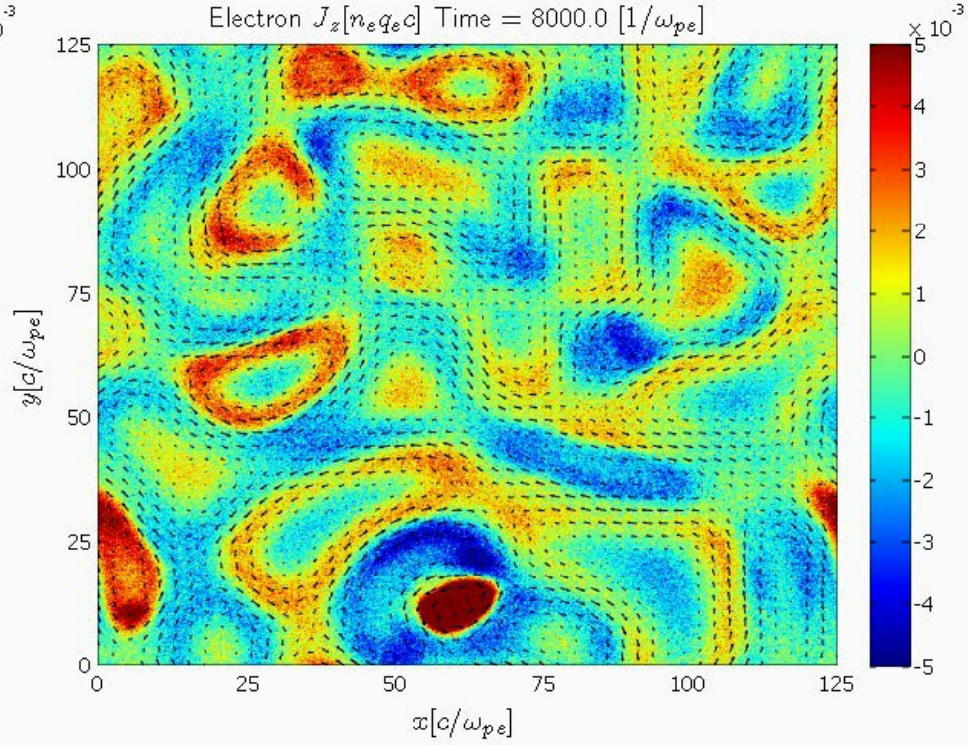

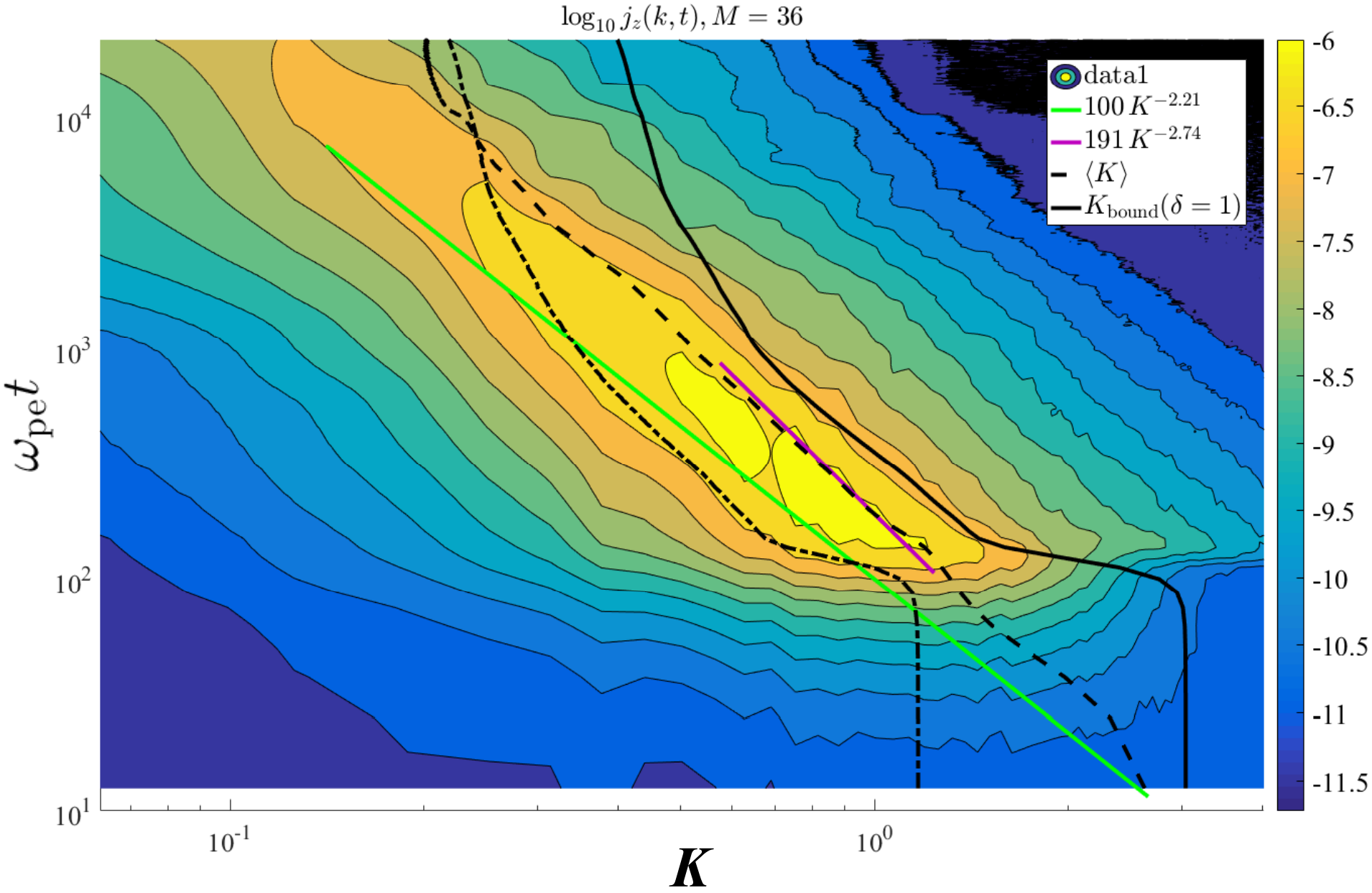

Spatial spectrum of the total current density along z axis in dependence on time (m_i / m_e = 36) in the case of an anisotropic axis z transverse to the plane of 2D modelling (x,y). Solid and dash-dotted curves are the boundary of unstable wave numbers and the optimal wave number according to the linear theory, dashed line — the average wave number from the simulation.

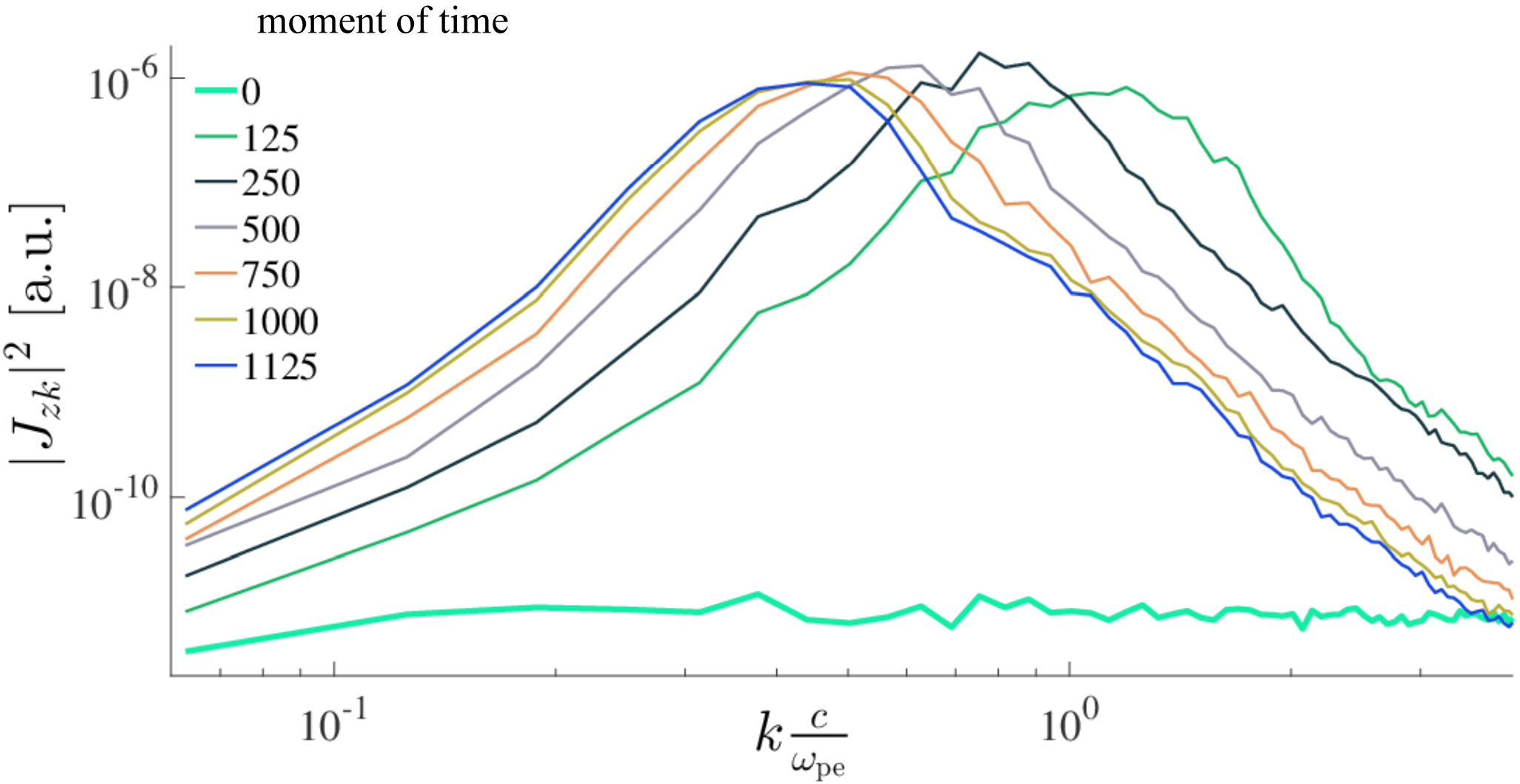

Spatial power spectra of the longitudinal current density at different moments of time. The typical current filament size grows with time approximately as a square root $\sim\sqrt{t}$.

For details see the talks of Nechaev and Kuznetsov at seminar 3 (Nov. 9), hall 1.

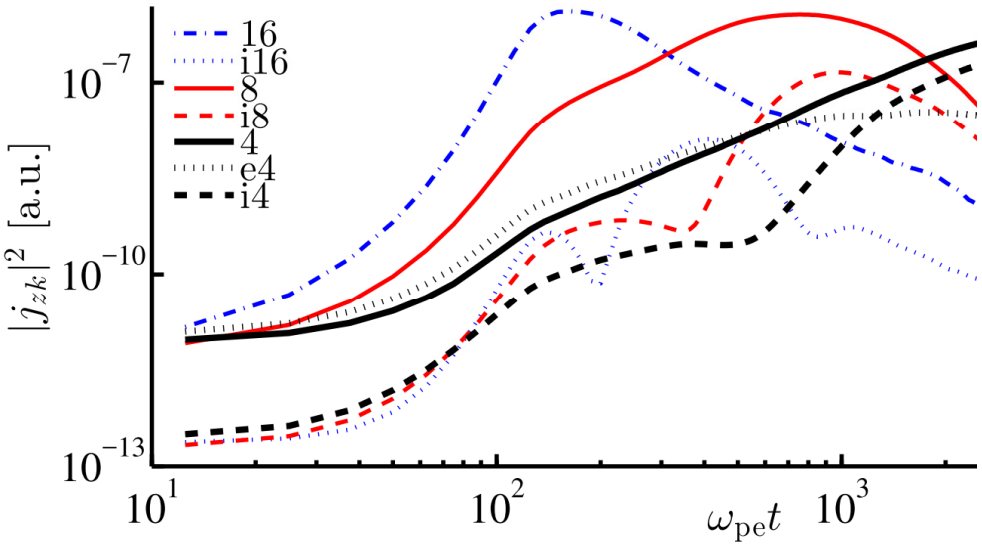

Figure 2. Spectral power of different harmonics of the electron (j_{ze}), ion (j_{zi}), and total (j_z) current densities. Spectral power of different harmonics of the total magnetic field decays as $\sim t^{-5/2}$.

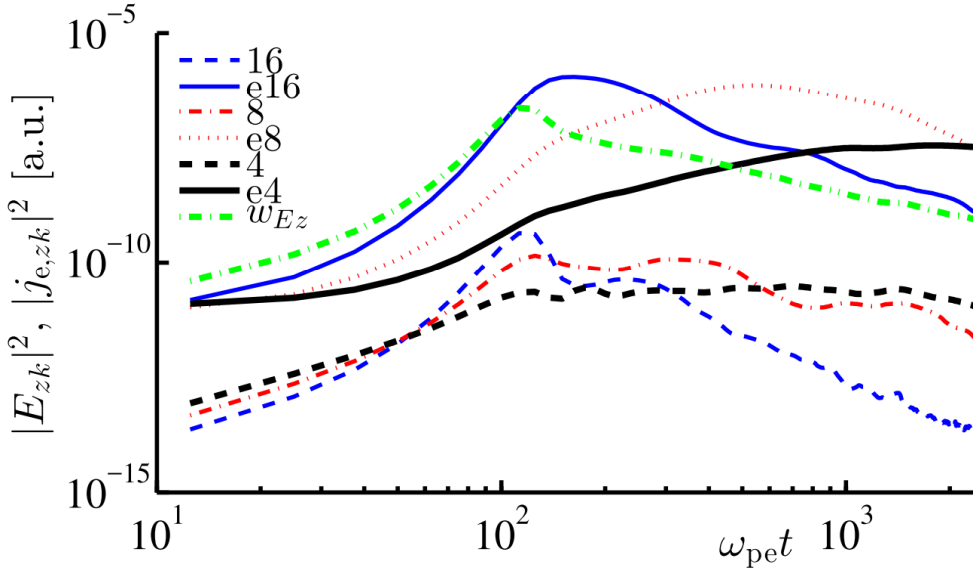

Figure 3. Spectral power of different harmonics of the electron current density (j_{ze}) and electric field (E_z). The latter decays according to a power-law $\sim t^{-5/3}$, i.e., faster than the magnetic field $\sim t^{-(1\ -\ 1.4)}$.

Similar 2D3V PIC-analysis of the current turbulence and its spatial spectra in the case when the axis with the largest initial temperature is in the simulation plane (the horizontal axis).

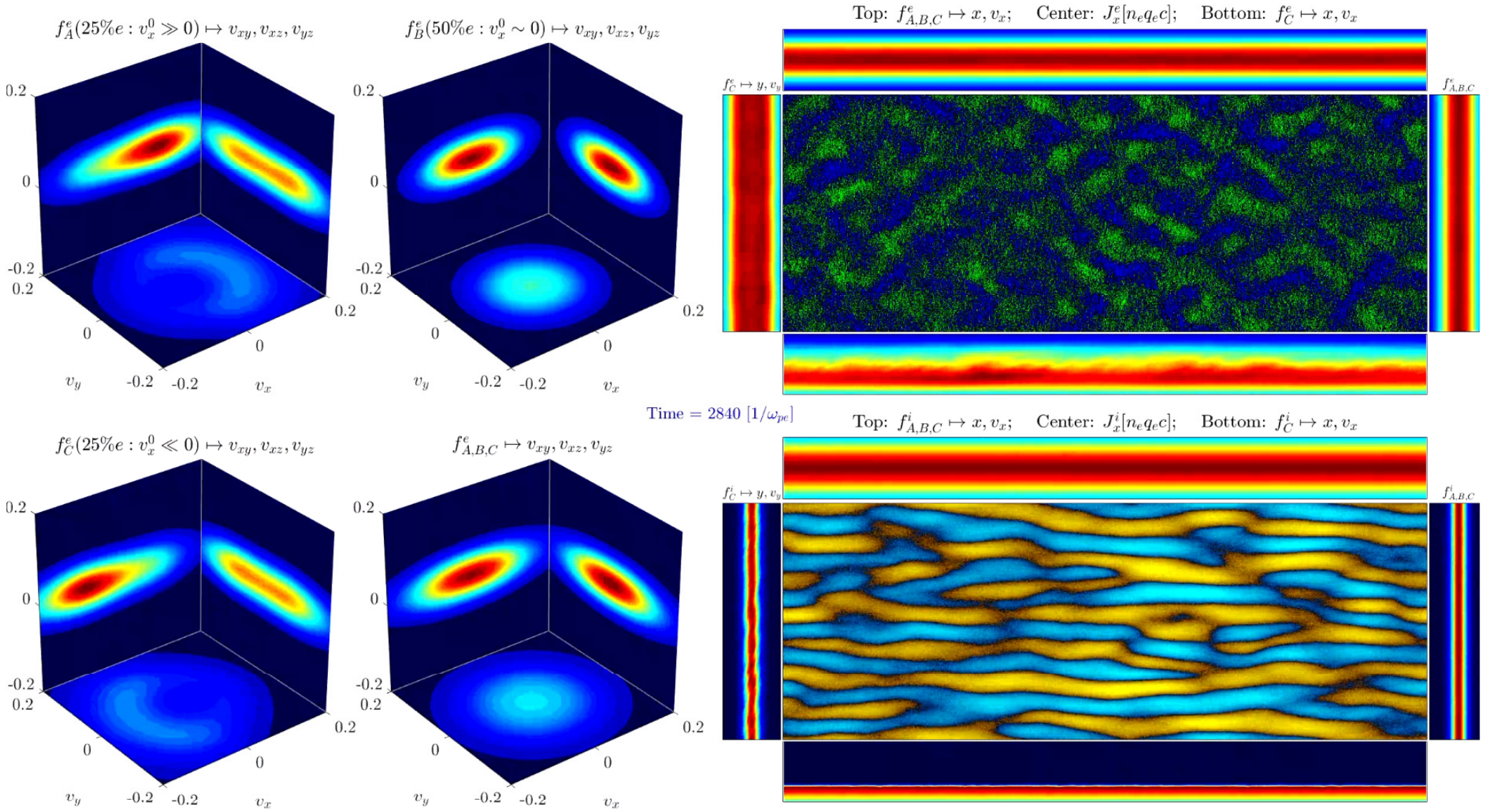

Similar 2D3V PIC-analysis of the current turbulence and its spatial spectra in the case when the axis with the largest initial temperature is in the simulation plane (the horizontal axis).

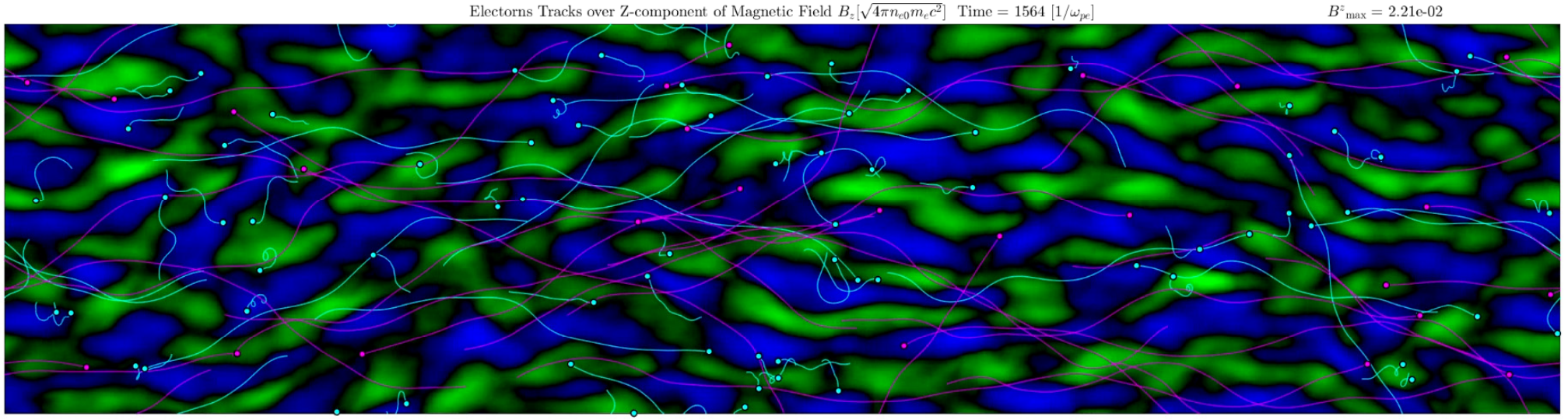

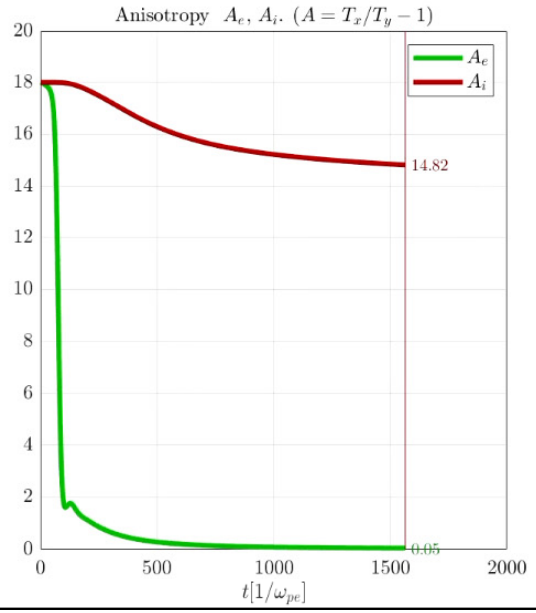

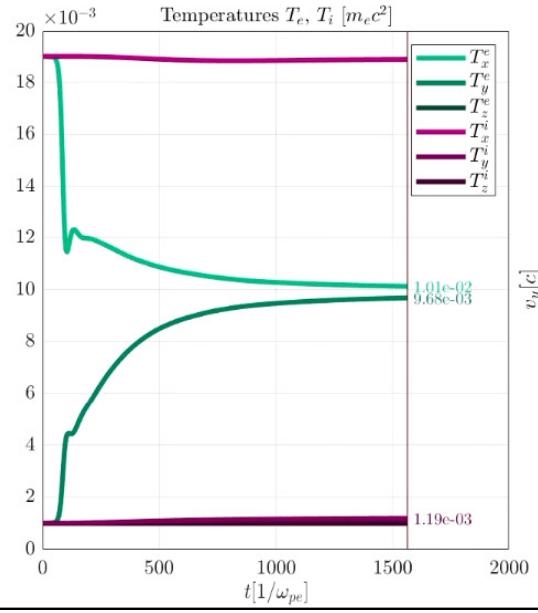

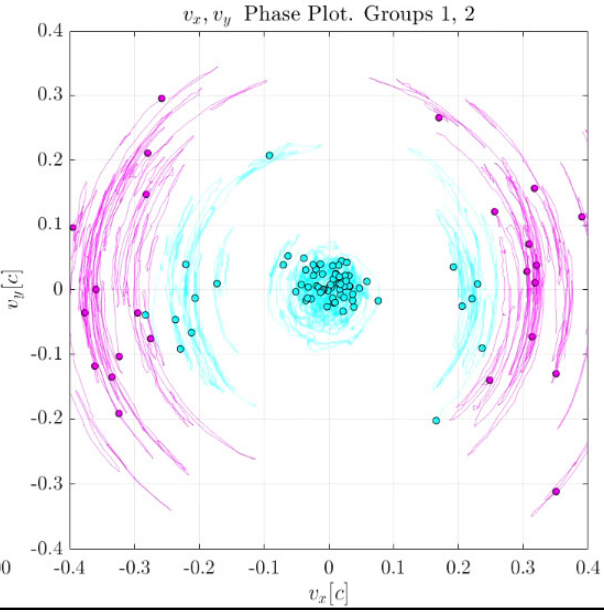

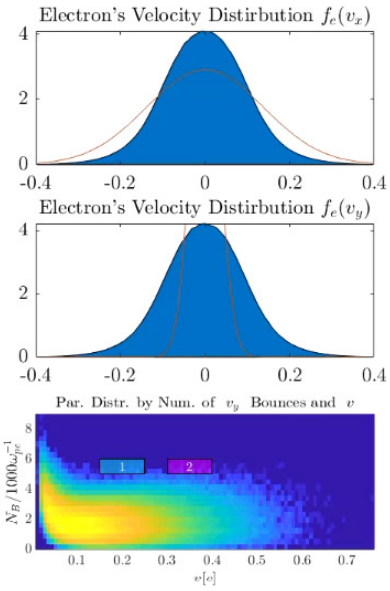

Conclusions on the problem # 1

1. Using 2D3V PIC-code DARWIN, based on a radiationless Maxwell equations' approximation, we carried out a simulation of a nonlinear stage of the Weibel instability and the self-consistent particle dynamics in a collisionless plasma with comparable energy content and anisotropy parameters of electrons and ions ($A_e = A_i \sim 10$).

2. **The evolution of spatial spectra of the magnetic field and current density created, first, by electrons and, then, by the electrons and ions together is found. There is a relay-race growth and decay of the electron-current harmonics due to dephasing of the electron trajectories, so that the spatial spectrum proceeds from small to larger scales.**

3. In the process of nonlinear power-law decay, the small-scale magnetic field created by the electron currents induces the ion ones. The latter gradually overcome the current of electrons and determine the long-term slow evolution of the large-scale perturbations of the magnetic field. The magnetic field energy is of the order of several percent of the particle energy.

4. **At the late stage, the electrons become isotropic, and some part of them is magnetized or trapped. It may result in a considerable delay and even suppression of the ion Weibel instability, which otherwise could develop due to the remaining anisotropy of ions.**

5. Eventually the electron currents become much weaker than the ion ones and follow the latter. In a fully 3D case, this scenario of the formation of the self-consistent current filaments and magnetic field is still under question at very long stage. The solution of this problem can unveil a role of the Weibel instability in the formation of turbulence in stellar (solar) winds.

2. A quasi-electrostatic shock accompanied by, first, a plasma density bump formation and, second, a magnetic field generation due to hot electrons

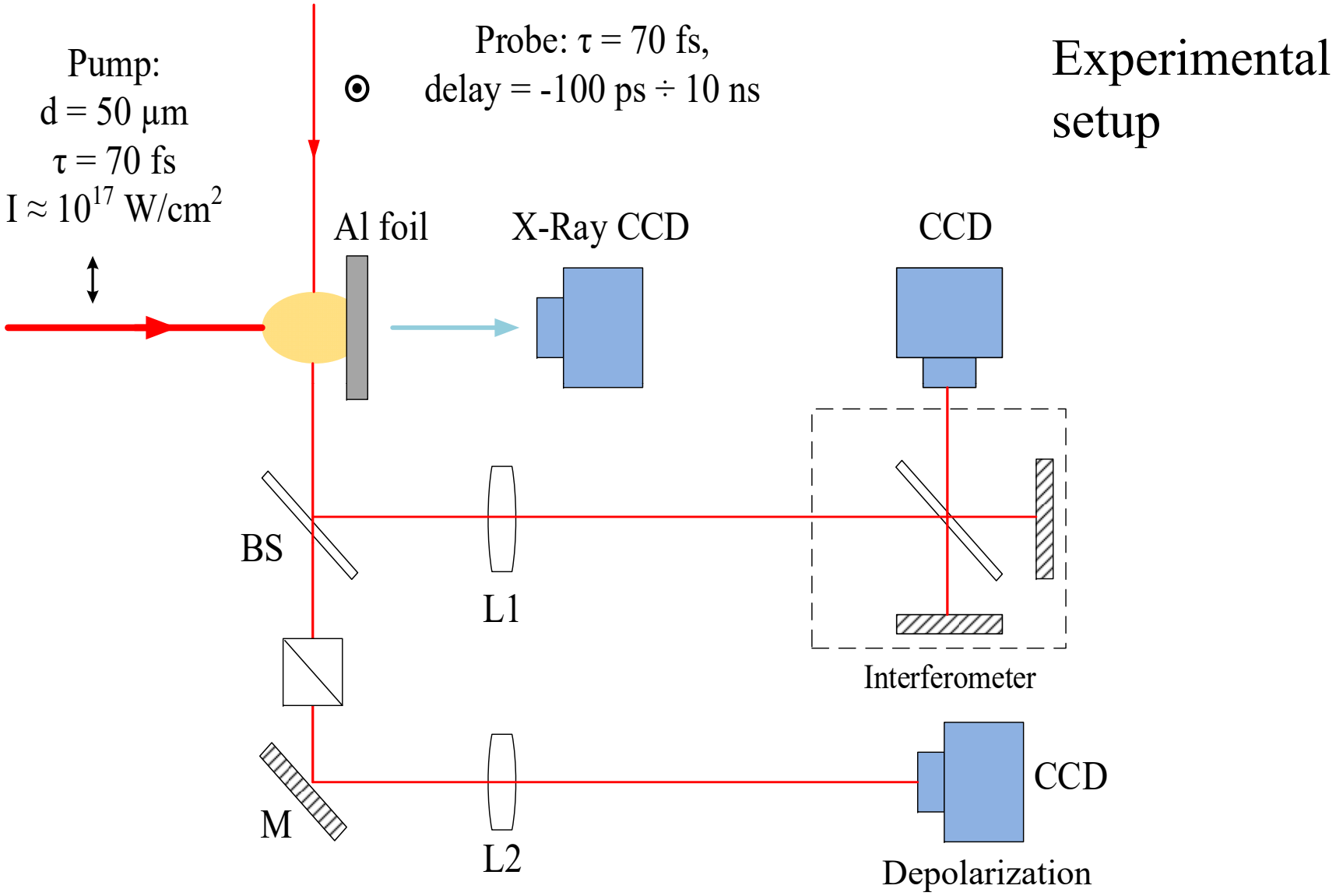

M. A. Garasev, A. I. Korytin, V. V. Kocharovsky et al. *JETP Lett.* 105, 164 (2017)

W = 95 mJ

Laser

2D phase distribution

Experimental results

τ = 0.85 ns

τ = 1.35 ns

τ = 2.35 ns

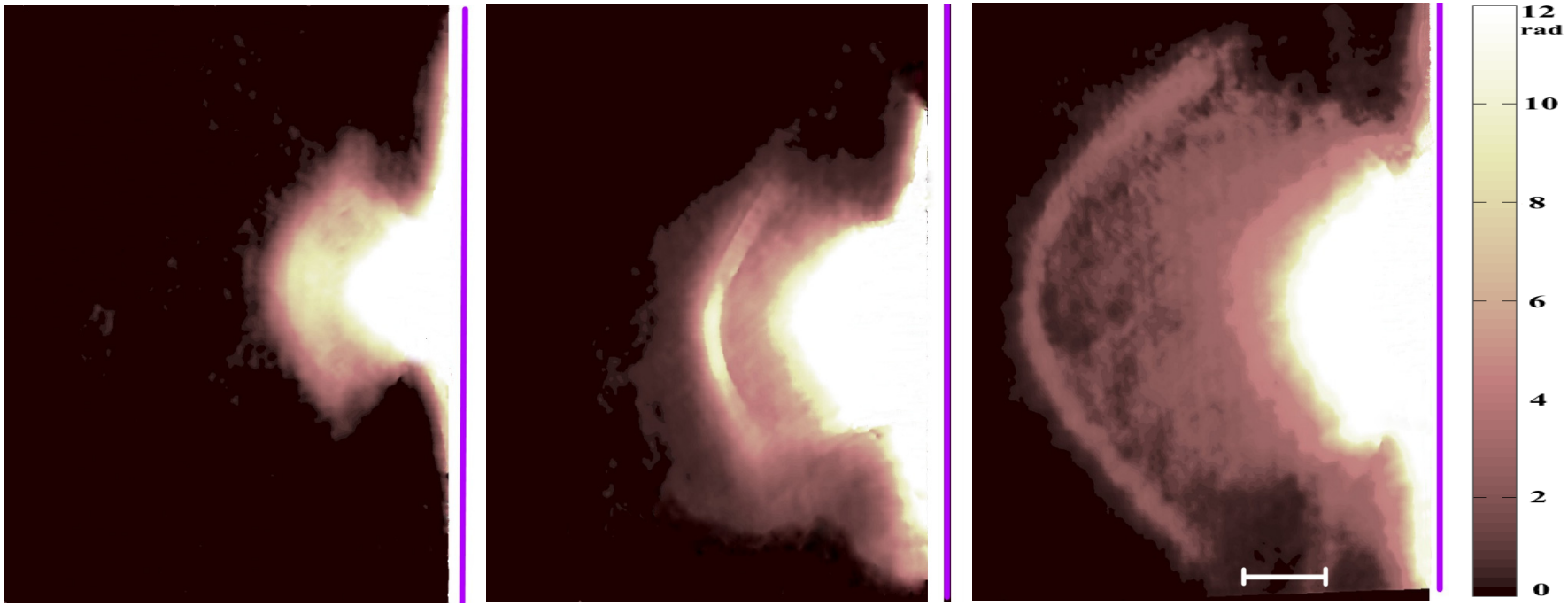

100 mkm

M. A. Garasev, A. I. Korytin, V. V. Kocharovsky et al. *JETP Lett.* 105, 164 (2017)

Experimental results

Plasma density distribution, τ = 1.35 ns

2D

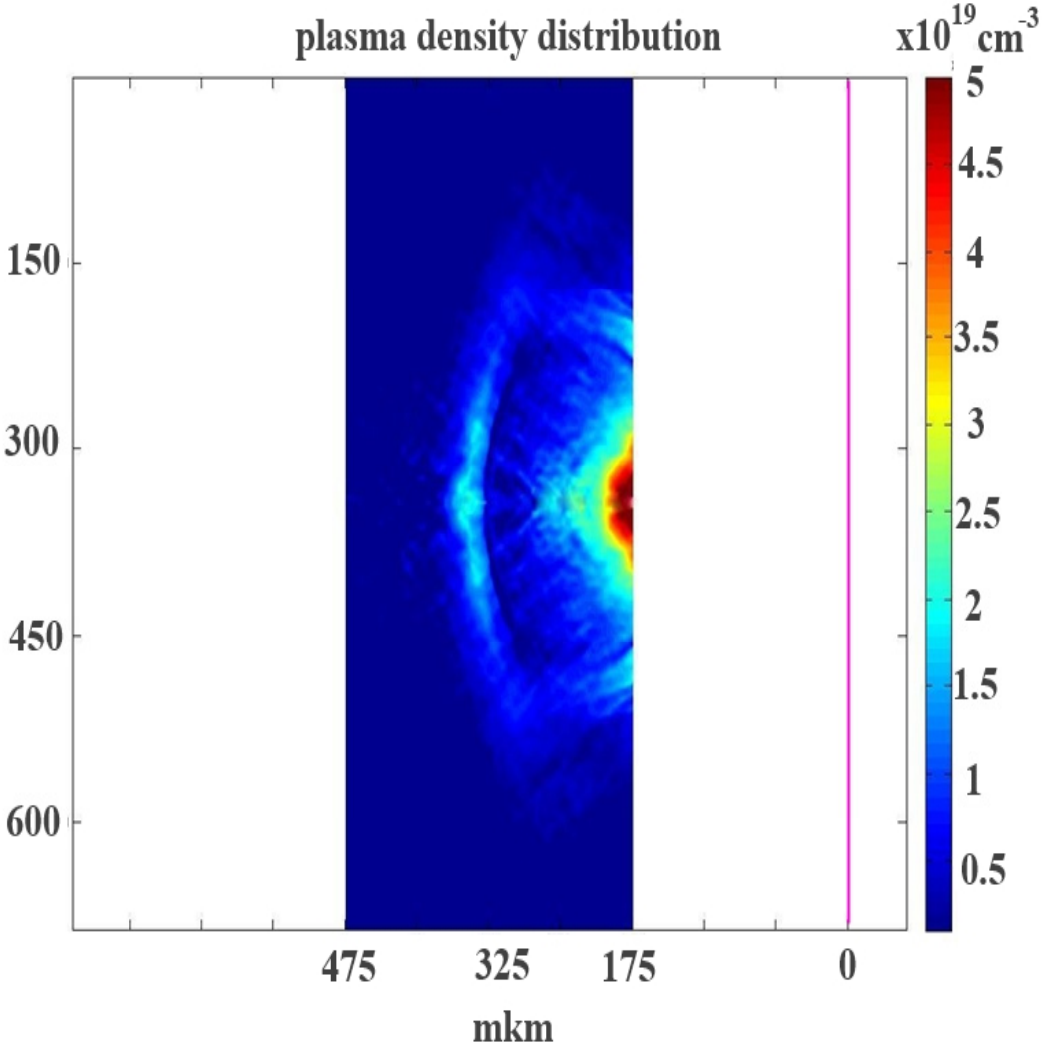

1D

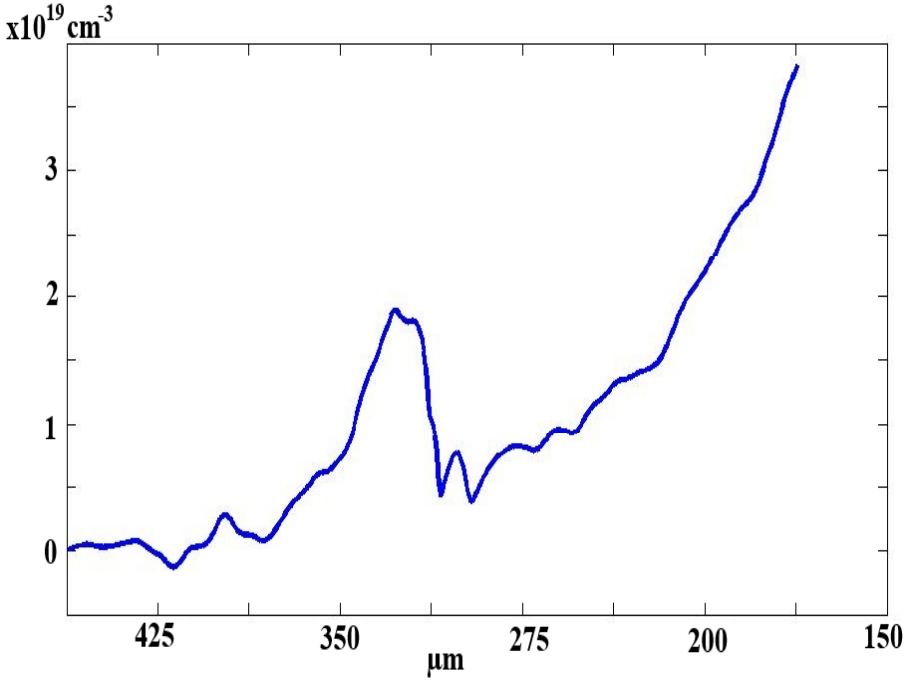

Formation of a density bump

Experimental results

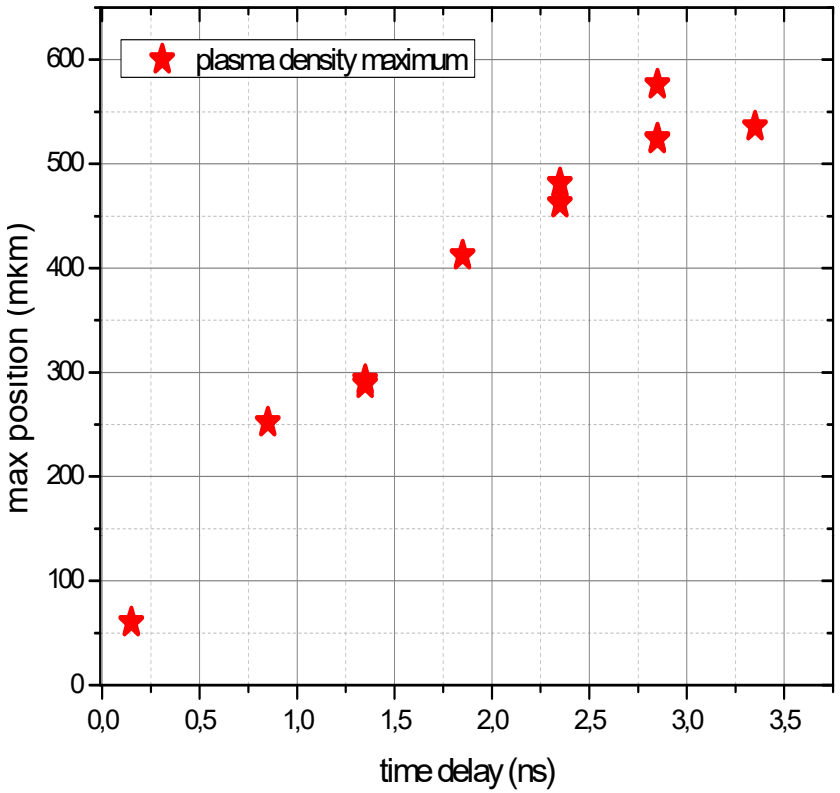

Position of max plasma density
at different moments of time

$V_{is} \approx 1.5 \cdot 10^7$ cm/s => $T_e = 2–3$ KeV

X-ray spectrum from plasma (Andor)

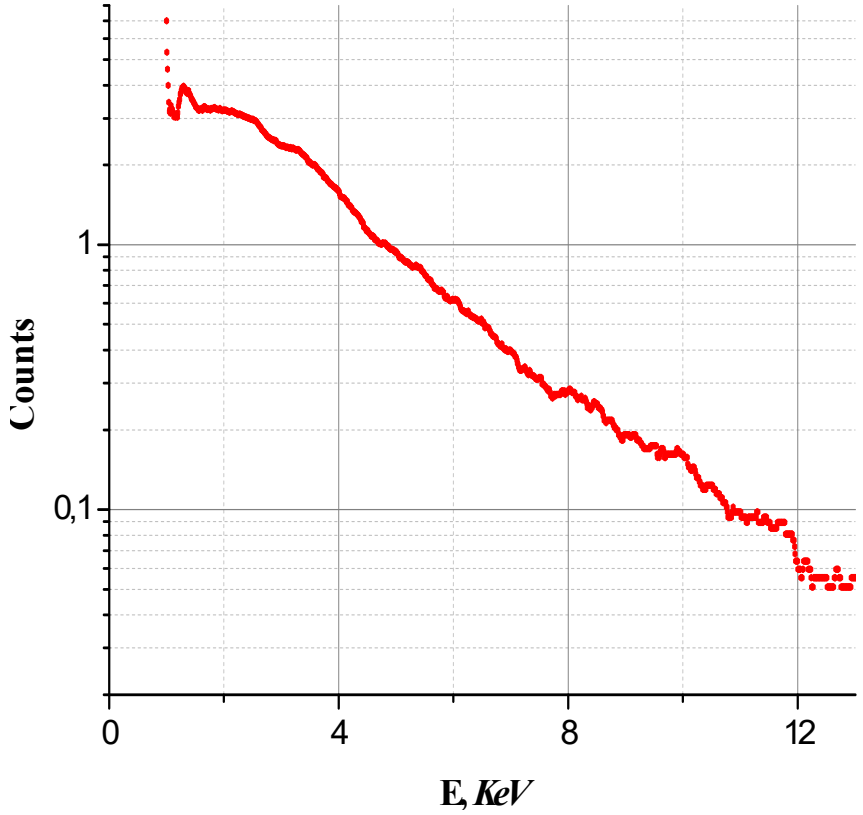

Temperature of electrons

$T_e = 2–2.5$ KeV

Experimental observations of a density bump and a magnetic field structure

t= 0.85 ns

t=1.8 ns

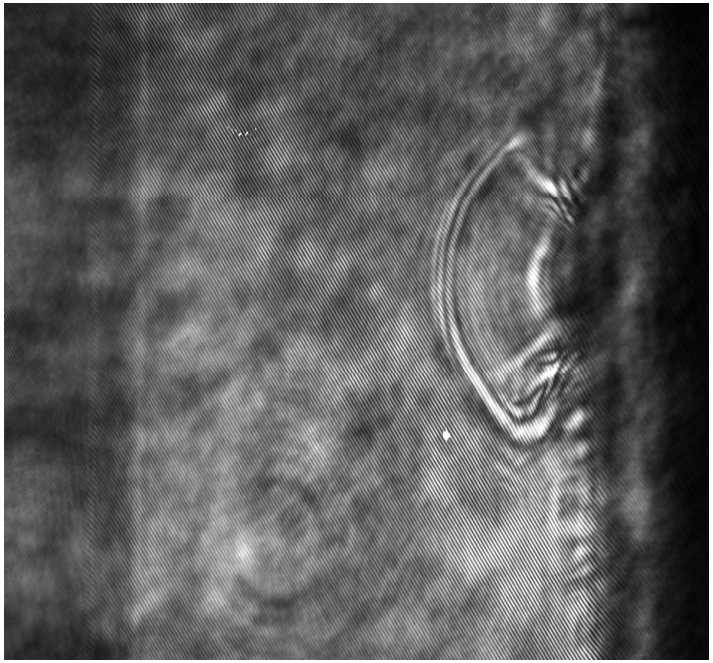

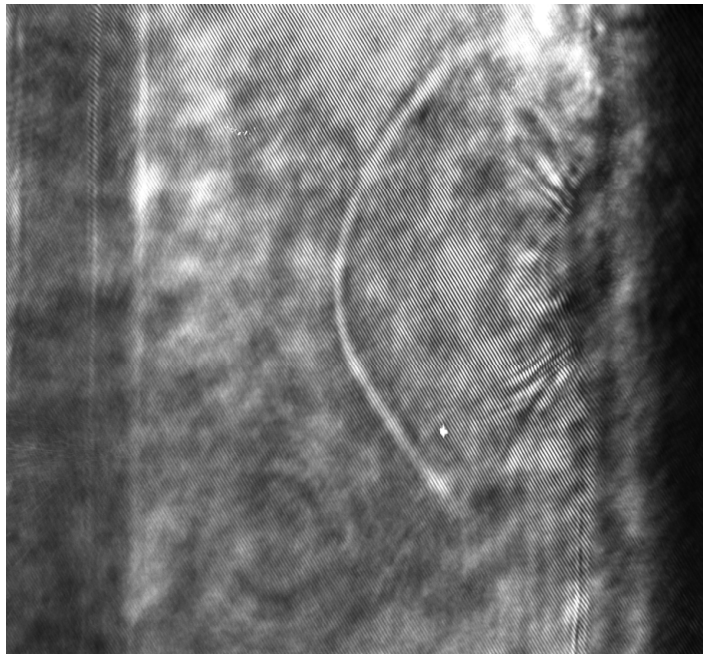

Laser

W = 95 mJ

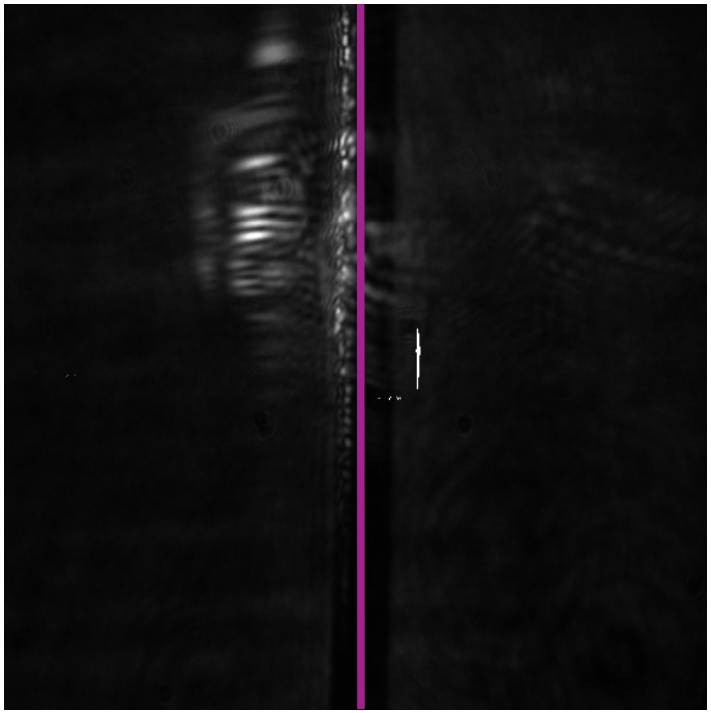

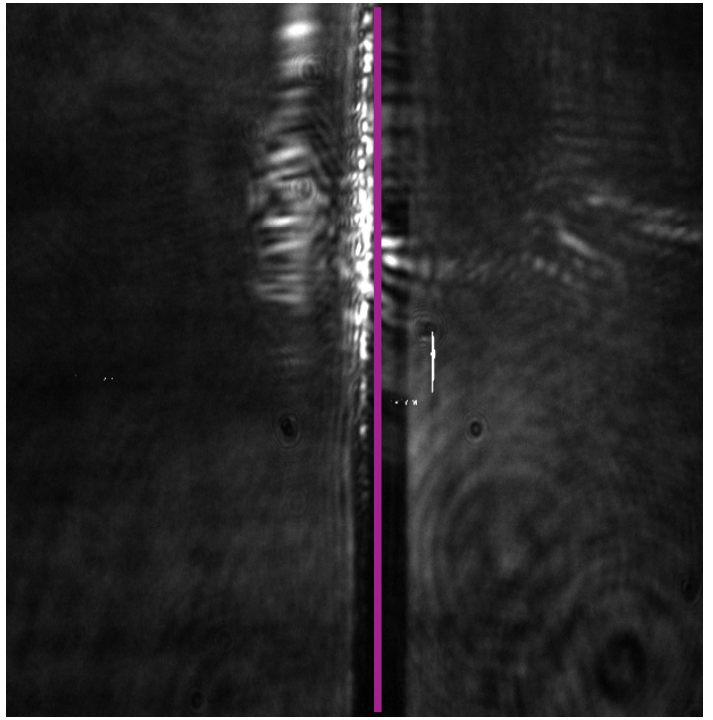

Early experiments

L. Romagnani et al. PRL, 101, 025104 (2008)

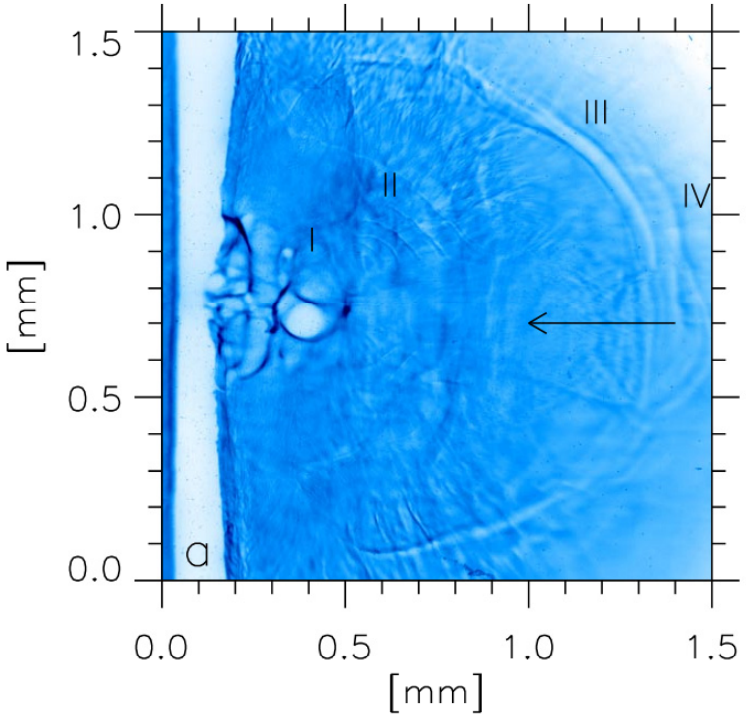

The ion-acoustic solitons were considered mainly. See Medvedev Yu.V. "Nonlinear phenomena of the decay of discontinue-ties in a rarefied plasma" (M.: Fizmatlit, 2012) and references therein.

H. Ahmed et al. PRL, 110, 205001 (2013)

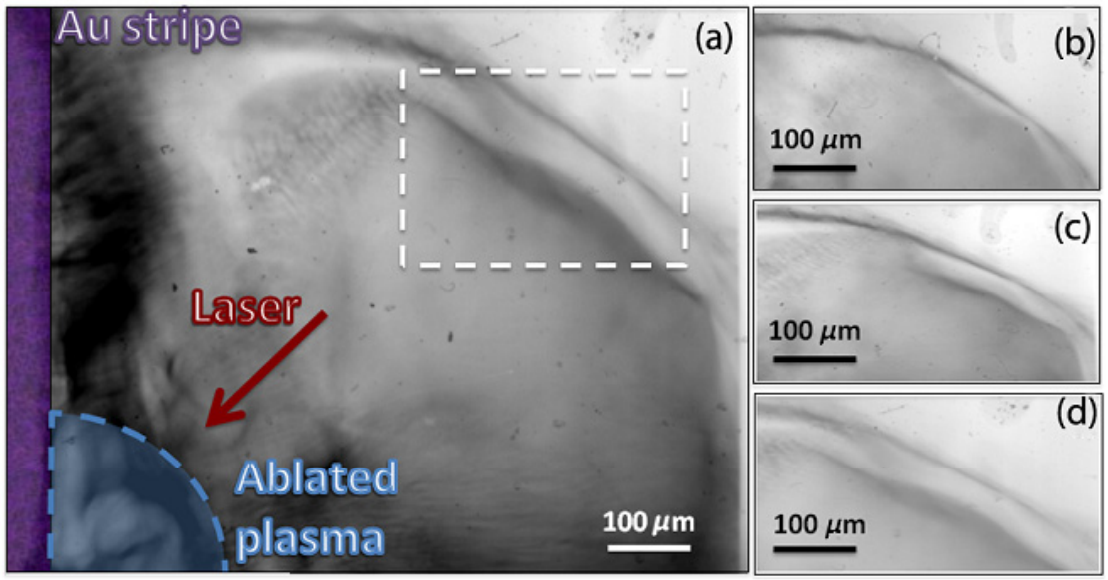

FIG. 2 (color online). Two-dimensional proton radiographs: (a) Proton radiograph of the interaction of a nanosecond laser pulse (red arrow) with a 50 μm gold foil (left purple rectangle) corresponding to 170 ps after the arrival of the long pulse (see Fig. 1). Zooms of the proton radiographs of the region highlighted by the dashed white rectangle in the frame (a) for different proton energies of approximately 11.5 [frame (b)], 10 [frame (c)], and 9 [frame (d)] MeV. These energies correspond to a probing time of 150, 160, and 170 ps after the start of the interaction, respectively.

Cf. a simplified theory Malkov M.A., Sagdeev R.Z. et al. Ion-acoustic shocks with self-regulated ion reflection and acceleration // Physics of Plasmas **23** (2016) 043105.

Early theory: Weibel instability of anisotropic plasma

PHYSICAL REVIEW E **82**, 016408 (2010)

Self-generation of megagauss magnetic fields during the expansion of a plasma

C. Thaury, P. Mora, A. Héron, and J. C. Adam
Centre de Physique Théorique, Ecole Polytechnique, CNRS, 91128 Palaiseau, France
(Received 4 December 2009; revised manuscript received 13 April 2010; published 27 July 2010)

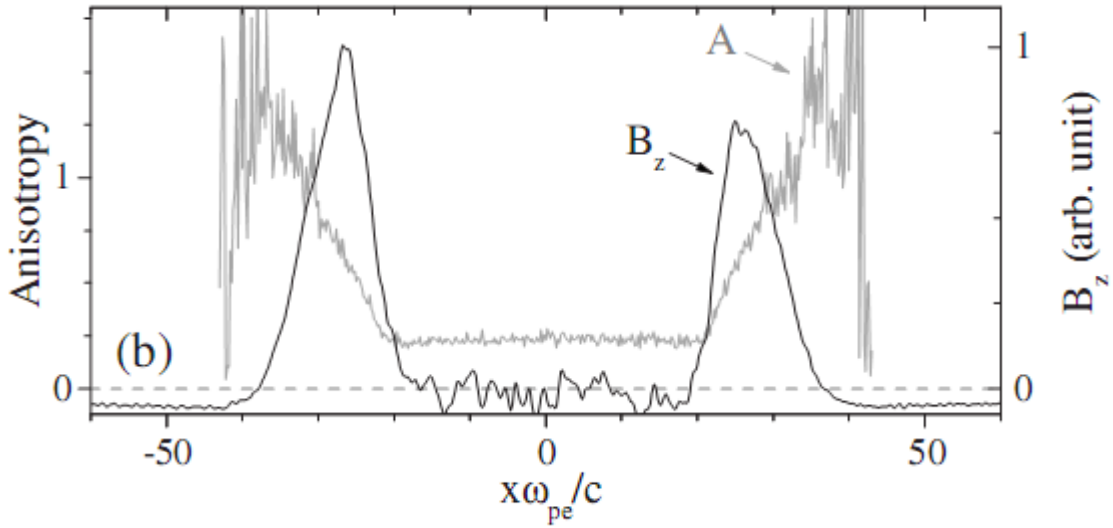

$$f_\alpha = \frac{m_\alpha^{3/2}}{(2\pi)^{3/2} T_{\perp\alpha} T_{\parallel\alpha}^{1/2}} \exp\left[-\frac{m_\alpha (v_x^2 + v_y^2)}{2T_{\perp\alpha}} - \frac{m_\alpha v_z^2}{2T_{\parallel\alpha}} \right]$$

$A_\alpha = T_{\parallel\alpha}/T_{\perp\alpha} - 1 > 0$ — an anisotropy degree.

Particle-in-cell simulations: parameters (EPOCH code)

2D3V

M/m = 100, Z = 1

$n_0 = 10^{20}$ cm^{-3}; $n_{bkg} = 10^{18}$ cm^{-3}

T_{eL} = 2.5 keV; $T_{e,bkg}$ = 50 eV

$T_{iL} = T_{i,bkg}$ = 3 eV

Grid: 600 x 2400 cells x 40 particles (1 Debye length per cell)

Simulated time period: 1000 T_{pl}

1D3V

M/m = 50 000, Z = 3

Grid: 6000 cells x 1000 particles (0.5 Debye length per cell)

Simulated time period: 100 000 T_{pl}

In the case of a weak discontinuity decay *(e.g., Medvedev Yu.V. PPCF* ***56*** *(2014) 025005)***, there are no a bump formation and a magnetic-field generation in addition to the well-known ion-acoustic soliton-oscillatory structure of a quasi-electrostatic shock wave.**

Particle-in-cell simulations: 2D3V

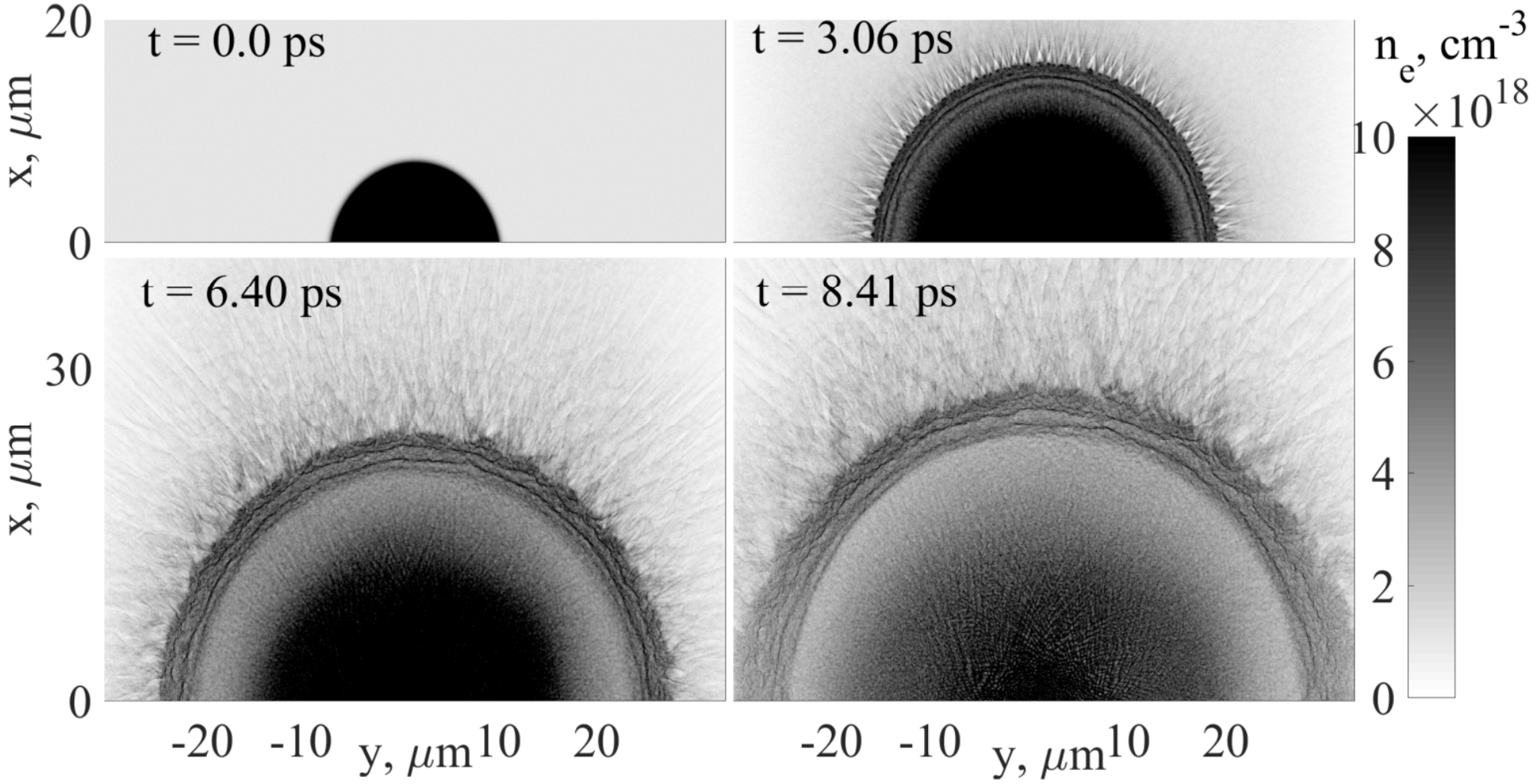

Dense plasma	Background
$N_0 = 10^{20}$ cm^{-3} ~ exp[-(x/L)^p]	$N_{bkg} = 10^{15}$–10^{19} cm^{-3}
Te = 2.5 KeV	Te = 50 eV
Ti = 3 eV	Ti = 3 eV

A. Nechaev, M. Garasev, V. Kocharovsky. Proc. of Laser Optics 2016. IEEE, 2016. P. R5-14

Particle-in-cell simulations: 1D3V

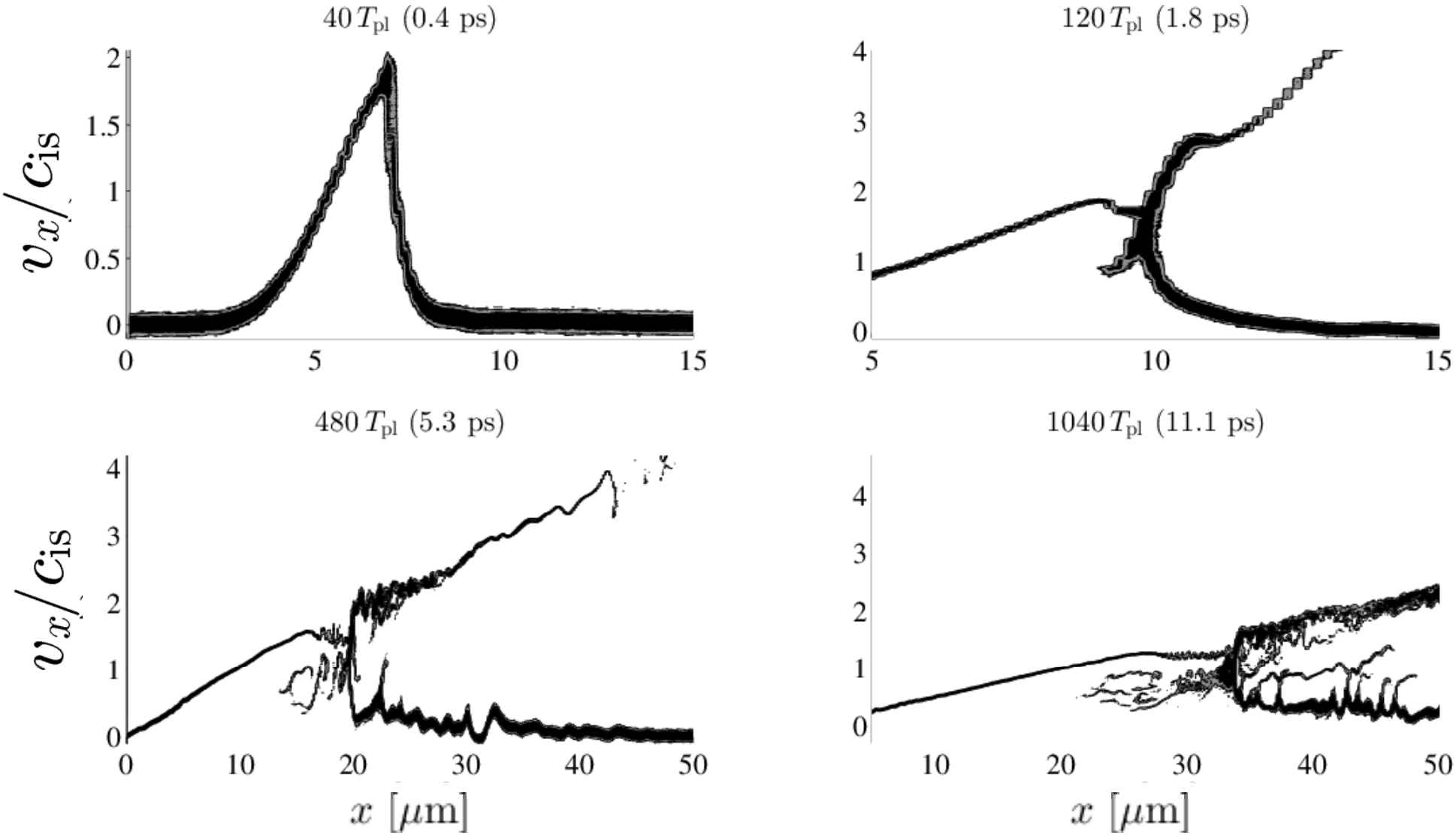

x–v_x phase space of the background ions (M = 100).

The kinetic effects suppress a formation of the ion-acoustic solitons.

Particle-in-cell simulations: Hot electron thermal pressure

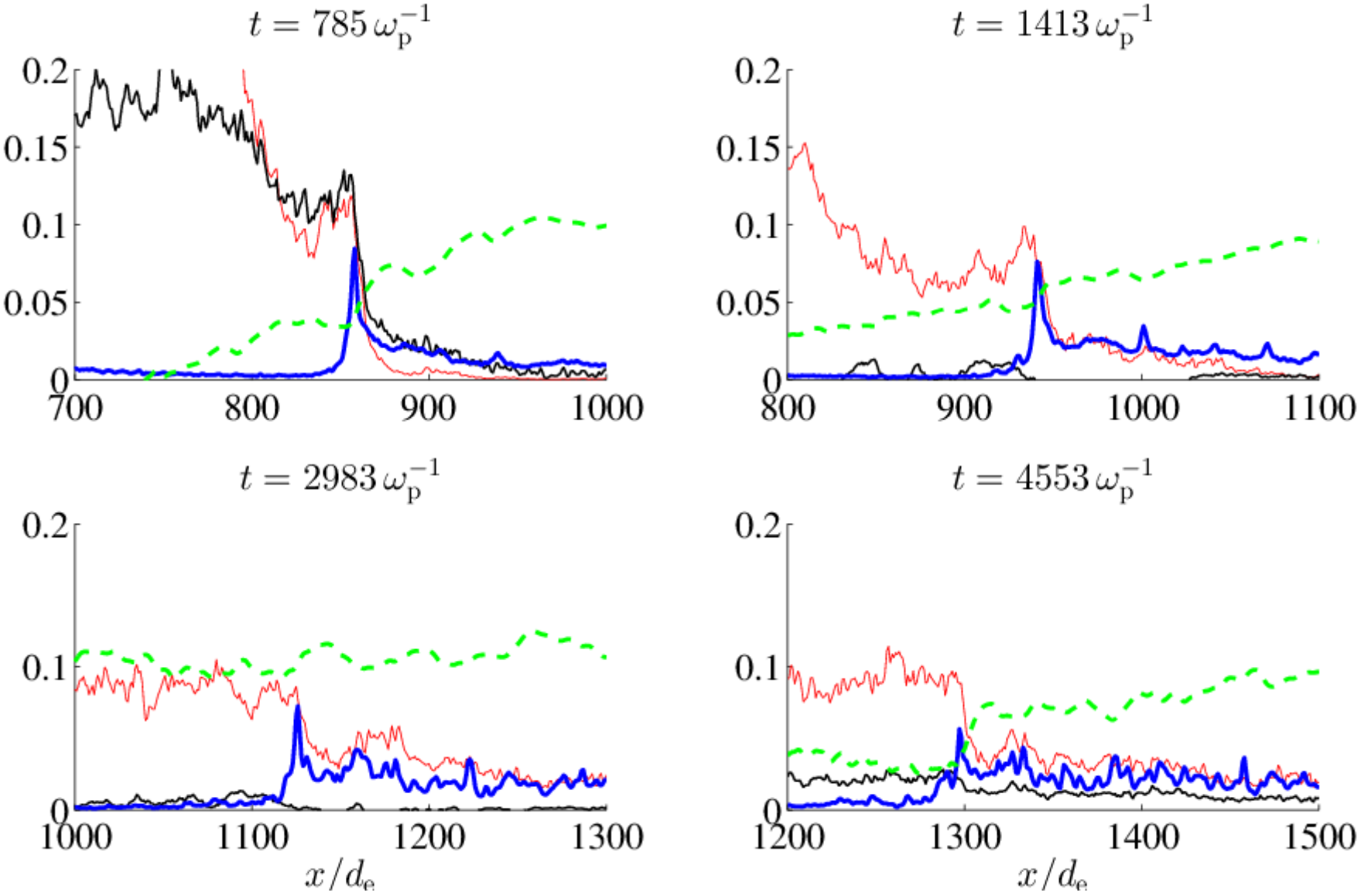

Nechaev A.A. et al.
Plasma Phys. Rep.
46 (2020) 765

W. Fox et al. Phys. Plasmas, 25, 102106 (2018)

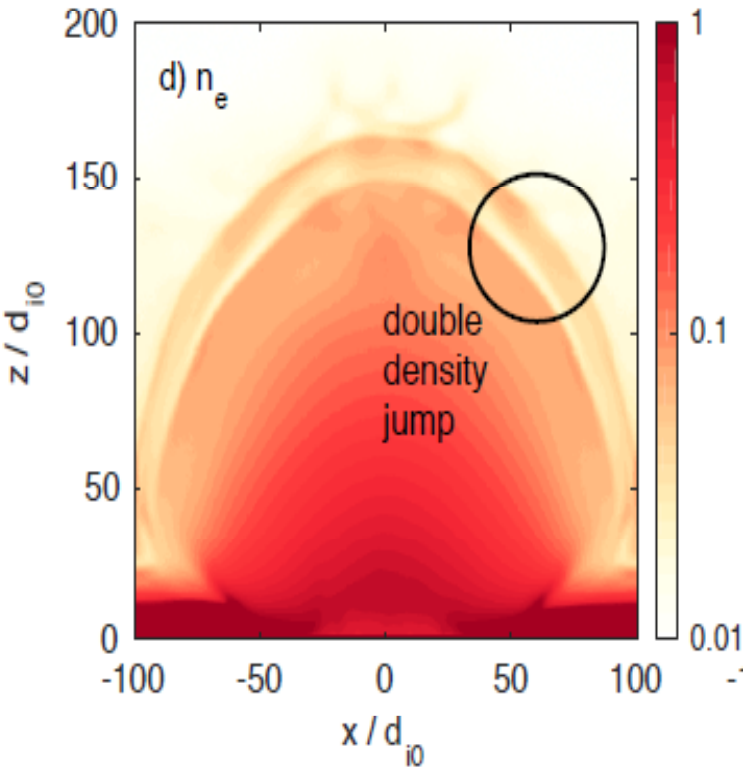

R_H = 340 mkm
d_{i0}=15 mkm
n_{bg}/n_0= 0.01
n_0=6·10^{20} cm^{-3}

M. E. Dieckmann et al. Phys. Plasmas, 24, 094501 (2017)

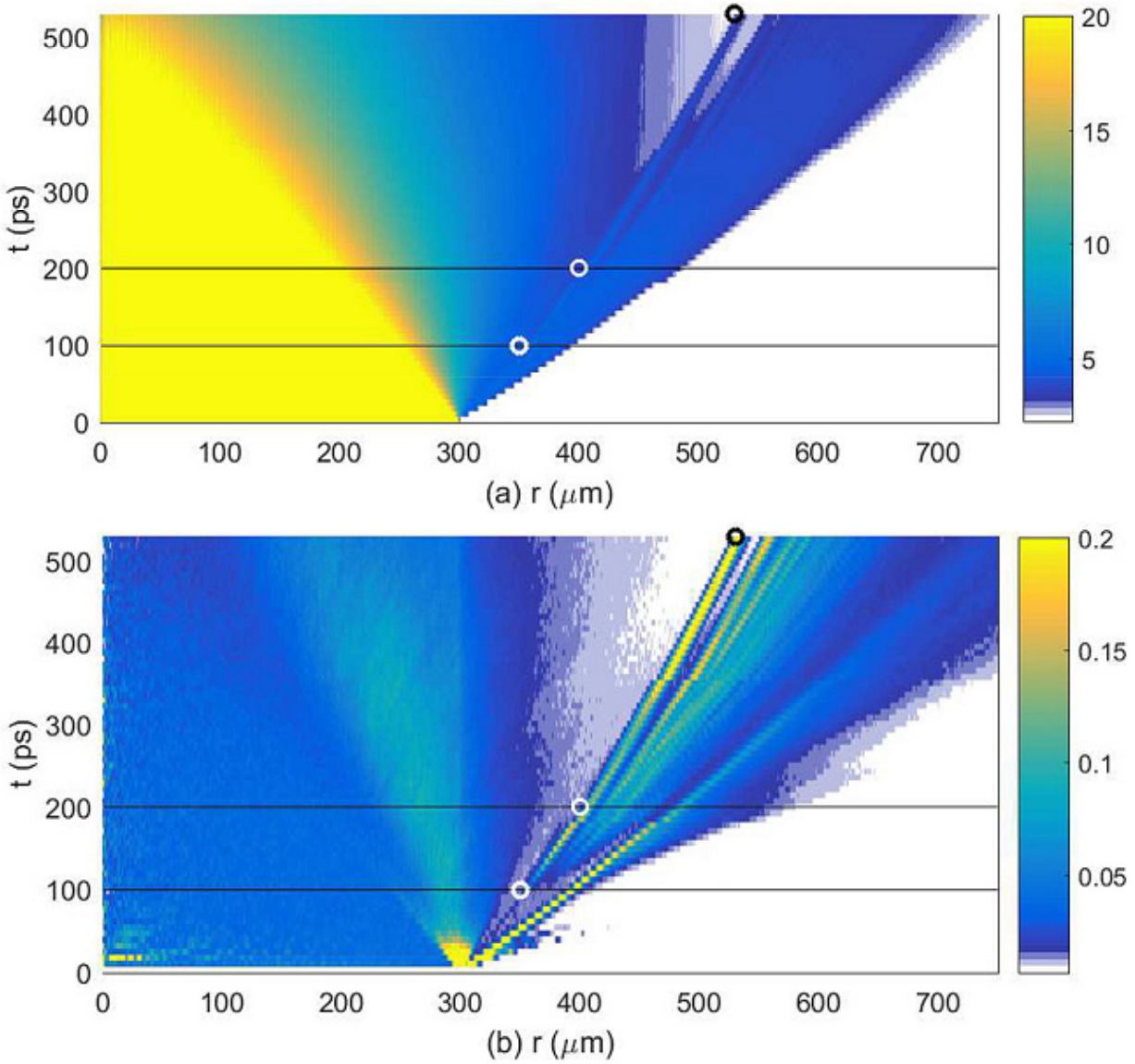

FIG. 1. Panel (a) shows the averaged proton density distribution $n(r, t)$. The linear color scale is clamped to a minimum of 2.2 and a maximum of 20. Lower and higher densities are thus not resolved by the color map. The averaged energy density $10^3 \cdot E_E(r,t)$ of the in-plane electric field is shown in panel (b). The linear color scale is clamped to 0.007 and 0.2. The horizontal lines denote the times $t = 100$ ps and $t = 200$ ps and the circles are explained in the text.

Particle-in-cell simulations: a magnetic field structure

Generation of magnetic field behind the front of a collisionless shock wave during the expansion of a laser plasma

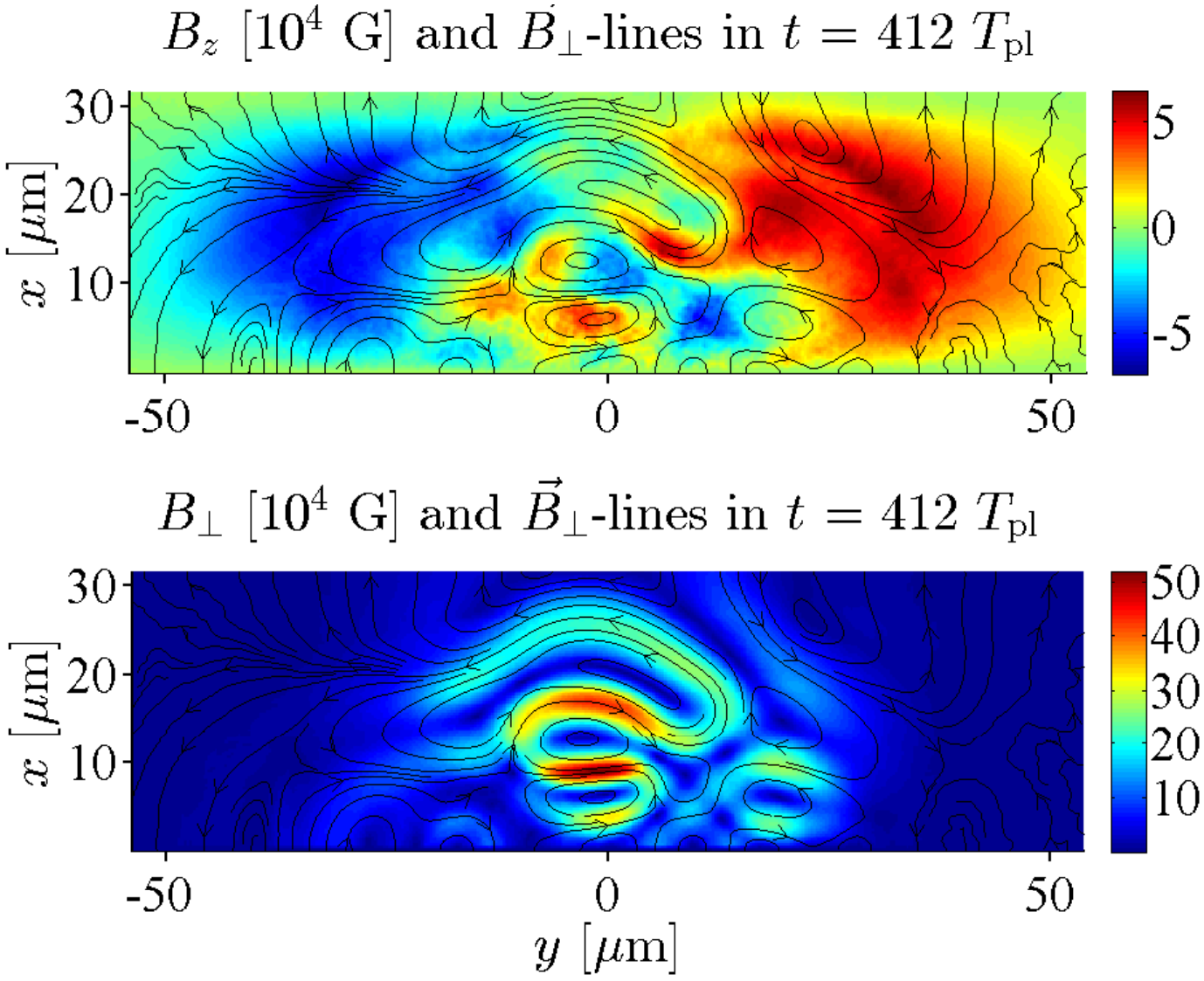

A. N. Stepanov et al. / Proc. of ICLO 2018. IEEE, 2018. P. 242.

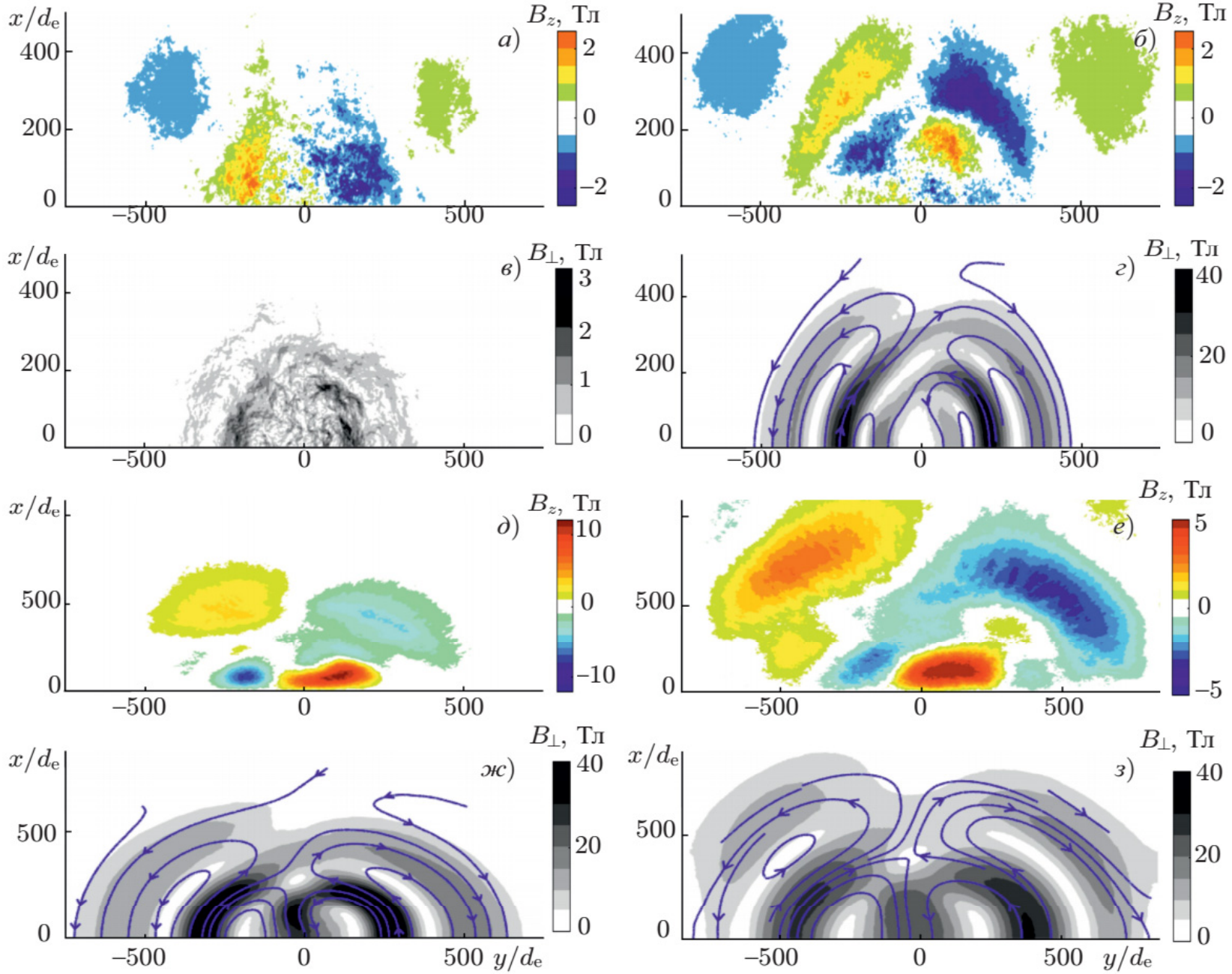

Nechaev A.A., Garasev M.A., Kocharovsky V.V., Kocharovsky Vl.V., Radiophys. Quant. Electr. **62** (2019) 932

Magnetic field components B_z (colour) and $B_\perp$ (black-white) at different moments of time: 1.8 ps, 2.7 ps, 3.7 ps, 5.7 ps. The magnetic field lines in the plane x,y are shown in blue

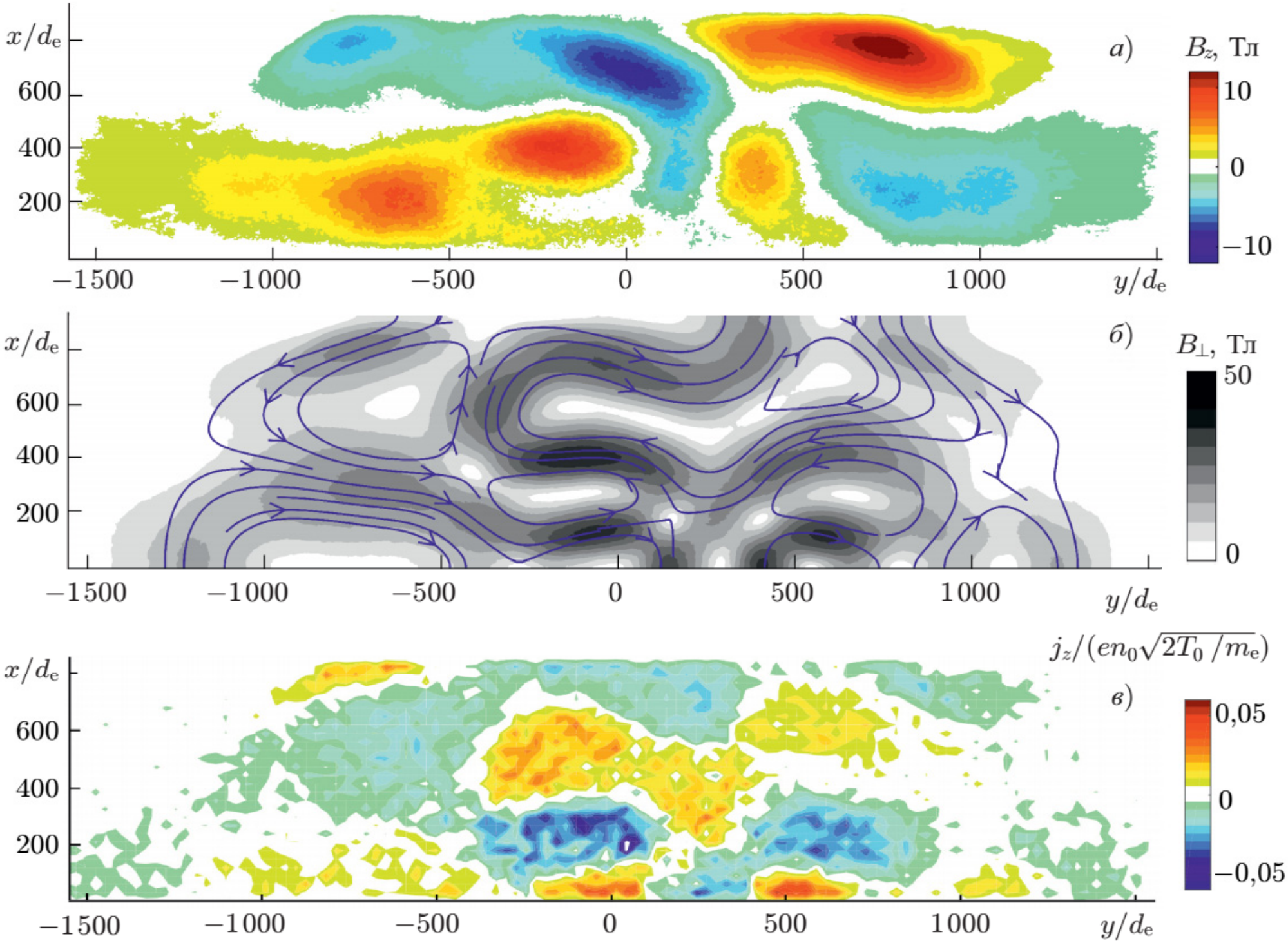

The same field components B_z,$B_\perp$ and a current component j_z at time 7.6 ps

Thermal anisotropy in an expanding plasma

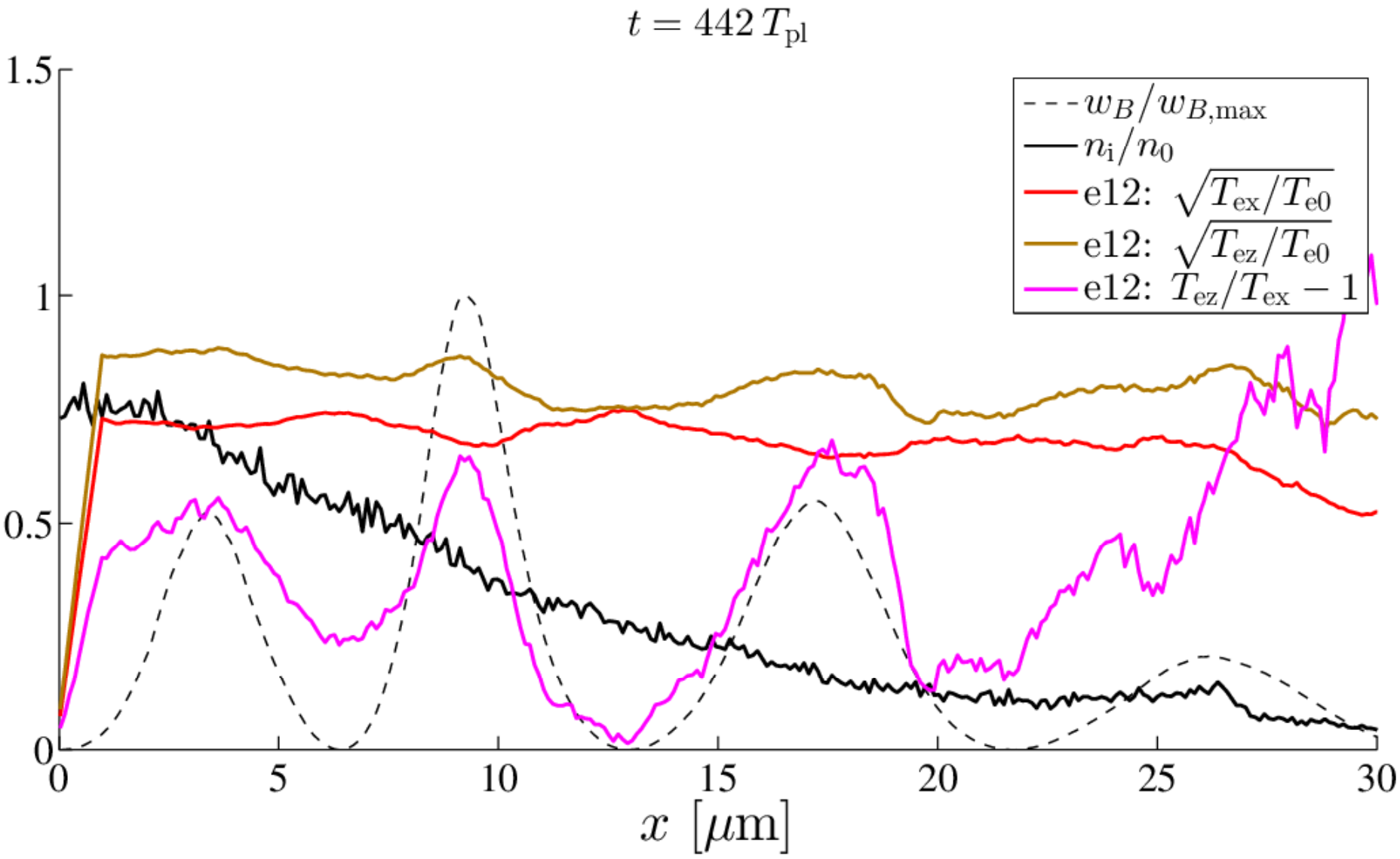

$$\Lambda_{opt} = 2\pi / K_{opt} \approx \frac{2\pi c}{\omega_{pe}} \sqrt{\frac{3}{A_e}} \approx 10\ \mu m$$

Conclusions on the problem # 2

1. The nonequilibrium hot electrons are responsible for the bump and shock wave formation. **They consist of both cold and accelerated ions which penetrate partially through the shock front if the initial plasma discontinuity is strong.** As a result, the long-term plasma dynamics is very different from the excitation and free propagation of the ion-acoustic solitons or oscillatory shock waves.

2. Generation of MG magnetic fields in an expanding plasma have been observed in experiments and numerical simulations.

3. It is shown that the large-scale field in front of the shock wave is formed due to a hot electron current streaming away from the target (cf. a fountain effect).

4. **The decrease in the longitudinal temperature of the hot electrons drives the Weibel instability which gives rise to the small-scale magnetic field and results in a spatial modulation of the electron temperature anisotropy.**

5. The Weibel mechanism for the growth of a magnetic field behind the shock is verified numerically. The dependency of the spatial structure of the Weibel fields and electric currents on the initial conditions is shown.

3. Different-type Weibel instabilities and coexistence of orthogonal current structures in adjacent regions of a plasma transition layer with a hot electron flow.

On the basis of numerical 2D3V particle-in-cell modeling using the EPOCH code, we found the features of the growth, evolution, and decay of different-scale current structures (sheets and filaments) during a finite-duration injection of a dense plasma with hot electrons into a layer of cold, rarefied plasma with a monotonically decreasing density.

The considered model corresponds to the collisionless expansion of a high-energy-density laser plasma produced as a result of **femtosecond ablation of a target by a cylindrically focused laser beam** and is typical for a number of problems in space and laboratory plasma physics.

In this case, the character of the anisotropy of the hot-electron velocity distribution function responsible for the Weibel-type instability depends significantly on the density of the background cold plasma.

The elucidation of the role of the discovered physical phenomenon in various problems of explosive transition processes in plasma astrophysics, including those in the presence of an external inhomogeneous magnetic field, and the experimental study of this phenomenon using petawatt femtosecond are of great interest.

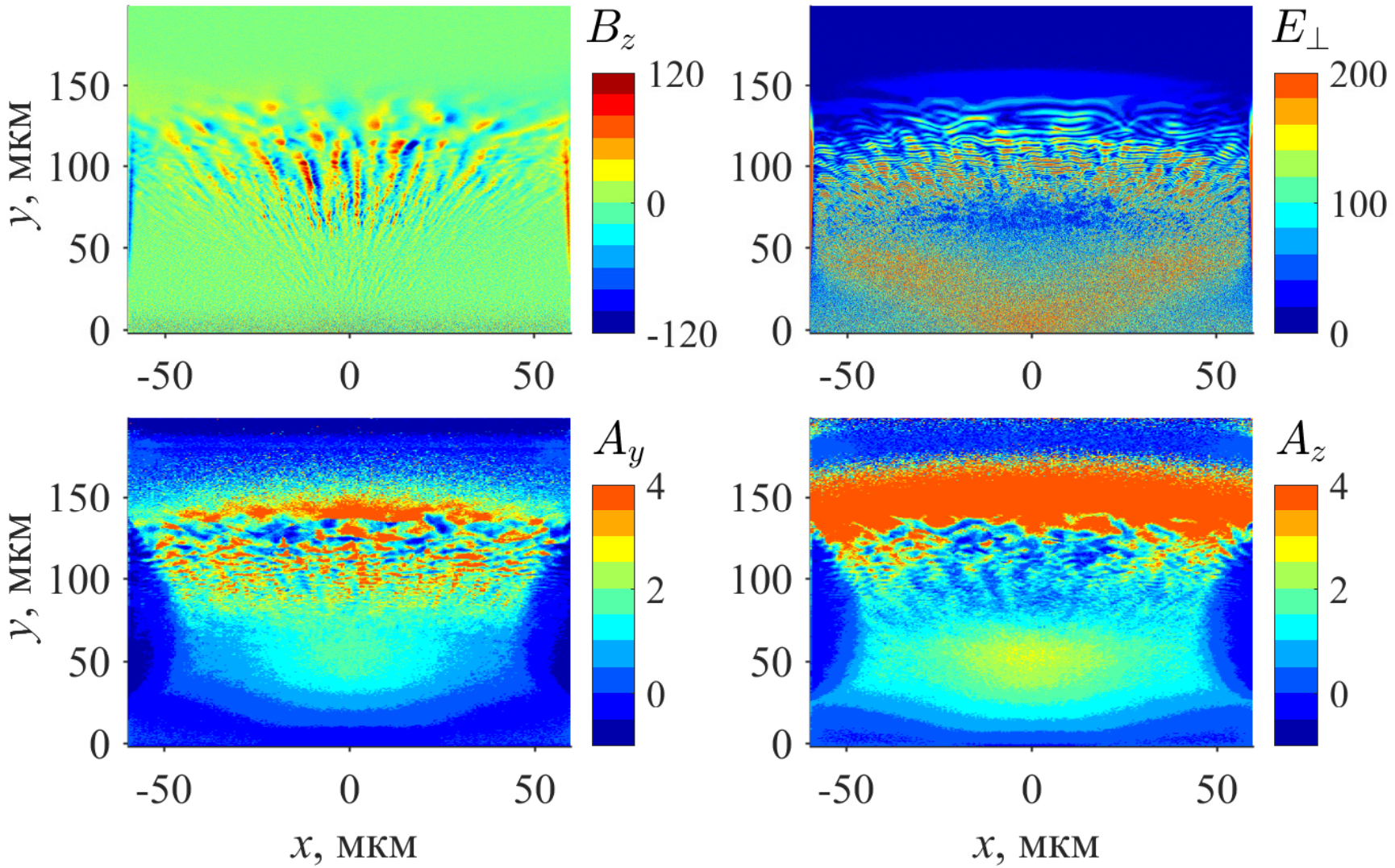

The spatial distributions of magnetic field B_z (top left, in T), transverse electric field $E_\perp = (E_x^2 + E_y^2)^{1/2}$ of (top right, in units of $3 \cdot 10^8$ V/m), anisotropy indices of $A_y = T_y/T_x - 1$ (bottom left) and $A_z = T_z/T_x - 1$ (bottom right) at $t = 0.7$ ps after the onset of injection of the plasma with hot electrons into the background plasma with an inhomogeneity scale of $L = 16$ μm at $n_0^* / N_0 = 0.03$.

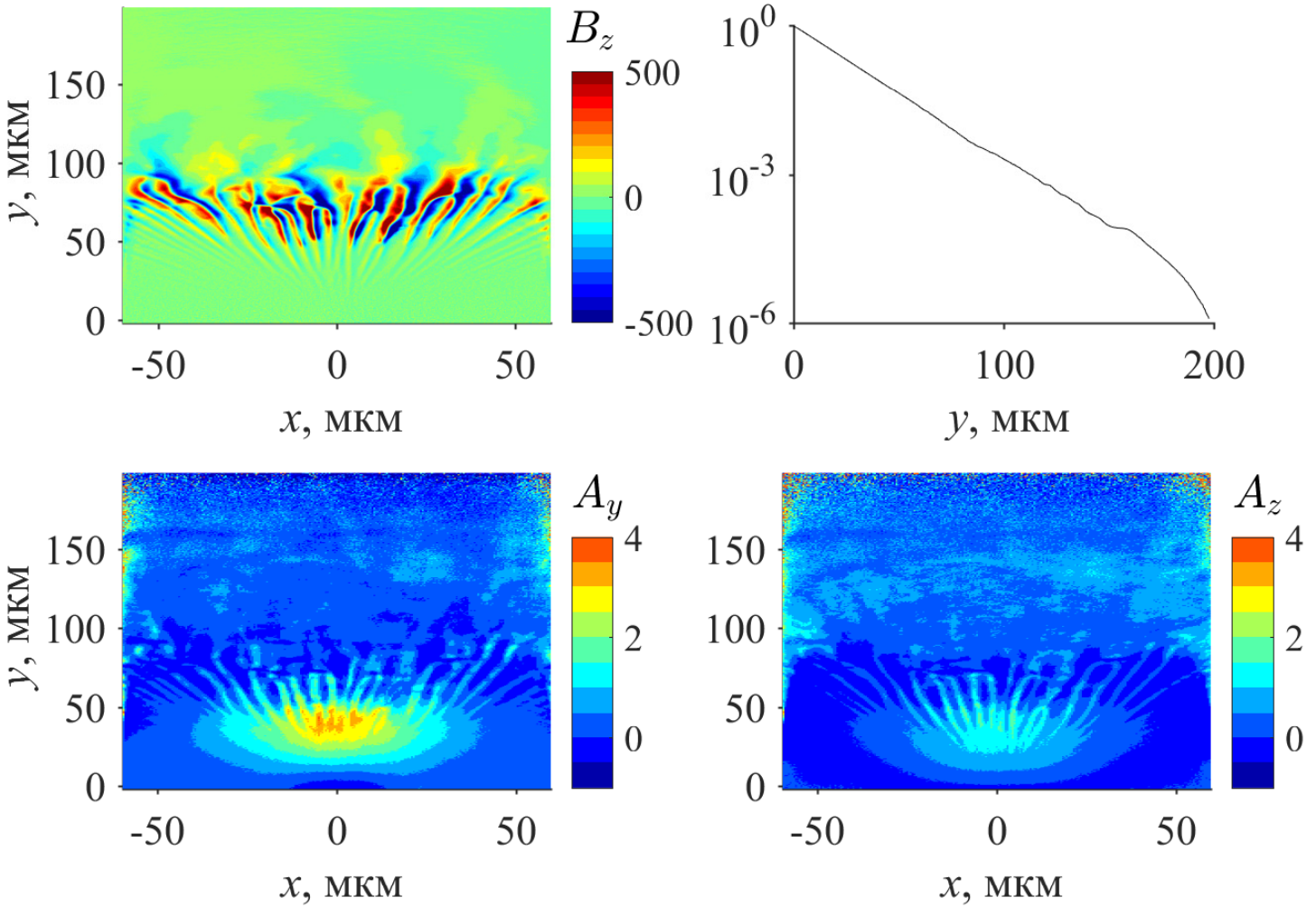

The structure of magnetic field B_z (top left, in T), plasma number density profile n/n_0 (top right), anisotropy indices of $A_y = T_y/T_x - 1$ (bottom left) and $A_z = T_z/T_x - 1$ (bottom right) at $t = 1.8$ ps after the onset of injection into the background plasma with an inhomogeneity scale of $L = 16$ μm at $n_0^*/N_0 = 0.03$. The bottom panels show the logarithm of the normalized number density, and the lines with arrows show the directions of the flow of cold background or hot electrons.

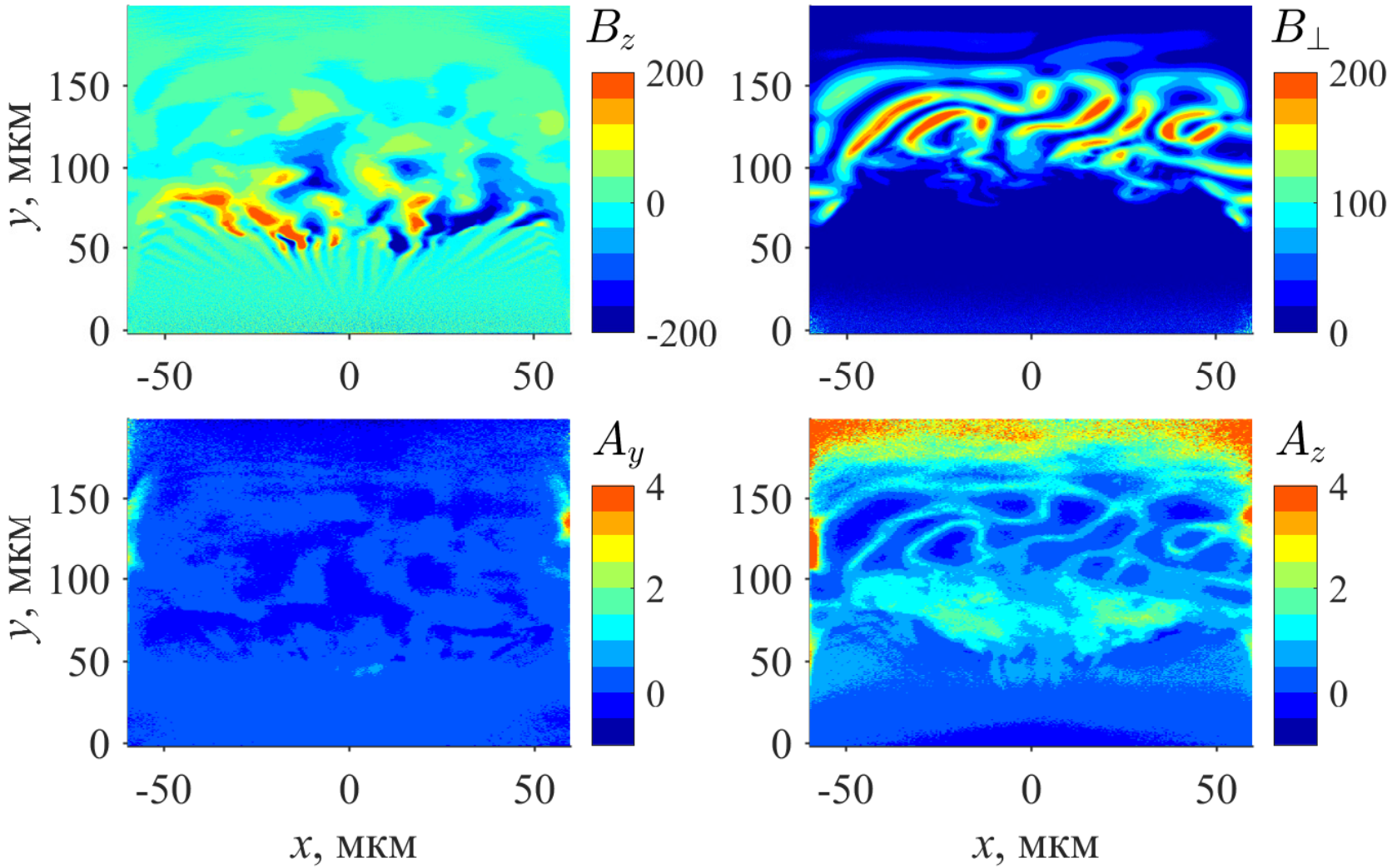

The structure of magnetic field B_z (top left, in T), transverse magnetic field of $B_\perp = (B_x^2 + B_y^2)^{1/2}$ (top right, in T), anisotropy indices of $A_y = T_y/T_x - 1$ (bottom left), and $A_z = T_z/T_x - 1$ (bottom right) at $t = 3.6$ ps after the onset of injection, which lasted 2 ps, of hot electrons into the background plasma with an inhomogeneity scale $L = 16$ μm at $n_0^* / N_0 = 0.03$.

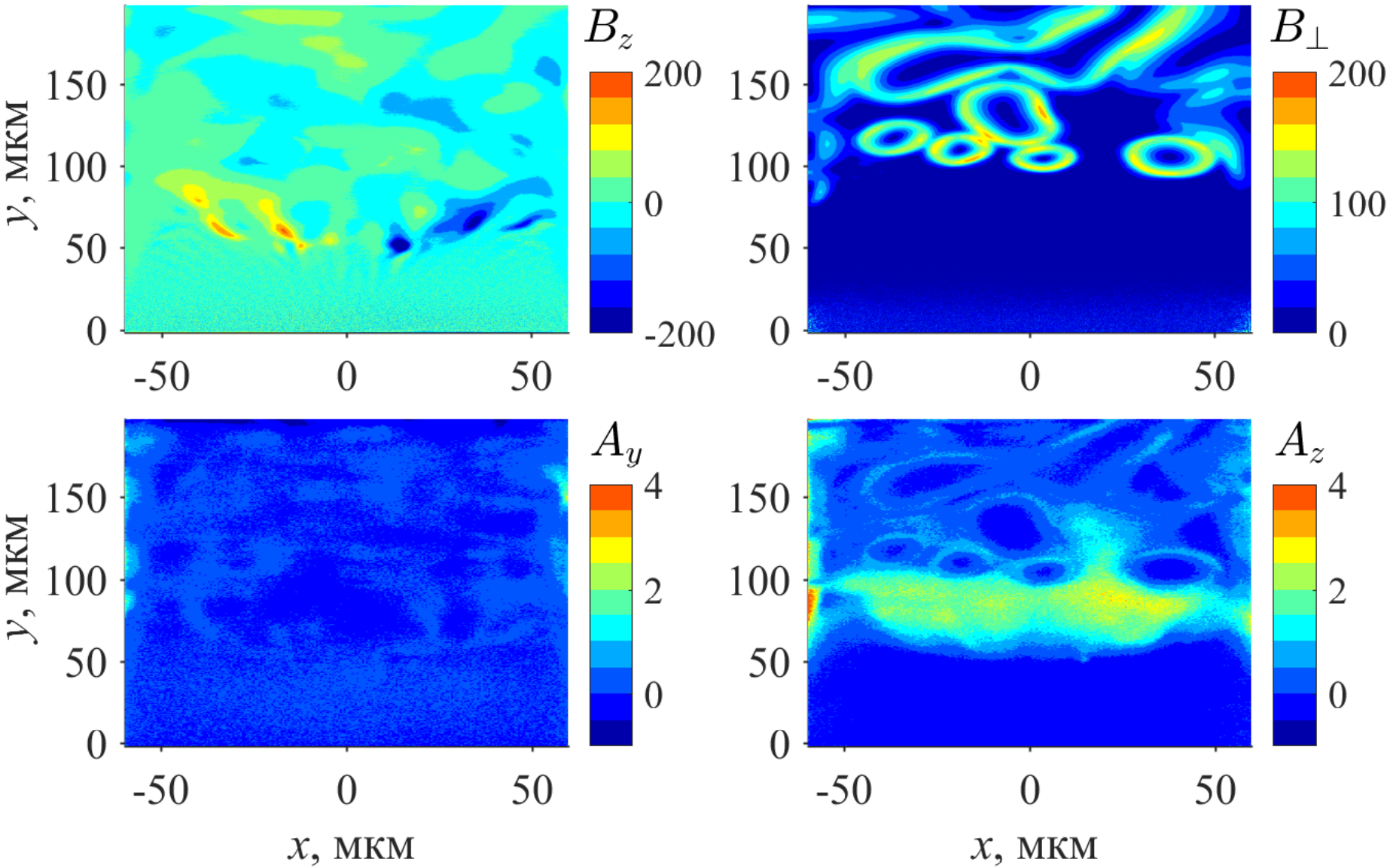

The same as in the previous figure at t = 6.6 ps.

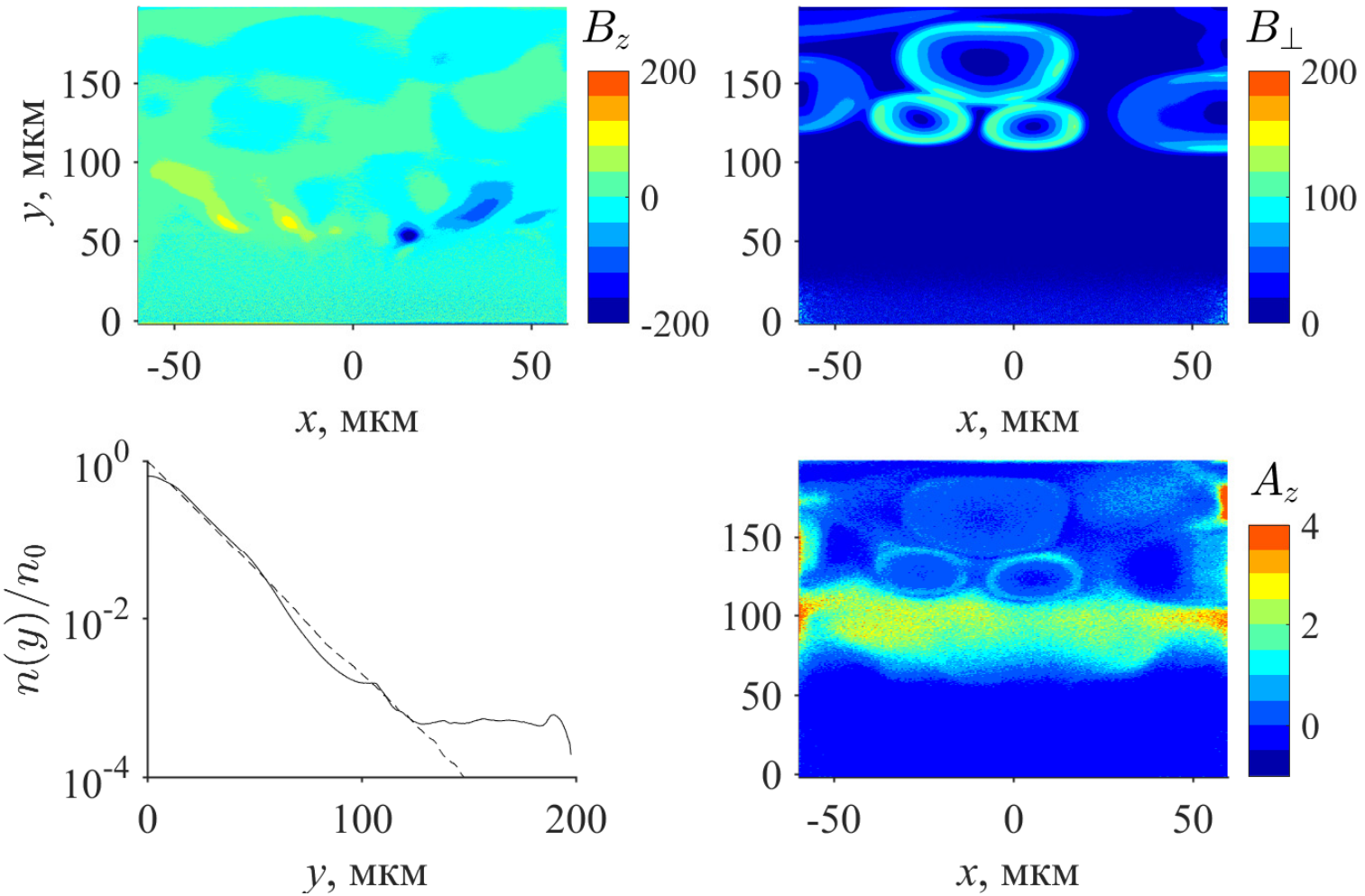

The structure of magnetic field B_z (top left, in T), transverse magnetic field of $B_\perp = (B_x^2 + B_y^2)^{1/2}$ (top right, in T), plasma density profile n/n_0 (bottom left, the solid line is for t = 10 ps and the dashed line is for t = 1.8 ps), and the anisotropy index of $A_z = T_z/T_x - 1$ (bottom right) at t = 10 ps after the onset of injection, which lasted 2 ps, of hot electrons into the background plasma with an inhomogeneity scale L = 16 μm at $n_0^*/N_0 = 0.03$.

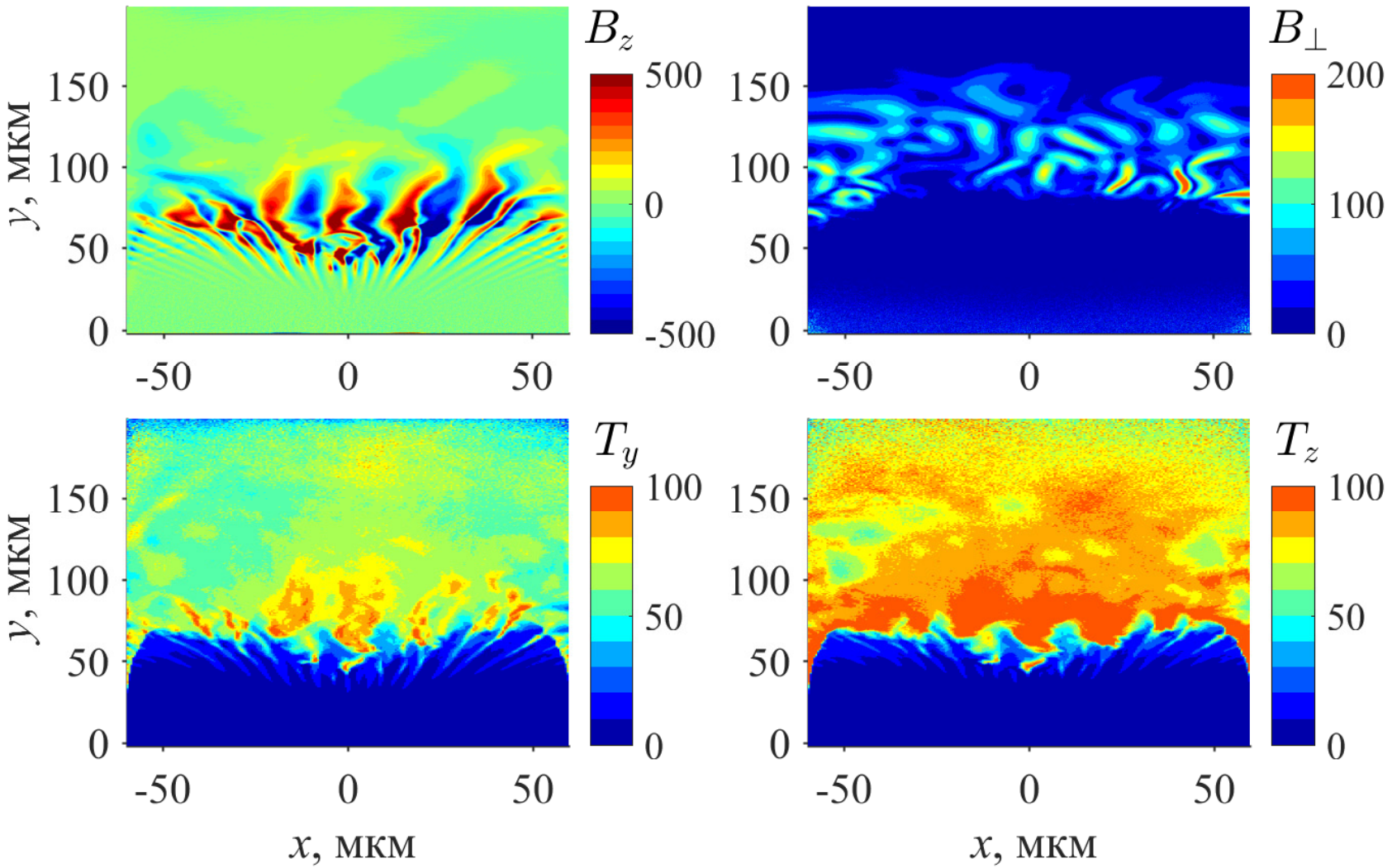

The tructure of magnetic field B_z (top left, in T), transverse magnetic field of $B_\perp = (B_x^2 + B_y^2)^{1/2}$ (top right, in T), effective temperature T_y and T_z (bottom left and right, in eV) at $t = 3.6$ ps after the onset of injection, which lasted 5 ps, of hot electrons into the background plasma with a scale of inhomogeneities of $L = 16$ μm at $n_0^* / N_0 = 0.03$.

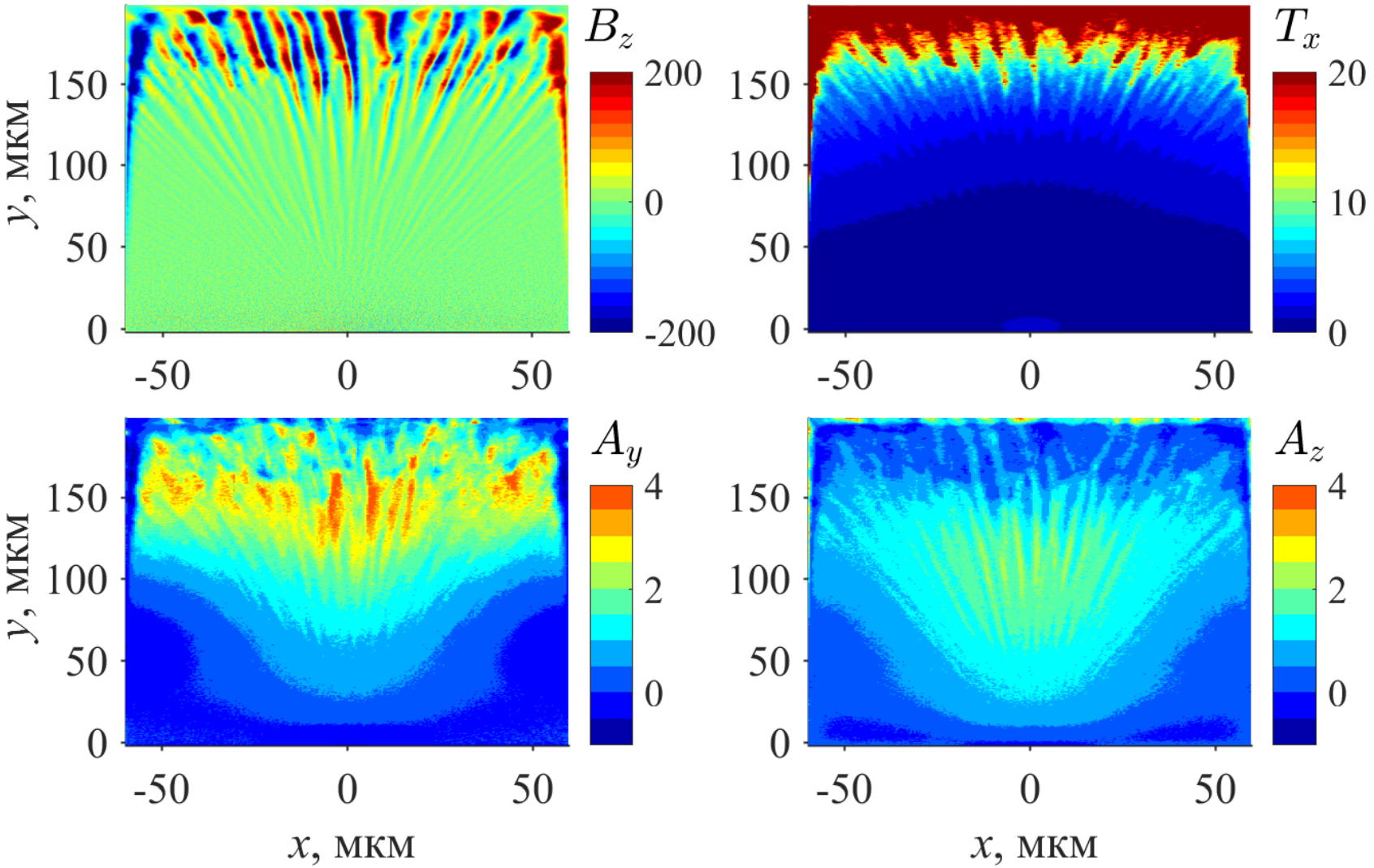

The structure of magnetic field B_z (top left, in T), effective temperature T_x (top right, in eV), anisotropy indices of $A_y = T_y/T_x - 1$ (bottom left) and $A_z = T_z/T_x - 1$ (bottom right) at $t = 1.8$ ps after the onset of injection of hot electrons into the background plasma with a scale of inhomogeneities of $L = 32$ μm at $n_0^*/N_0 = 0.03$.

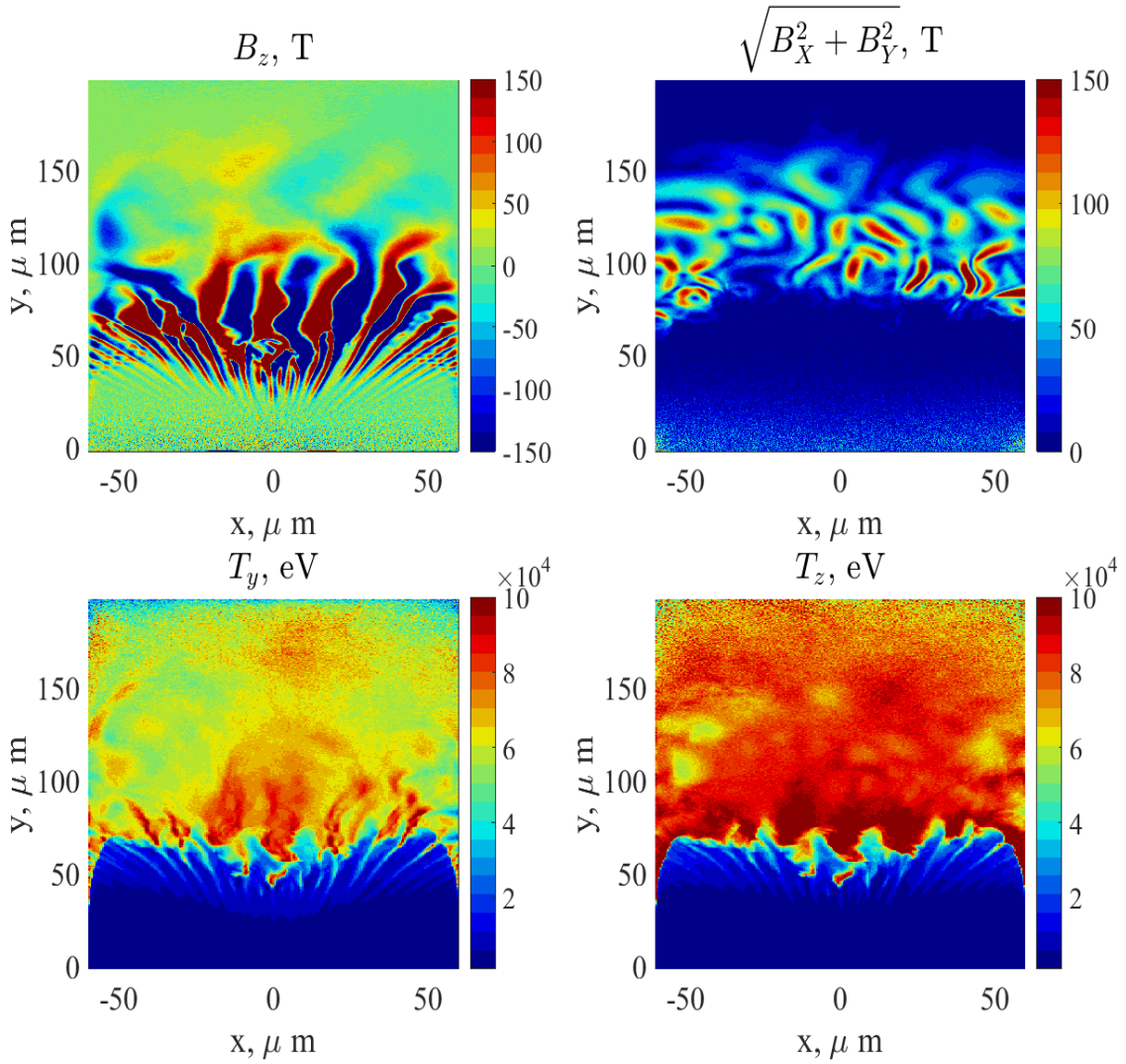

Structure of the longitudinal, B_z, and transverse, $B_\perp = (B_x^2+B_y^2)^{1/2}$, magnetic fields in Tesla (upper left and right) as well as the effective temperatures T_y and T_z in eV (lower left and right) at t = 3.6 ps after the start of the injection of hot electrons (which lasted for 2 ps) from the target surface into the background plasma with an inhomogeneity scale L = 32 μm at an injection ratio n_0^*/N_0 = 0.03 of the densities of hot and background electrons for a semi-cylindrical form of the hot-electron spot elongated along the surface of the plasma boundary where the cylindrical axis z is lying.

Conclusions on the problem # 3

1. As a result of a femtosecond ablation of a target by **a cylindrically focused laser beam**, two qualitatively different Weibel mechanisms for the generation of mutually orthogonal current structures can take place. They produce strong and also mutually orthogonal magnetic fields in adjacent plasma layers between which the plasma density experiences a rather sharp drop.

2. In a denser layer, the anisotropy axis is oriented along the initial direction of the electron injection, and in a less dense layer, it is transverse to this direction. **In the first layer**, the electron distribution is formed by a cold thermal background and a gradually relaxing hot flow, while **in the second layer** it is similar to the bi-Maxwellian distribution of hot electrons.

3. In the direction of the anisotropy axis in each layer, current structures emerge in the form of either wedge-shaped inhomogeneous **current sheets** (filamentation Weibel instability), or deformed partially hollow **z-pinches** (thermal Weibel instability), respectively. After the end of the injection, the latter decay much slower than the former due to the nonlinear effects of electron trapping and exhibit a lifetime that is much longer than the duration of the injection.

4. The revealed phenomenon of the formation of two orthogonal different-scale current structures and the corresponding magnetic fields during the injection of hot electrons into a strongly inhomogeneous cold plasma is relevant also to other geometries and ablation models.

5. Similar phenomena are expected at the initial stage of cosmic explosive processes, e.g., during heating of density ducts in the solar wind, stellar coronas, or magnetospheres.

4. A decay of a strong elongated quasi-one-dimensional discontinuity in a plasma with hot electrons in the presence of an external magnetic field

Analysis of the expansion of a plasma that fills a half-space and has a quasi-one-dimensional semi-cylindrical region with isotropically heated electrons elongated along its boundary showed that the presence of **an external magnetic field parallel to the boundary of the initial strong discontinuity of the plasma density**, in a wide range of parameters, strongly affects the dynamics of formation and the spatial structure of the self-consistent magnetic field created by currents of anisotropically expanding electrons.

An experiment is underway.

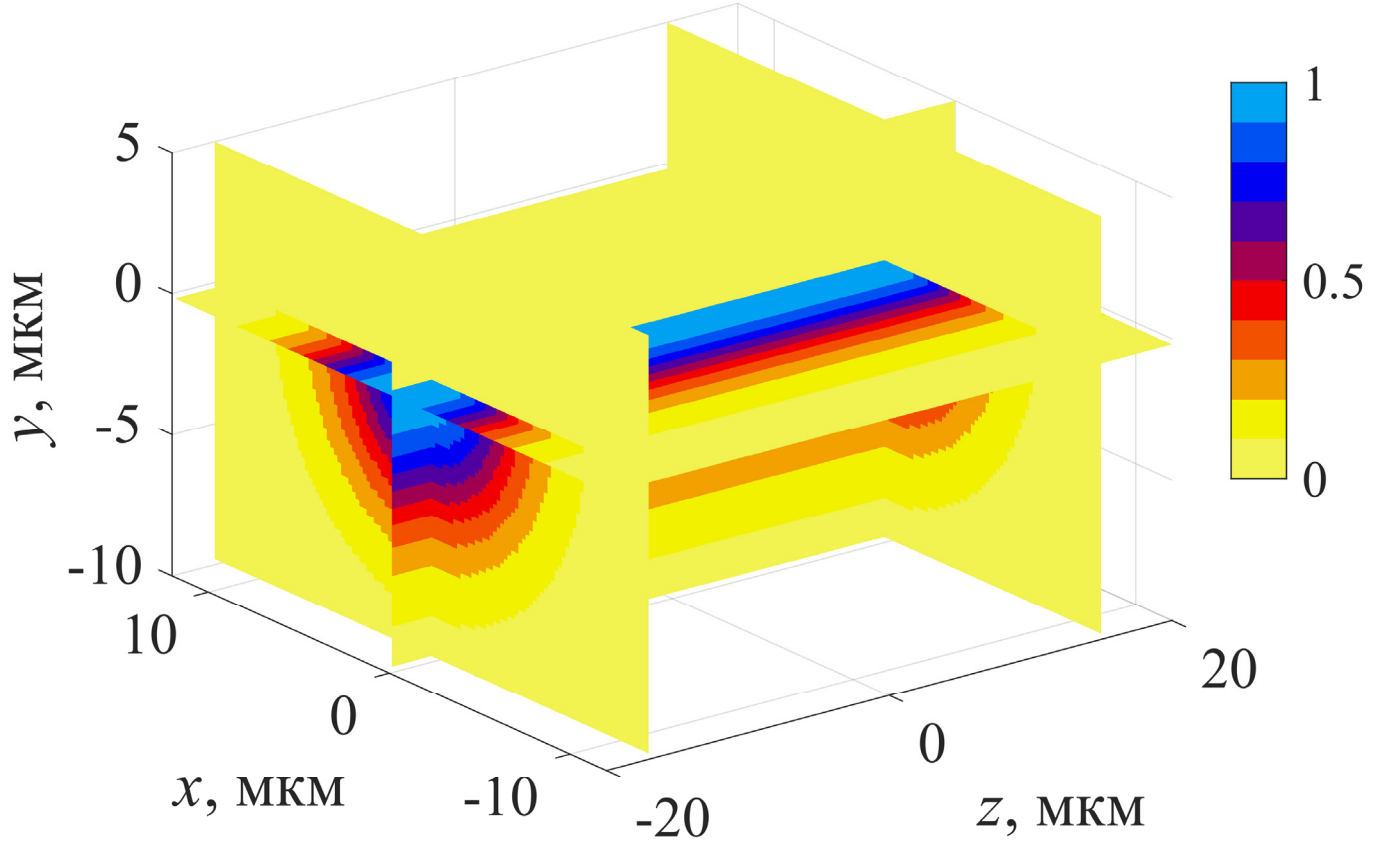

Initial temperature of hot electrons in a semi-cylindrical region of a target.

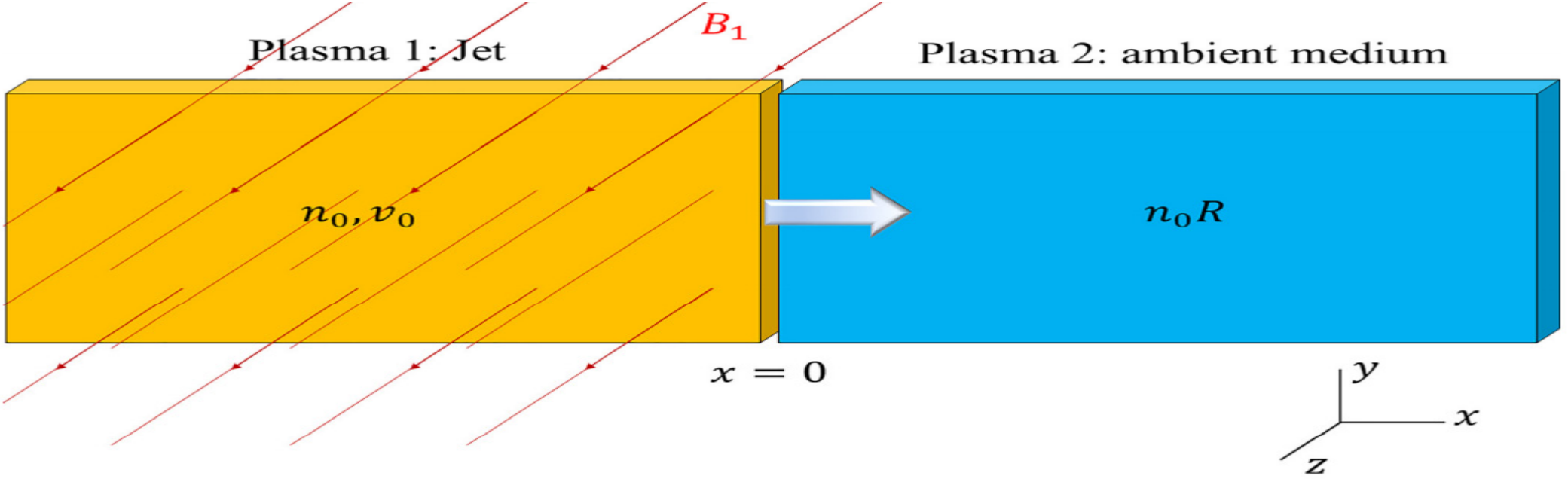

FIG. 1. Sketch of the initial plasma density distribution and magnetic field in the simulations.

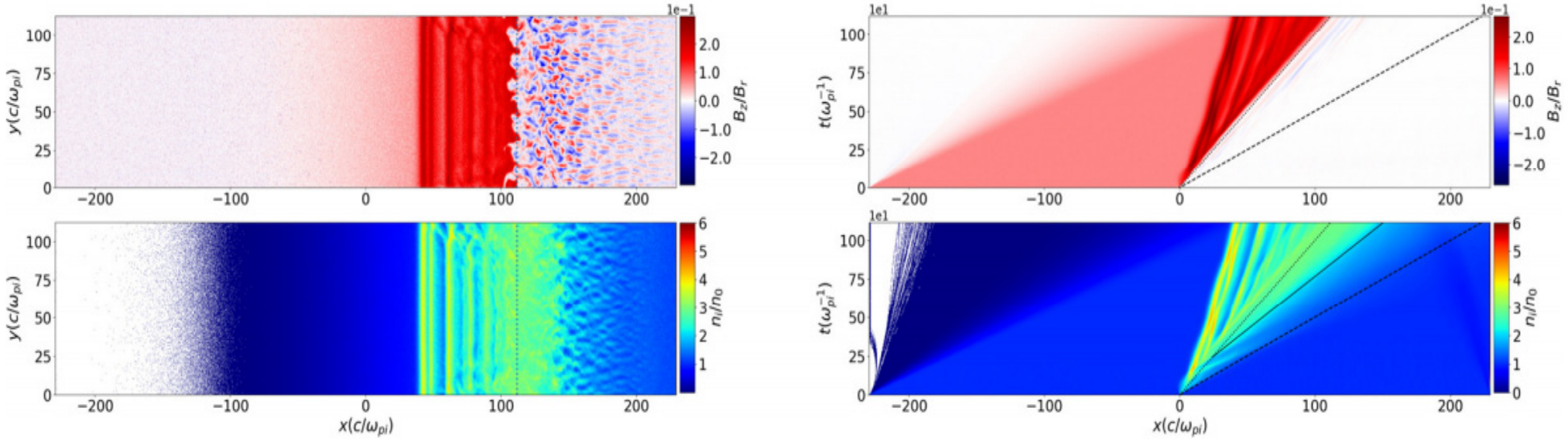

FIG. 8. Magnetic field (top) and ion density (bottom, clamped at 6 for visualization reasons) at time $t = t_{max} = 1118\omega_{pi}^{-1}$ (left) and their evolution with time (right). The speeds v_f, v_c, and v_0 are overplotted by solid, dotted, and dashed lines, respectively. The mass ratio is $\mu = 20$.

Particle-in-cell simulations with a magnetic field
B_x=0, 2, 13, 250 T or B_z=0, 13, 250 T (EPOCH code)

2D simulation area:

$L_y * L_x$ = 36 μm * 36 μm (i.e., 1200 * 1200 cells)

Plasma layer has a step density profile without pre-plasma:

$n_0 = 10^{22}$ cm^{-3} = $10n_{critical}$ (or up to $n_0 = 10^{20}$ cm^{-3}),

width = 9 μm, $M_{ion} = 100\ m_{electron}$ (or M_i/m_e=400),

Initially heated semi-cylinder: $T_e = T_{e0} + T_{e1}*\exp(-(r/r_0)^2)$,

T_{e0} = 10 eV, T_{e1} = 1000 eV, r_0 = 8 μm.

A preview

The possibility of the appearance of **magnetic fields of various structures, significantly exceeding the external magnetic field in magnitude**, is demonstrated, primarily in the form of multiple expanding z-pinches parallel to the external magnetic field, and slowly evolving current sheets oriented at different angles to the boundary between the plasma and the deformed magnetic field. Such structures can be essential for a number of processes in laser and space plasma, including explosive processes in the magnetospheres of planets and in the coronal arches of stars.

The expansion of a plasma with hot electrons (with initial concentration $n_0 = 10^{20}$ cm^{-3}) into a vacuum **without an external magnetic field** at time $t = 20$ ps. Top left panel — magnetic field magnitude (in Tesla). Lower left panel — the logarithm of normalized plasma concentration. The upper and the lower panels on the right show the effective temperatures (in eV) along the x and y axes respectfully.

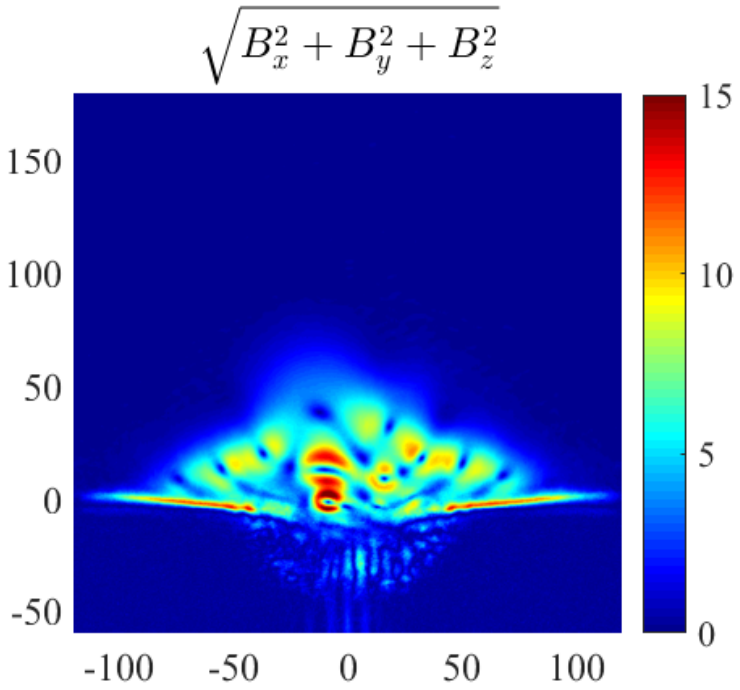

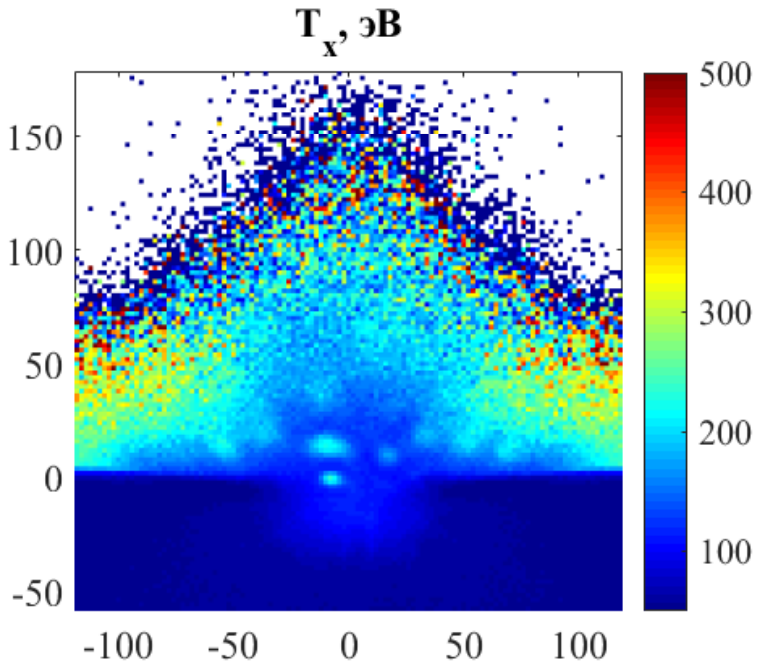

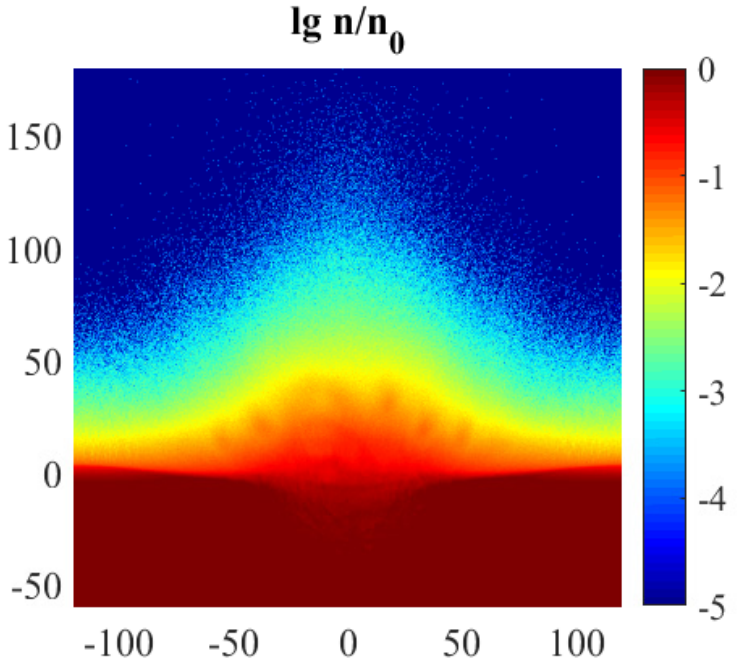

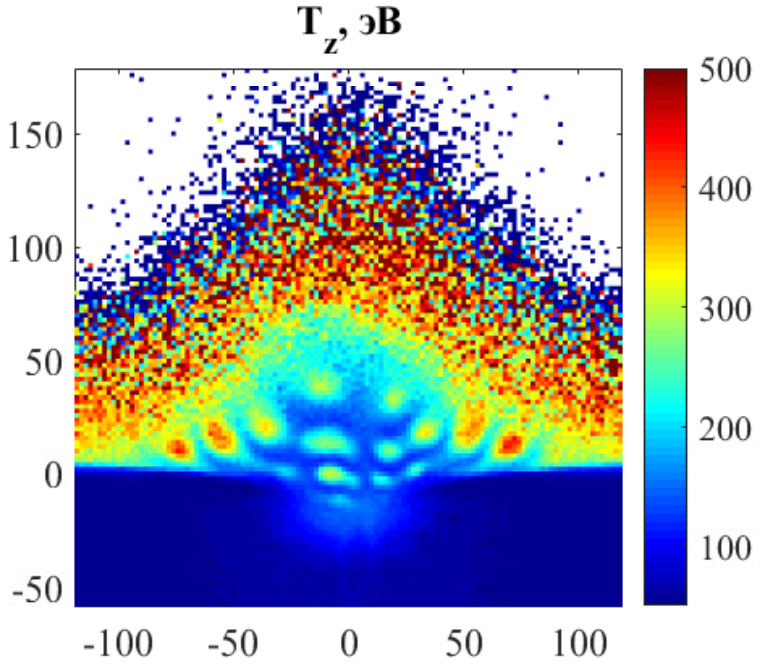

The expansion of a plasma with hot electrons (with initial concentration $n_0 = 10^{20}$ cm^{-3}) into **an external magnetic field B_z = 13 T** at time t = 20 ps. Top left panel — magnetic field magnitude (in Tesla), top right panel — the effective temperature (in eV) along the x axis. Lower left and right panels — effective temperatures along the y and z axes respectfully.

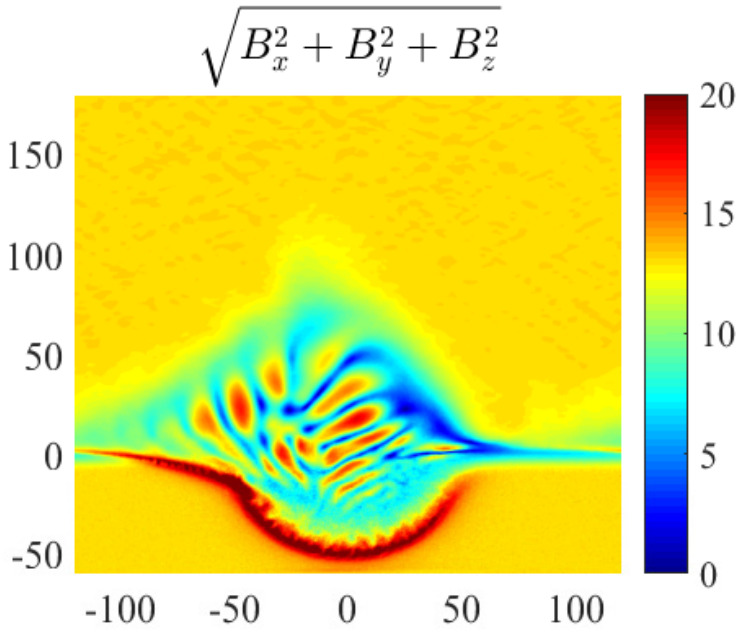

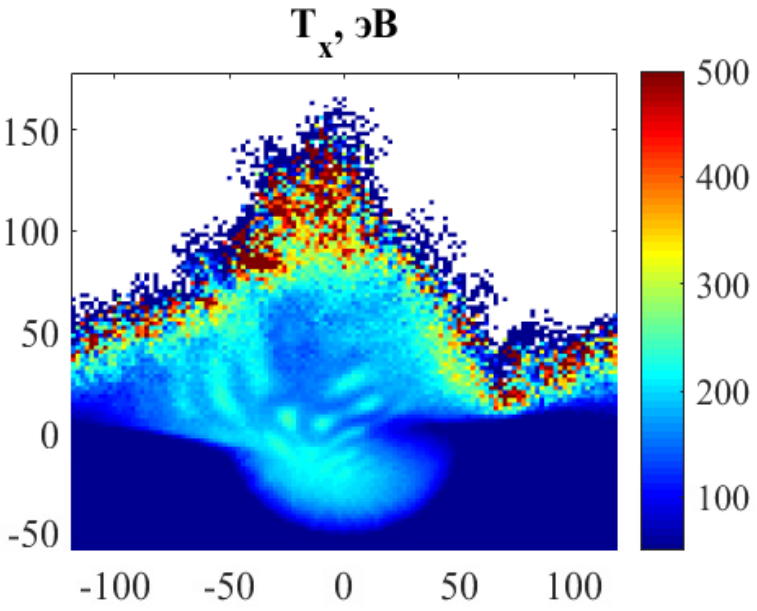

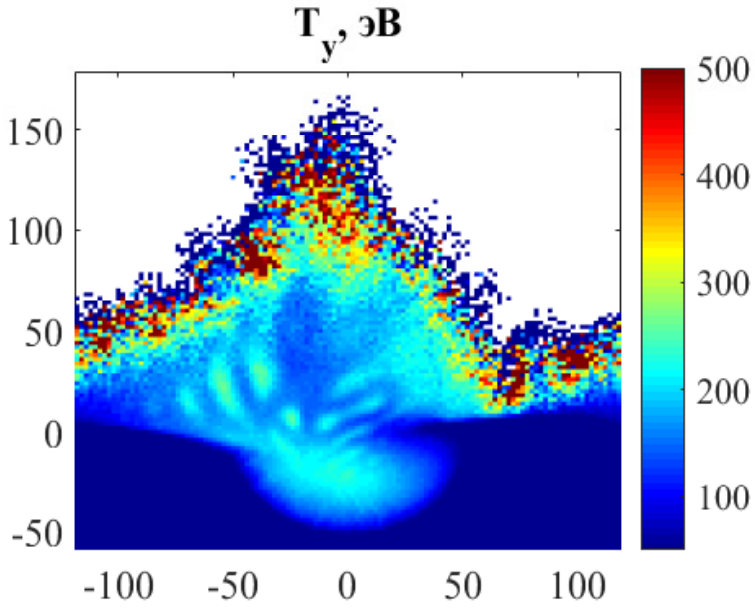

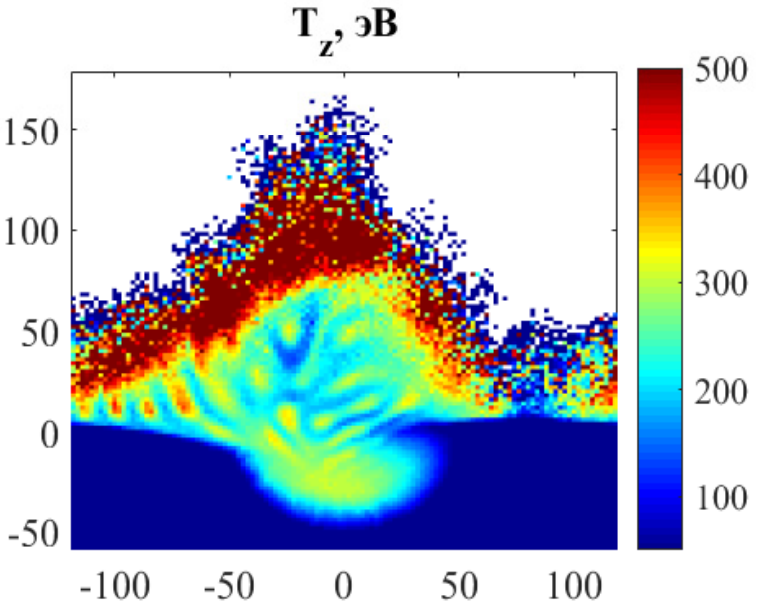

The expansion of a plasma with hot electrons (with initial concentration $n_0 = 10^{20}$ cm^{-3}) into an **external magnetic field B_x = 13 T** at time t = 20 ps. Top left panel — magnetic field component B_z (in Tesla). Top right panel — magnitude of the in-plane magnetic field (in Tesla), arrows show the direction of the in-plane field. Lower left panel — magnetic field component B_x minus the external field. Lower right panel — the logarithm of normalized plasma concentration.

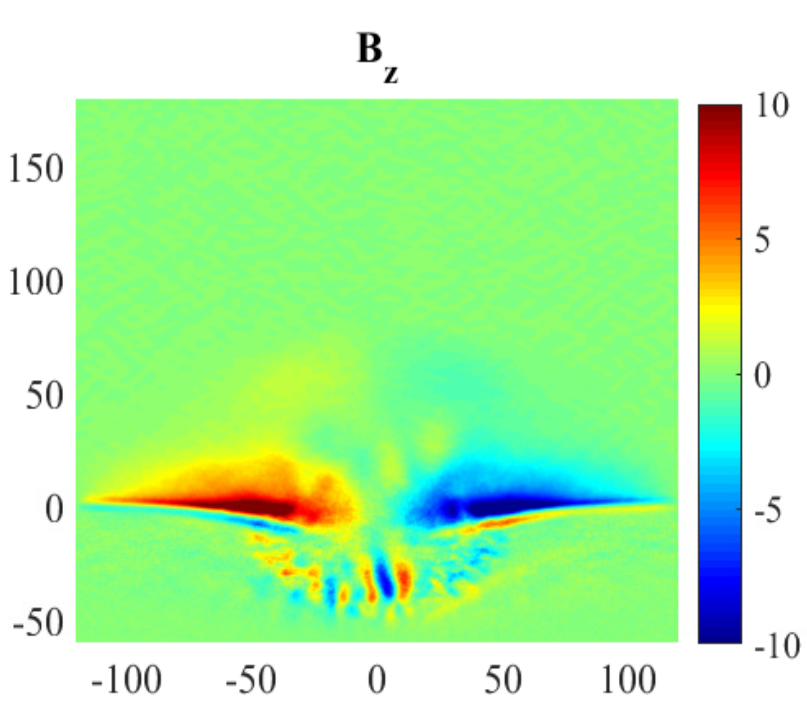

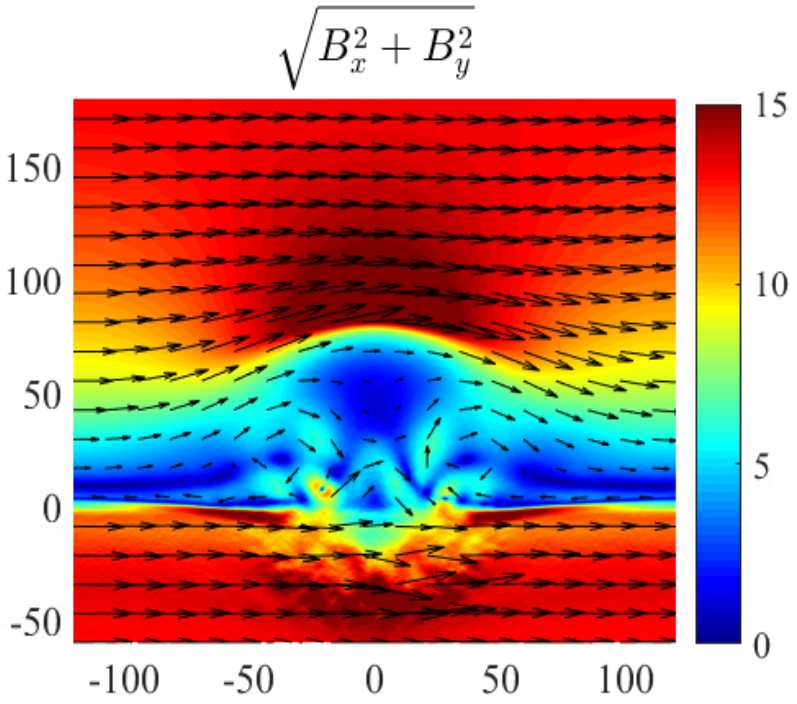

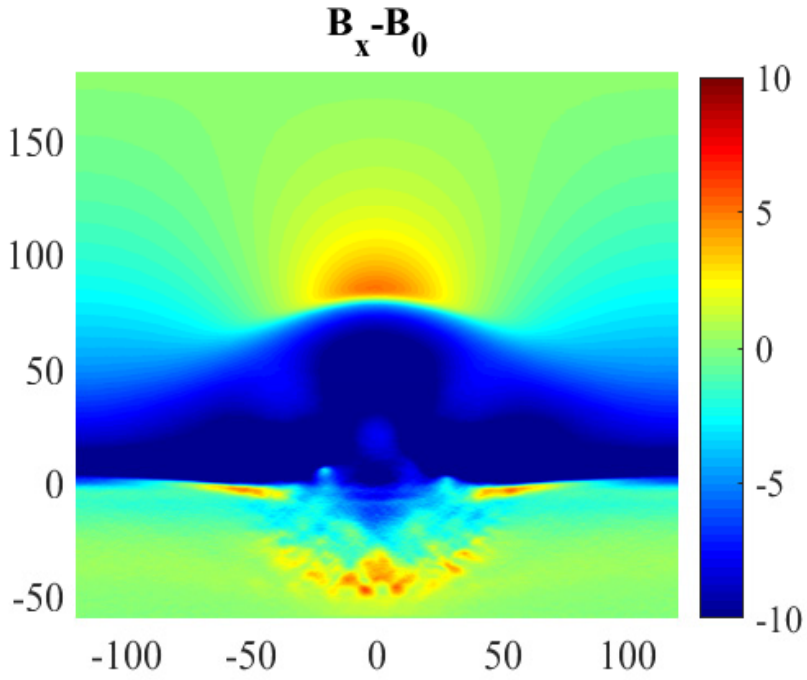

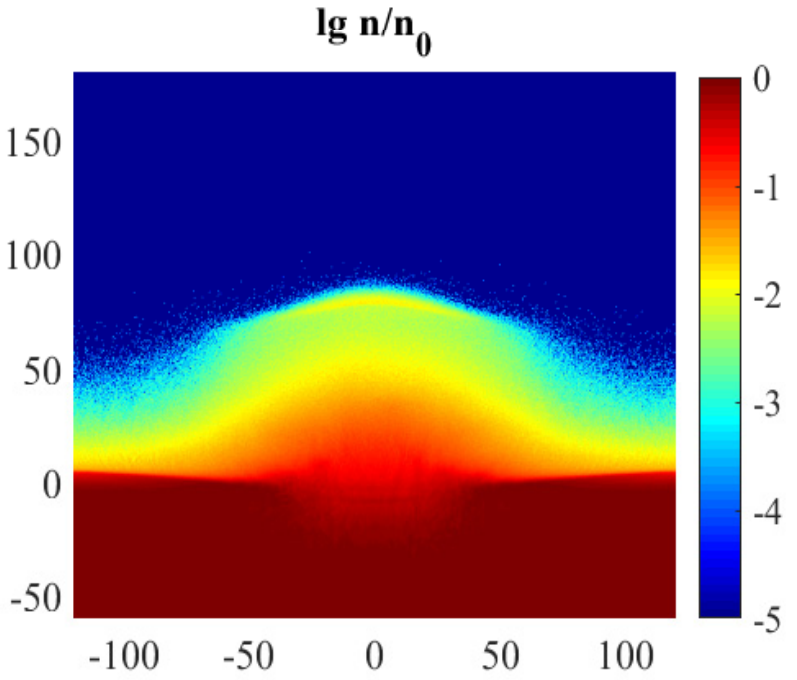

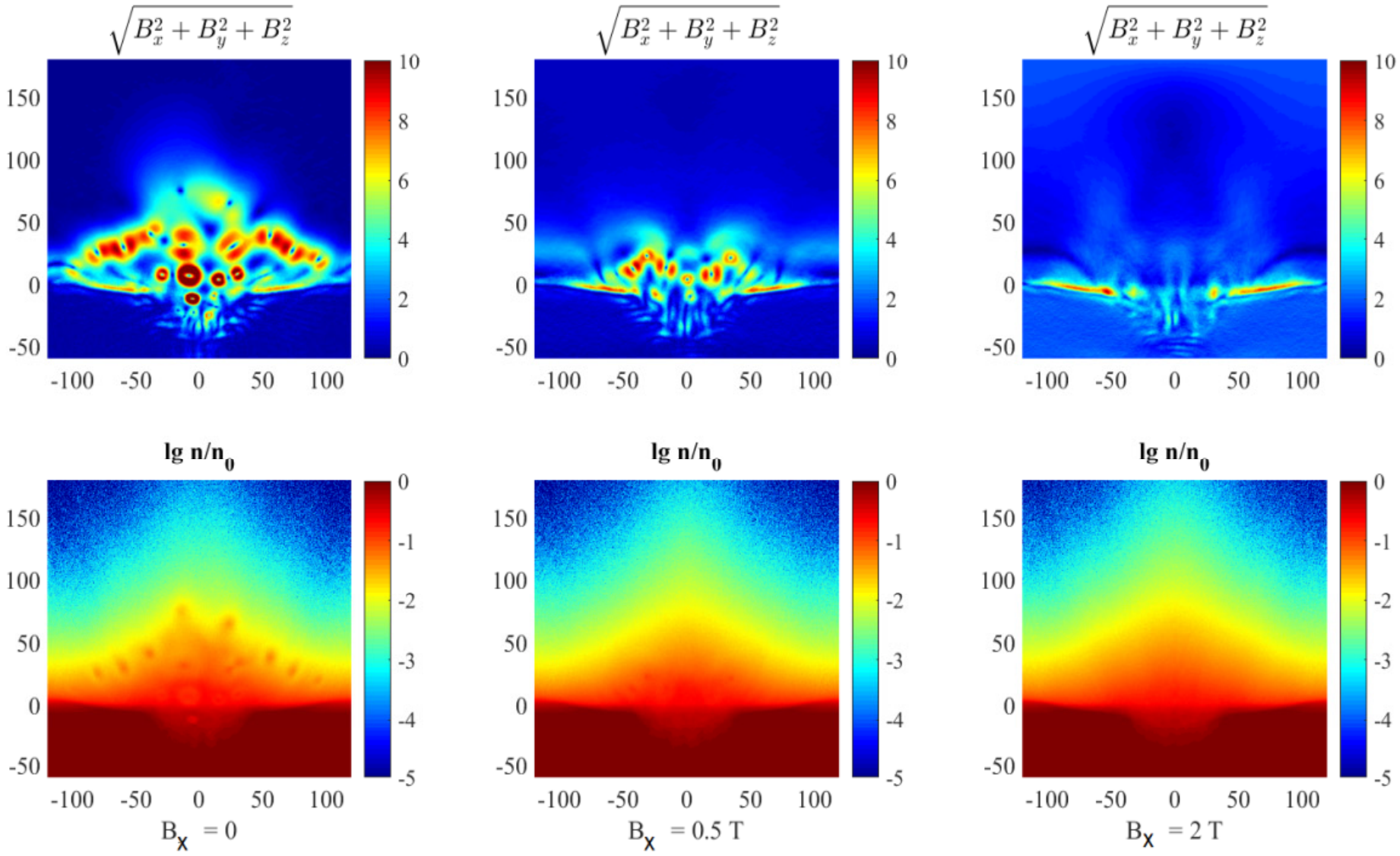

Comparison of expansion of a plasma with hot electrons (with initial concentration $n_0 = 10^{20}$ см$^{-3}$) at time $t = 36$ ps for simulations with different values of **external magnetic field, directed along x: B_x = 0, 0.5, 2 T** (from left to right). Upper panels show the magnitude of the magnetic field (in Tesla), lower panels show the logarithm of normalized plasma concentration.

Comparison of simulations of the expansion of a plasma with hot electrons in an **external magnetic field B_z = 13 T** for different ion masses. On the left, M = 100 m at time t = 25 ps, on the right, M = 400 m at time t = 50 ps. The initial plasma concentration is $n_0 = 10^{20}$ cm^{-3}. The horizontal and vertical axes correspond to the x and y coordinates respectfully (given in microns). The upper panels show the distribution of the quantity $(B_x^2+B_y^2)^{1/2}$, in the middle — the logarithm of the normalized plasma concentration n/n_0, the lower panels show the distribution of the effective temperature T_z (orthogonal to the calculation plane).

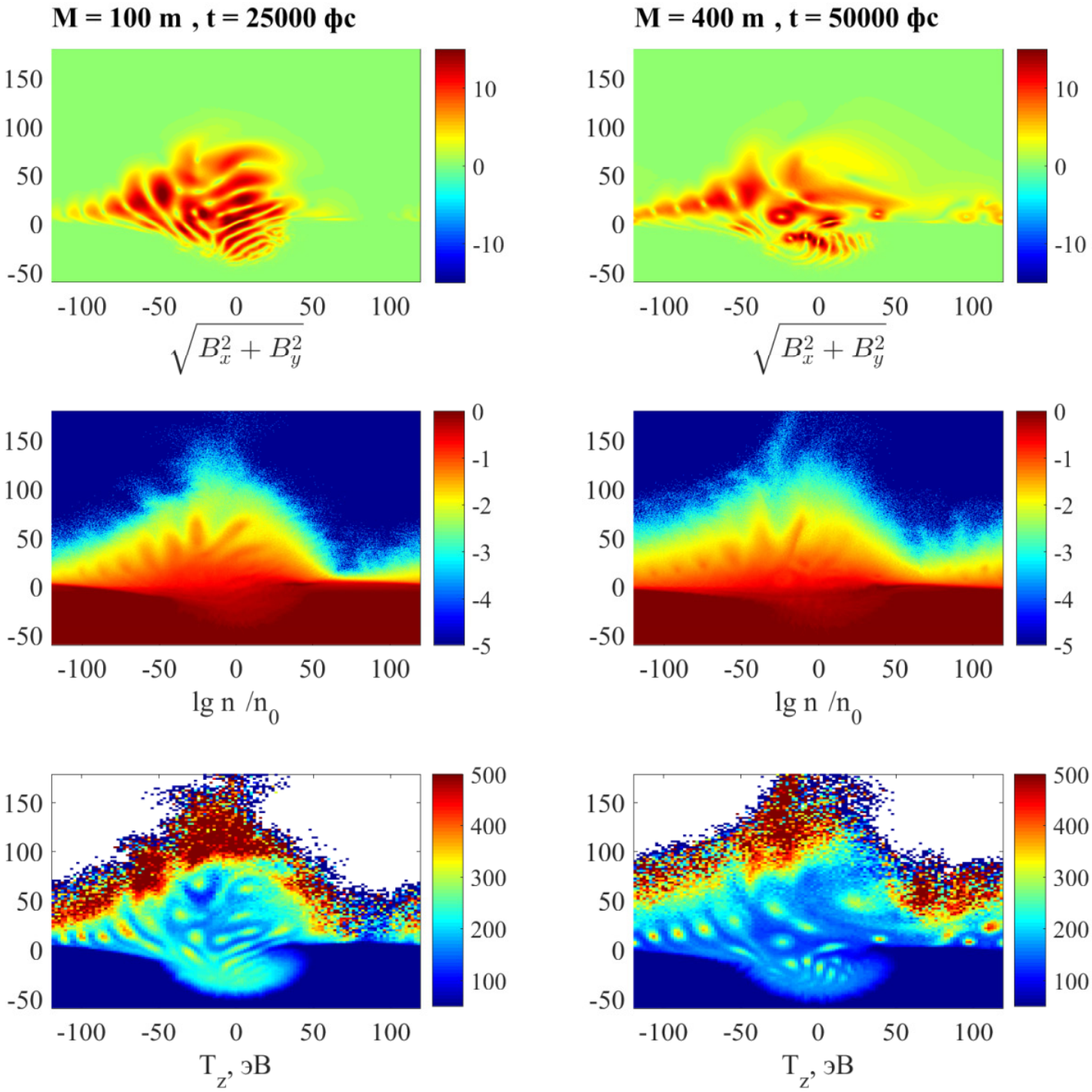

The magnetic structures after 7.5 ps expansion of a plasma layer with hot electrons into vacuum (the decay of the discontinuity). The **initial plasma concentration is $n_0 = 1.7 \cdot 10^{22}$ cm^{-3}**. The horizontal and vertical axes correspond to the x and y coordinates respectively (given in microns). On the left is the simulation with an external magnetic field B_z = 13 T orthogonal to the simulation plane: the top panel shows the B_z component of the magnetic field minus the external field (in Tesla) in color, the level lines show the plasma concentration normalized to the initial one, n/n_0, with gradations of 0.01, 0.1, 1; the bottom panel shows the B_x component of the field. Right panels show the same for the simulation with B_z = 250 T.

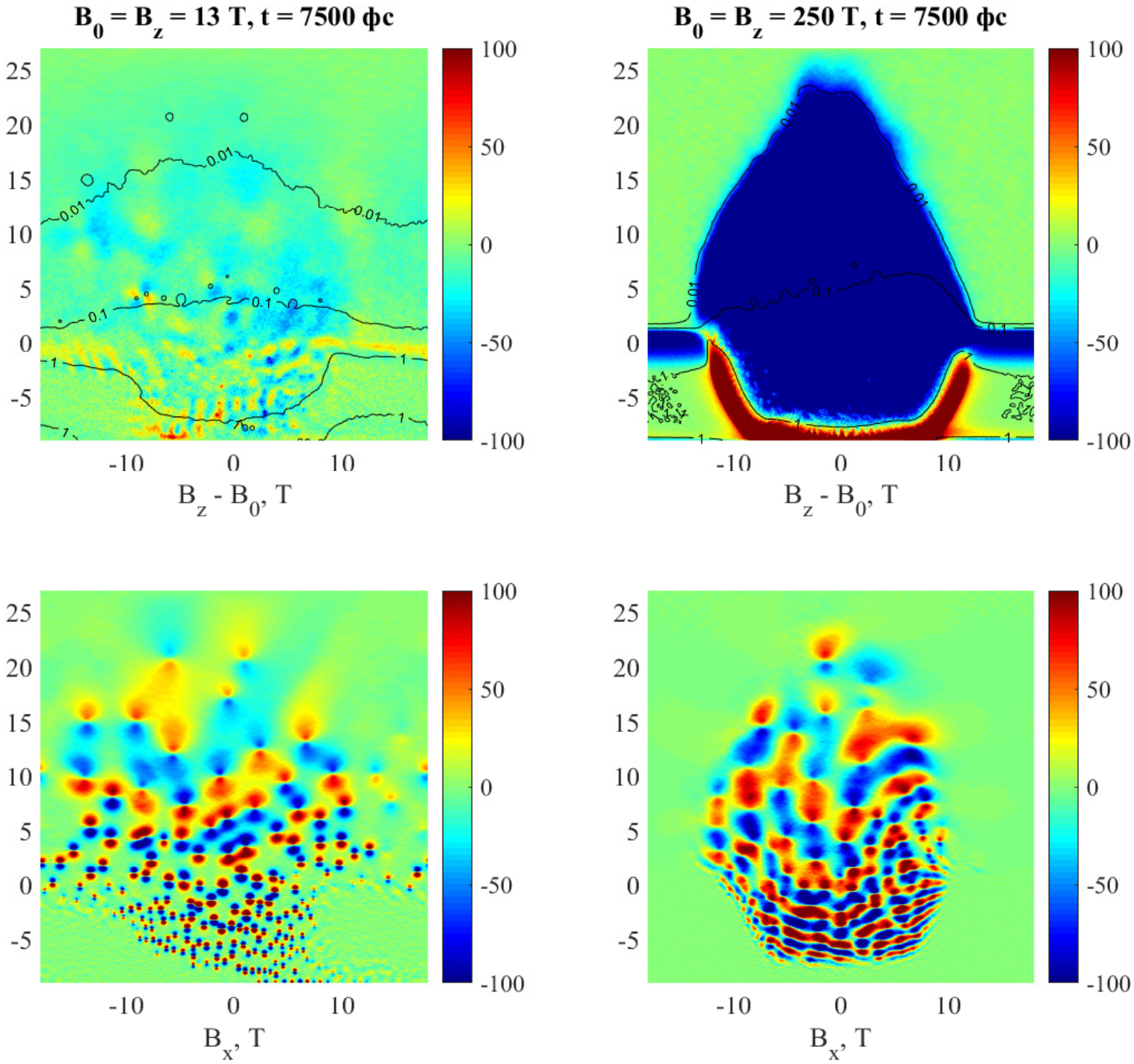

The magnetic structures after 7.5 ps expansion of a plasma layer with hot electrons into vacuum (the decay of the discontinuity). The initial plasma concentration is $n_0 = 1.7 \cdot 10^{22}$ cm^{-3}. The horizontal and vertical axes correspond to the x and y coordinates respectfully (given in microns). On the left is the simulation with an **external magnetic field B_x = 13 T** parallel to the simulation plane: the top panel shows the B_x component of the magnetic field minus the external field (in Tesla) in color, the level lines show the plasma concentration normalized to the initial one, n/n_0, with gradations of 0.01, 0.1, 1; the bottom panel shows the B_x component of the field. Right panels show the same for the simulation with **B_x = 250 T**.

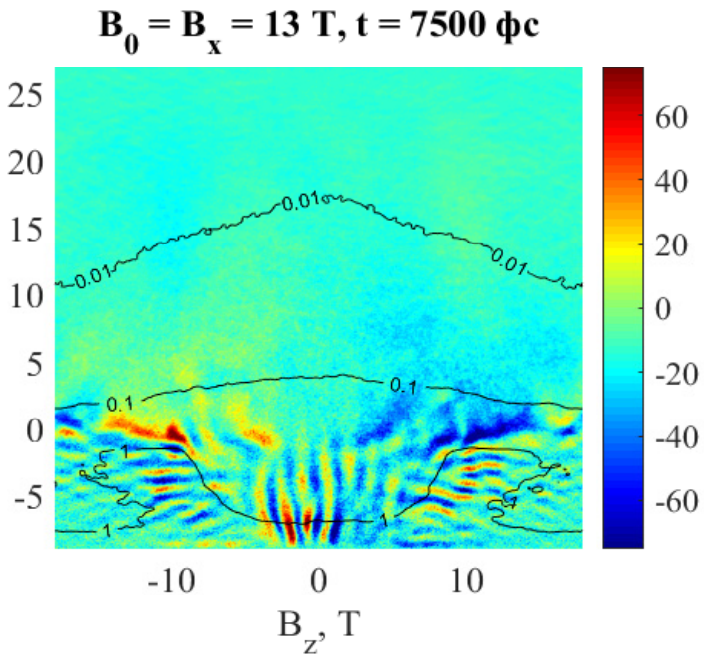

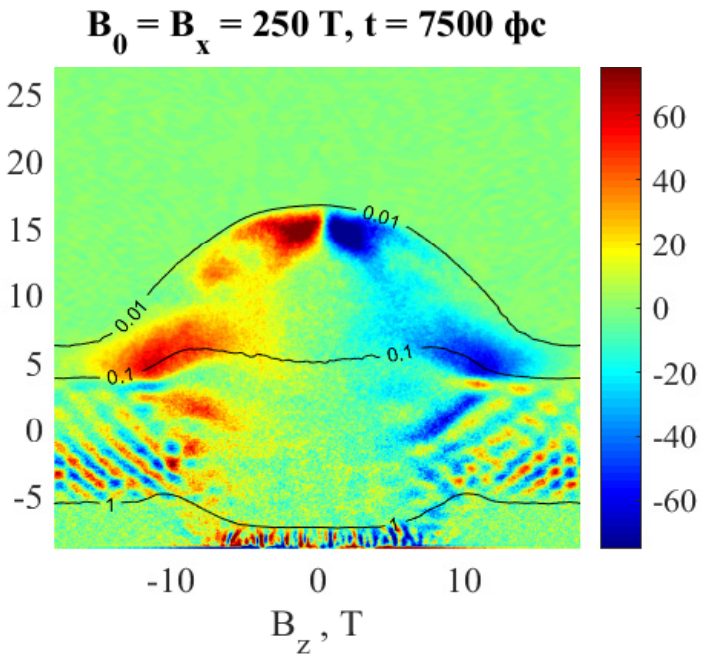

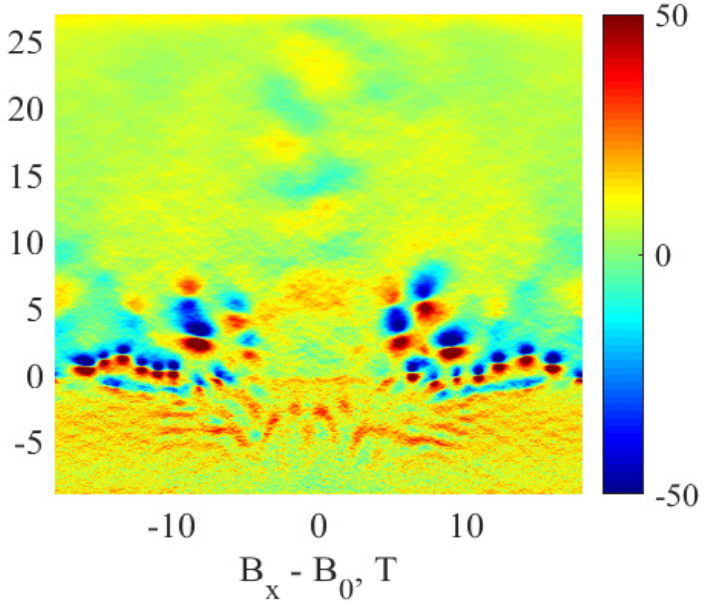

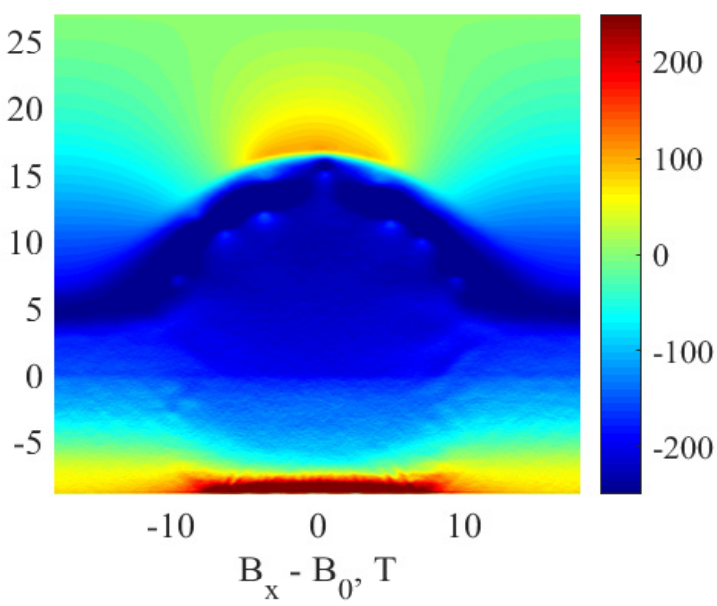

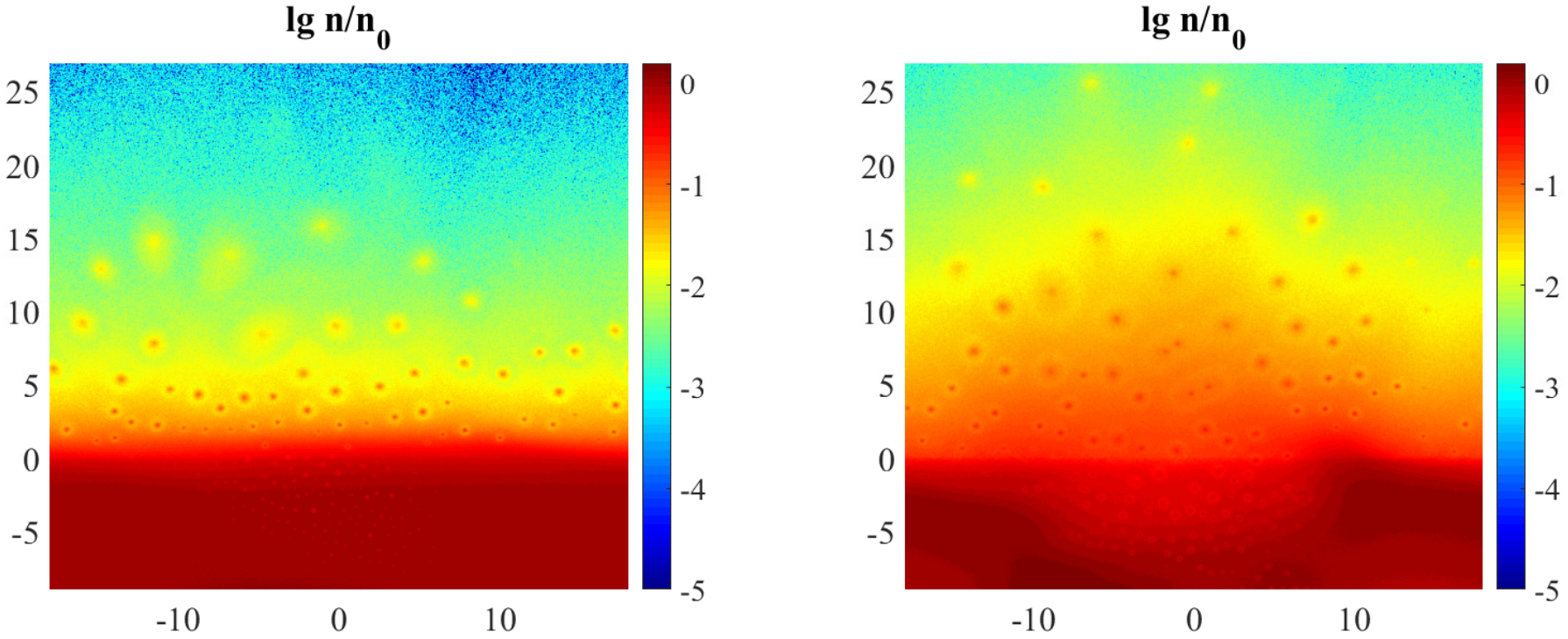

The logarithm of the normalized plasma concentration at time $t = 9$ ps for two simulations with the same external magnetic field $B_z = 13$ T and total initial plasma concentration of $1.7 \cdot 10^{22}$ cm^{-3}, but different fraction of heated electrons. On the left, **20% of electrons are heated**. On the right, **100% of electrons**.

Magnetic field components B_z minus the **external field B_z = 13 T** (top panels) and B_x (bottom) for two simulations with different fraction of heated electrons and the same total initial plasma concentration of $1.7 \cdot 10^{22}$ cm^{-3}, at time t = 5 ps. On the left, **20% of electrons are heated**. On the right, **100% of electrons**.

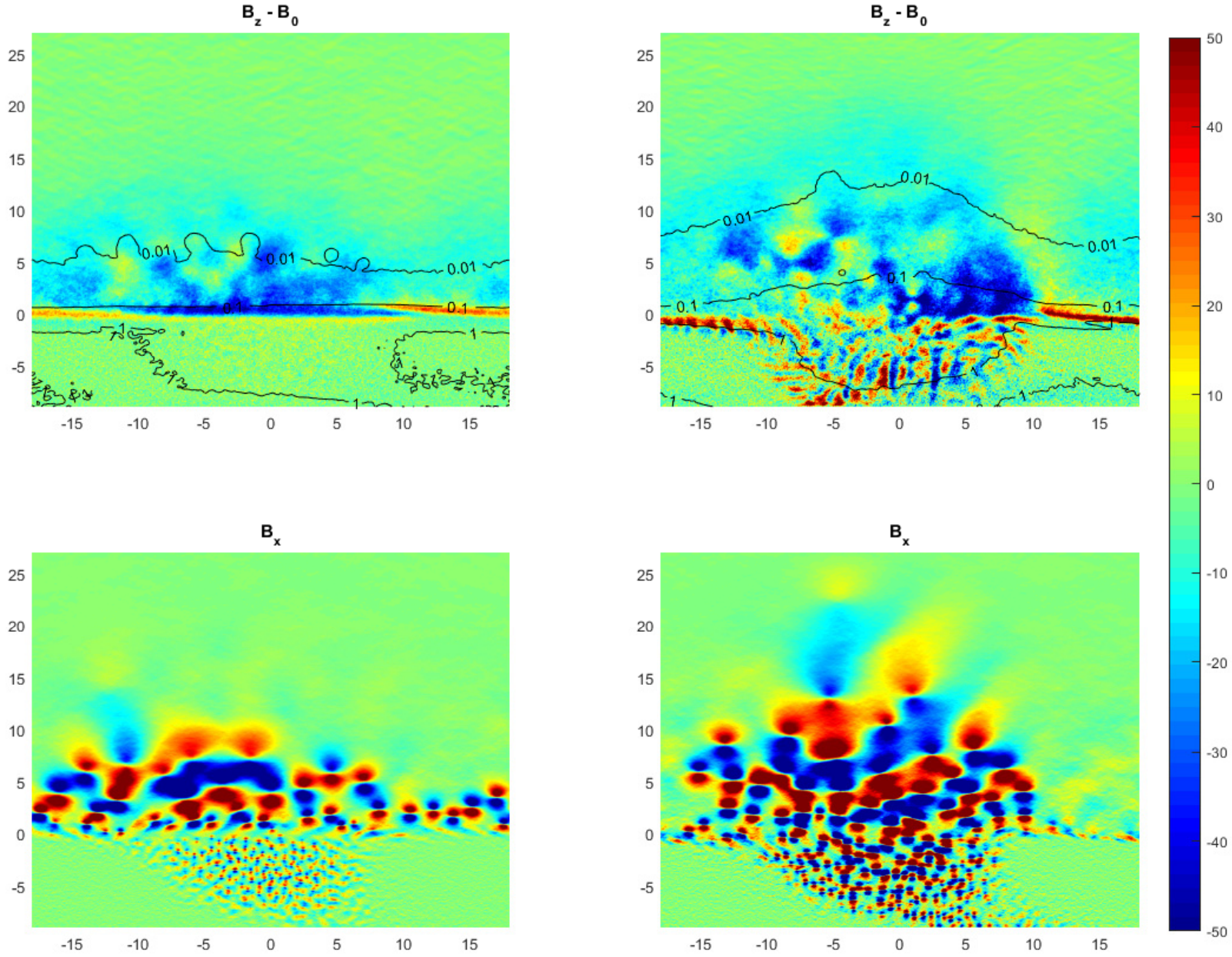

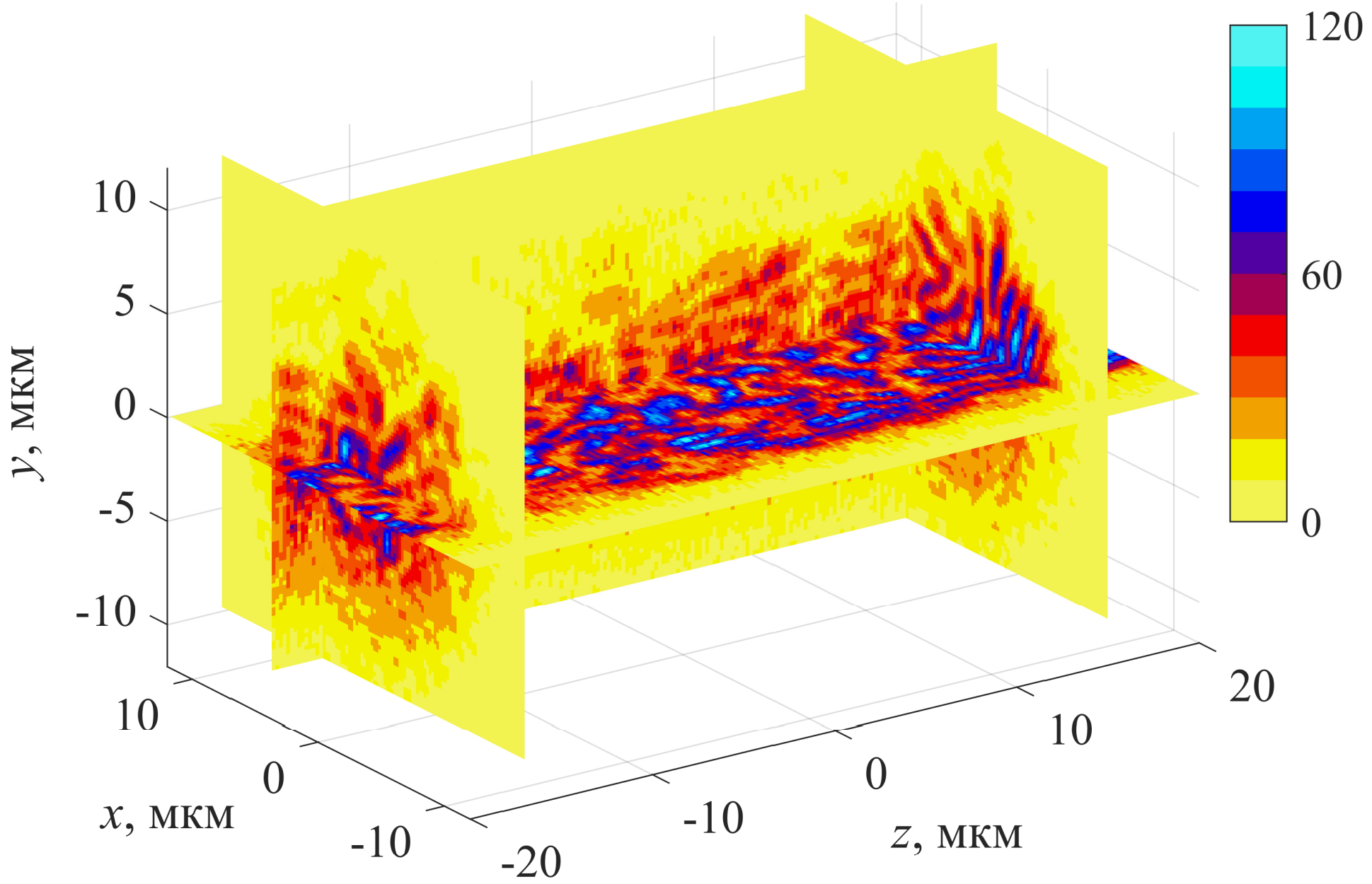

The magnitude of the transverse magnetic field $B_\perp = (B_x^2 + B_y^2)^{1/2}$ from the 3D PIC-simulation of the expansion of the plasma cloud with hot electrons into vacuum at the moment of time t = 3.0 ps. The initial plasma density is 1.7·10^22 cm^−3 . The external magnetic field is oriented along the z-axis, B0z = 250 T.

3D3V PIC-simulations, EPOCH code

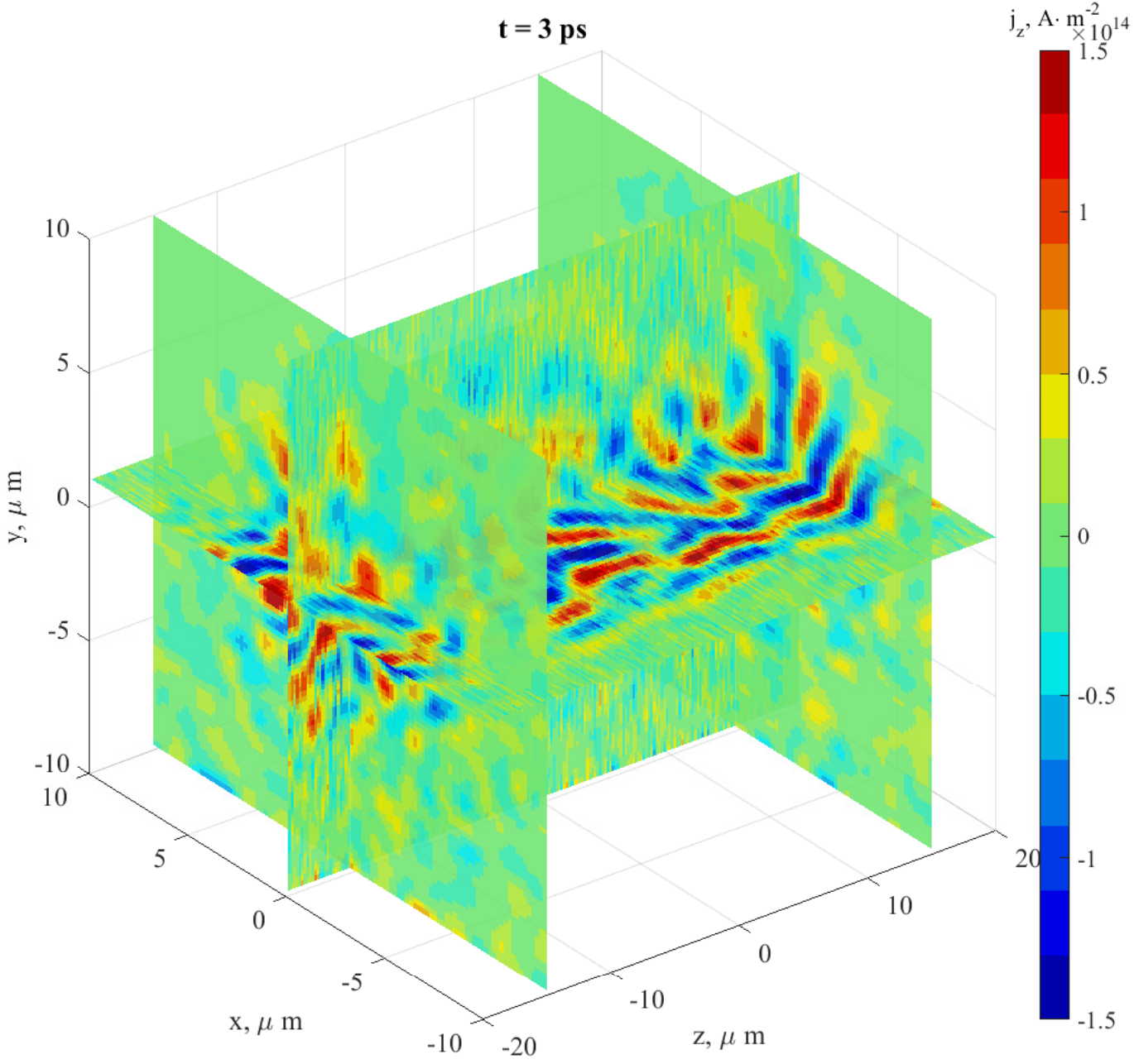

The neighbour current filaments have the opposite directions.

Z-component of the current density

Dieckmann M.E. et al. Expansion of a radially symmetric blast shell into a uniformly magnetized plasma // Phys. Plasmas 25 (2018) 052108

The expansion of a thermal pressure-driven radial blast shell into a dilute ambient plasma is examined with two-dimensional PIC simulations. The purpose is to determine if laminar shocks form in a collisionless plasma which resemble their magnetohydrodynamic counterparts. The ambient plasma is composed of electrons with the temperature of 2 keV and cool fully ionized nitrogen

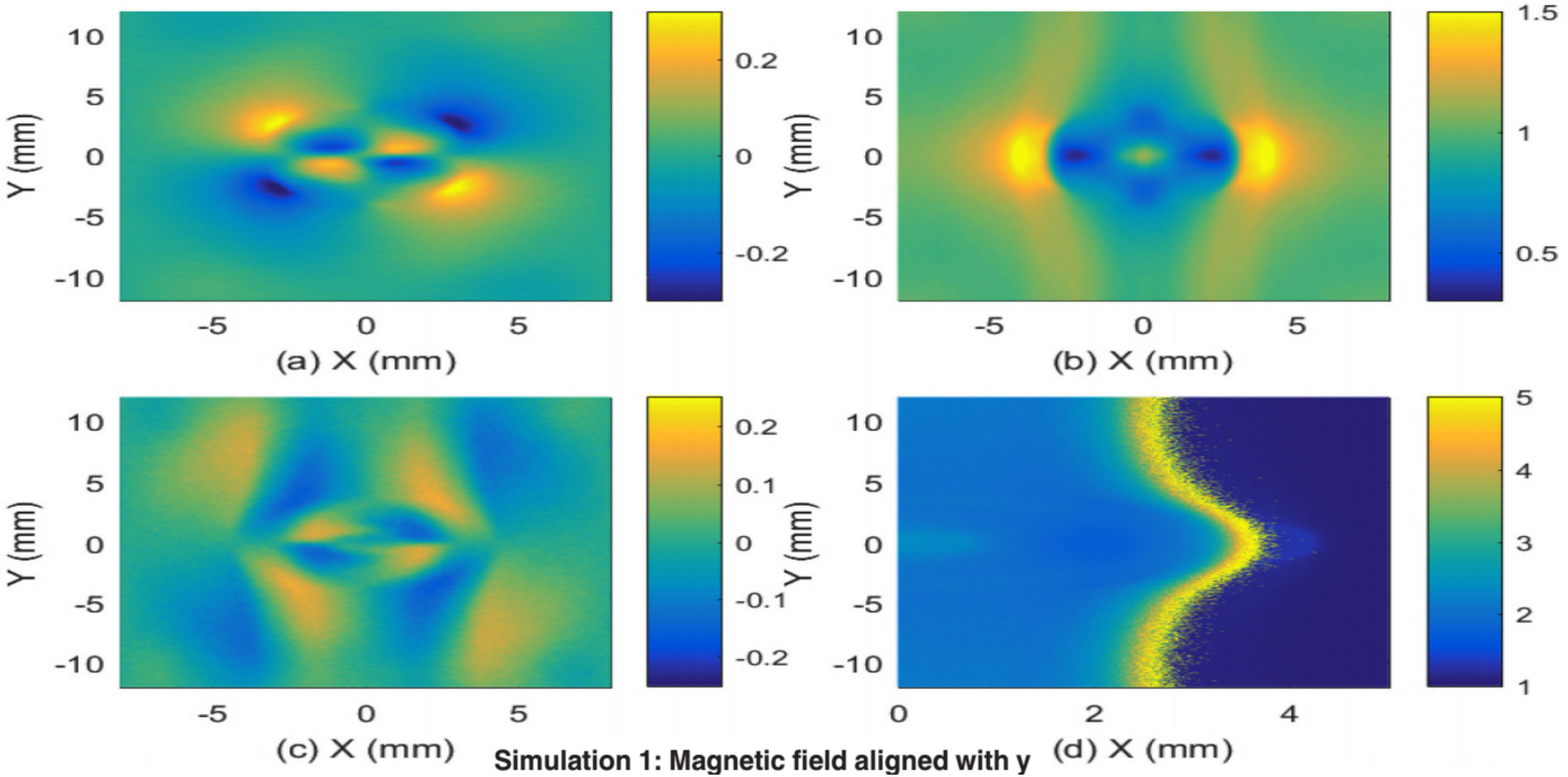

Simulation 1: Magnetic field aligned with y

The magnetic B_x component is shown in (a), B_y in (b), and B_z in (c) in units of B_0. (d) The mean kinetic energy per electron in units of th

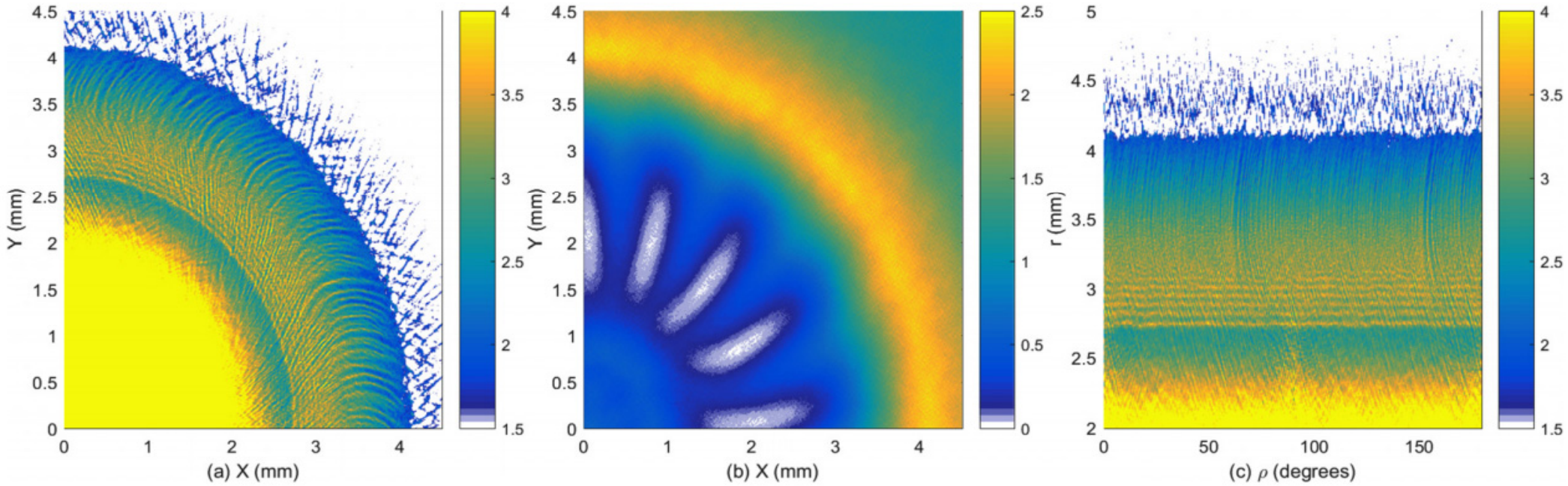

FIG. 7. The distribution of the ion density n_i and the normalized magnetic pressure $P_B = (B_x^2 + B_y^2 + B_z^2)/B_0^2$. The ion density is shown in Cartesian coordinates in (a). (b) The magnetic pressure in Cartesian coordinates. The ion density distribution in polar coordinates is shown in (c). The linear color scale i

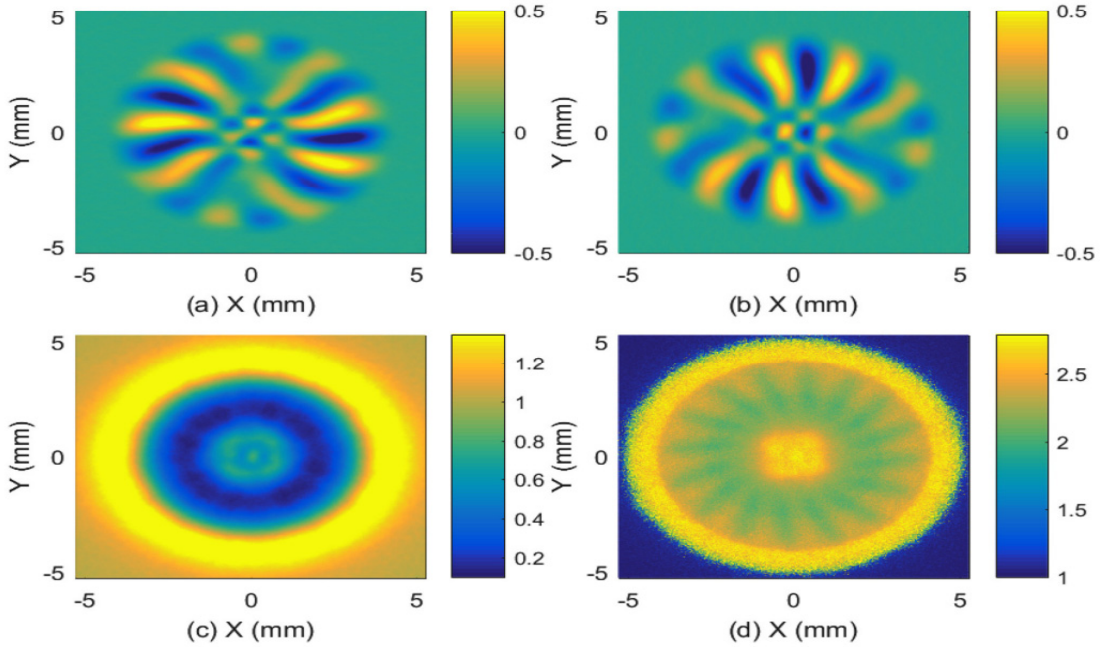

The magnetic B_x component is shown in (a), B_y in (b), and B_z in (c) in units of B_0. (d) The mean kinetic energy per electron in units of th

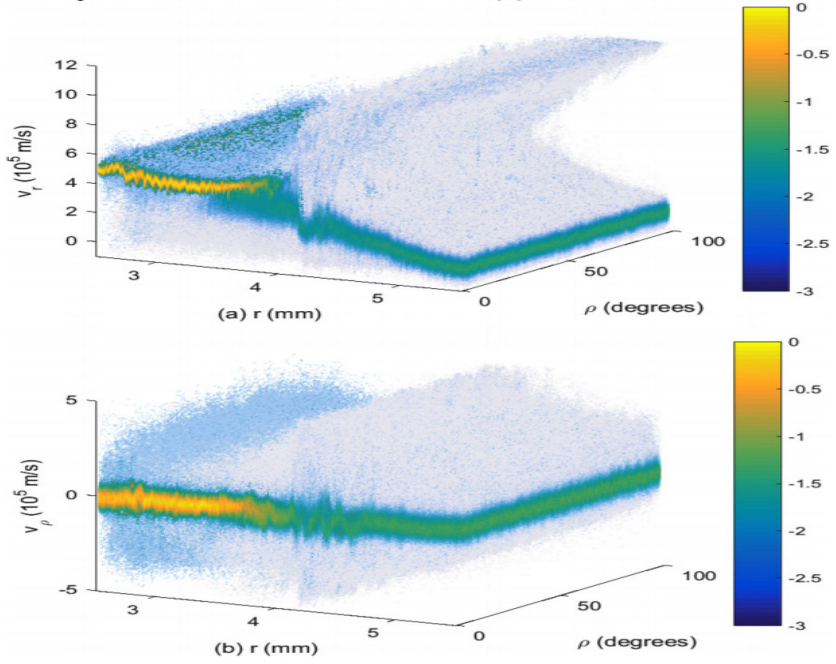

FIG. 8. The 10-logarithmic ion phase space density distribution in simulation 2. The time is $t_{sim} = 3.57$ ns. (a) The velocity in the radial direction v_r and (b) the azimuthal velocity component v_ρ.

Conclusions on the problem # 4

1. Even a weak magnetic field, the pressure of which is much less than the pressure of the expanding plasma cloud, significantly affects the cloud expansion in the presence of an energetic fraction of hot electrons and changes the structure of the arising quasi-magnetostatic field (turbulence).

2. **This expansion of the plasma is accompanied by a formation of the multiple local z-pinches, especially in the region with a displaced magnetic field.**

3. **The system of large-scale current sheets formed along the plasma boundary with a displaced magnetic field undergoes a small-scale transverse stratification which makes the boundary turbulent.**

4. A unidirectional external magnetic field leads to a violation of the symmetry of the expansion of the plasma and the arising current structures.

5. In the course of the surface heating of electrons by a short optical pulse, the character of expansion and the structure of currents in the resulting laser plasma can be very different from that in the case of the bulk heating.

5. Weibel-instability mechanism of a solar flare: analytical results for the growth rate and PIC-modeling of the nonlinear stage in the presence of an external magnetic field

Finally, let's discuss the Weibel instability and subsequent quasi-magnetostatic turbulence generated in a cold background plasma by a collisionless **flow of hot electrons moving along an external magnetic field**. Here, the orientation of the wave vectors of unstable modes is mainly across this field. Such situations with a one-directional flow or the counter-propagating flows of electrons are possible in the laser and cosmic plasmas. We have considered both an initial value problem and a boundary problem with the electron injection for various physical parameters of the system, including finite temperatures of all particle components. An experiment is underway.

On this basis, we propose **a novel mechanism of a solar flare associated with an individual coronal loop**. We show that a coronal loop can be heated, deformed and even destroyed in the course of Weibel instability due to an injection of energetic (multi-keV) electrons from a chromospheric plasma. For typical coronal parameters, we carry out the analytical theory and PIC-modeling of the instability in a collisionless plasma in the presence of an external magnetic field. If the latter is not too strong, a solar flare can be started up by a short-wavelength filamentation of currents along the external magnetic field (nanoflares) and a subsequent development of a quasi-magnetostatic turbulence.

The nanoflares are observed. An idea of the collective nanoflatres was introduced by E.Parker (1988) and L.Vlahos (1989), but its physical mechanism has not been found yet.

Related works on the Weibel (filamentation) instability in the presence of an external magnetic field

1. Hededal C.B., Nishikawa K.-I. *ApJ* 623 (2005) L89.
2. Stockem A. et al. *ApJ* 651 (2006) 584.
3. Pokhotelov O.A., Balikin M.A. *Ann. Geophys.* 30 (2012) 1051.
4. Bret A. *Phys. Plasmas* 21 (2014) 022106; 23 (2016) 062122.
5. Bret A., Dickmann M.E. *Phys. Plasmas* 24 (2017) 062105.
6. Grassi A et al. *Phys. Rev.* E 95 (2017) 023203.
7. Umega T., Nakamura K.M. *Phys. Plasmas* 25 (2018) 102109.
8. Verscharen D et al. *J. Plasma Physics* 84 (2018) 905840403.

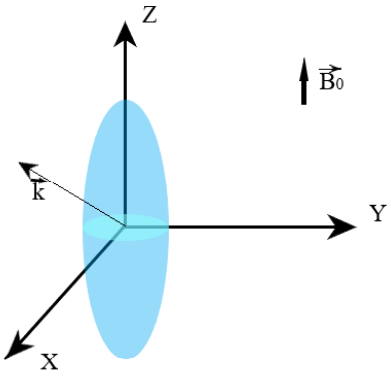

Fig. 1 Anisotropic bi-Maxwellian distribution function

The solar community is acquainted with many works on the injection of energetic electrons in the coronal loops and the subsequent deformation of the latter. See, e.g., Hudson et al. *MNRAS* 2020; Zaitsev V.V., Stepanov A.V. *Phys. Usp.* **51,** 1123, 2008; Zaitsev et al. *Sol. Phys.* 2015; Zaitsev, Stepanov *Solar Phys.* 292, 141, 2017; *Geom.&Aeron.* 59, 898, 2019 and references therein. For example, in some cases during the impulsive phase of the flare, the shrinkage of the size of the loops occurs and then the reduction is replaced by an increase in their size (Li & Gan, *ApJ* 629, L137, 2005; Zhou et al. *Res. A&A* 13, 526, 2013).

Linear analysis of the Maxwell-Vlasov equations in the presence of an external magnetic field

$$\frac{\partial f}{\partial t} + (\vec{v}\nabla)f + \frac{e}{m}\left\{\vec{E} + \frac{1}{c}[\vec{v}\times\vec{B} + \vec{B}_0]\right\}\frac{\partial f}{\partial \vec{v}} = 0 \qquad \vec{B} = \frac{c}{\omega}[\vec{k}\times\vec{E}]$$

$$f \approx f_0 + f_1 \qquad f_0 = \frac{n_0}{(2\pi)^{3/2}u_z u_\perp^2} e^{-\frac{v_0^2}{2u_\perp^2} - \frac{v_z{}^2}{2u_z^2}}$$

Initial condition

$$\frac{\partial f_1}{\partial t} + (\vec{v}\nabla)f_1 - \vec{\Omega}_c\left[\vec{v}\times\frac{\partial f_1}{\partial \vec{v}}\right] = -\frac{e}{m\omega}\left\{\left[\omega - \vec{k}\vec{v}\right]\vec{E}\frac{\partial f_0}{\partial \vec{v}} + \left(\vec{E}\vec{v}\right)\vec{k}\frac{\partial f_0}{\partial \vec{v}}\right\}$$

$$\vec{\Omega}_c = \frac{e\vec{B}_0}{mc}$$

Ordinary mode equation $k^2 - \frac{\omega^2}{c^2}\varepsilon_{zz} = 0$

Here f_0 is an initial distribution function, u_z average velocity in the Z-direction, $u_\perp$ average velocity in the transverse direction, m electron mass, e electron charge, c velocity of light in a vacuum, Ω_c electron gyro-frequency, $\vec{k}$ wave vector, ε_{zz} dielectric tensor component. In what follows, the axis of the highest temperature matches the direction of the external magnetic field B_0 along Z-axis.

Solution to the dispersion equation

$$\omega^2 - \omega_p^2\left(1 - \frac{u_z^2}{u_\perp^2} + \frac{u_z^2}{u_\perp^2}\sum_{n=-\infty}^{+\infty}\frac{\omega^2}{\omega^2 - n^2{\Omega_c}^2}e^{-S^2}I_n(S^2)\right) = {k_\perp}^2c^2$$

$$\sum_{n=-\infty}^{+\infty}\frac{\omega^2}{\omega^2 - n^2{\Omega_c}^2}e^{-S^2}I_n(S^2) = F\left(\frac{1}{2}, 1; 1 + \frac{\omega}{\Omega_c}, 1 - \frac{\omega}{\Omega_c}; -2S^2\right)$$

Generalized hypergeometric function

$$|\omega| \gg |k_\perp u_\perp| \qquad S = \frac{k_\perp u_\perp}{\Omega_c} \qquad |\omega| \ll |k_\perp u_\perp|$$

$$F \approx 1 + \frac{k_\perp^2 u_\perp^2}{\omega^2 - \Omega_c^2} \qquad I_n(S^2) \approx \frac{e^{S^2}}{\sqrt{2\pi}S}$$

$$\Gamma = \frac{1}{\sqrt{2}}\left[\sqrt{\left(k_\perp^2c^2 + \omega_p^2 + \Omega_c^2\right)^2 + 4\Omega_c^2\left(\omega_p^2\frac{u_z^2}{u_\perp^2}\frac{(k_\perp u_\perp)^2}{\Omega_c^2} - k_\perp^2c^2 - \omega_p^2\right)} - \left(k_\perp^2c^2 + \omega_p^2 + \Omega_c^2\right)\right]^{\frac{1}{2}}$$

$$\sum_{n=-\infty}^{+\infty}\frac{\omega^2}{\omega^2 - n^2{\Omega_c}^2}e^{-S^2}I_n(S^2) \approx \frac{\Omega_c}{\sqrt{2\pi}k_\perp u_\perp}\sum_{n=-\infty}^{+\infty}\frac{\Gamma^2}{\Gamma^2 + n^2{\Omega_c}^2} = \sqrt{\frac{\pi}{2}}\frac{\Gamma}{k_\perp u_\perp}cth\left(\frac{\pi\Gamma}{\Omega_c}\right)$$

$$\Gamma^2 + \omega_p^2\left(1 - \frac{u_z^2}{u_\perp^2} + \frac{u_z^2}{u_\perp^2}\sqrt{\frac{\pi}{2}}\frac{\Gamma}{k_\perp u_\perp}cth\left(\frac{\pi\Gamma}{\Omega_c}\right)\right) + {k_\perp}^2c^2 = 0$$

Growth rate and saturating magnetic field

$$\Gamma^2 + \omega_p^2\left(1 - \frac{u_z^2}{u_\perp^2} + \frac{u_z^2}{u_\perp^2}\sqrt{\frac{\pi}{2}}\frac{\Gamma}{k_\perp u_\perp} cth\left(\frac{\pi\Gamma}{\Omega_c}\right)\right) + {k_\perp}^2 c^2 = 0$$

Extremum equation

$$k_{\perp max}^6 + 3\frac{\pi}{8}(A+1)^2\frac{c^2}{u_\perp^2}\frac{\omega_p^4}{c^4}k_{\perp max}^2 - \frac{\pi}{8}A(A+1)^2\frac{c^2}{u_\perp^2}\frac{\omega_p^6}{c^6} = 0 \qquad k_{\perp max} \approx \omega_p \approx \sqrt{N_e}$$

$$cth\left(\frac{\pi\Gamma}{\Omega_c}\right) \approx \frac{1}{\frac{\pi\Gamma}{\Omega_c}} + \frac{\pi\Gamma}{3\Omega_c} - \frac{1}{45}\left(\frac{\pi\Gamma}{\Omega_c}\right)^3 + \cdots$$

$$\Gamma = \left[\frac{\omega_p^2\left(A - \frac{1}{\sqrt{2\pi}}\frac{u_z^2}{u_\perp^2}\frac{\Omega_c}{k_\perp u_\perp}\right) - {k_\perp}^2 c^2}{1 + \sqrt{\frac{\pi^3}{18}}\frac{u_z^2}{u_\perp^2}\frac{\omega_p^2}{k_\perp u_\perp \Omega_c}}\right]^{1/2}$$

$$B_{ext}^* = \sqrt{2\pi}\frac{mc}{e}k_\perp u_\perp\left(1 - \frac{u_\perp^2}{u_z^2}\left(1 + \frac{k_\perp^2 c^2}{\omega_p^2}\right)\right) \qquad B_{ext}^* \approx \omega_p \approx \sqrt{N_e}$$

The saturation condition: the gyro-frequency is equal to the growth rate. → $B_{sat} \sim (1/2)\, B_{ext}^*$

A harmonic with maximum growth rate and a critical magnetic field

Numerical solution to the growth-rate equation gives for $u_\perp$=0.06c

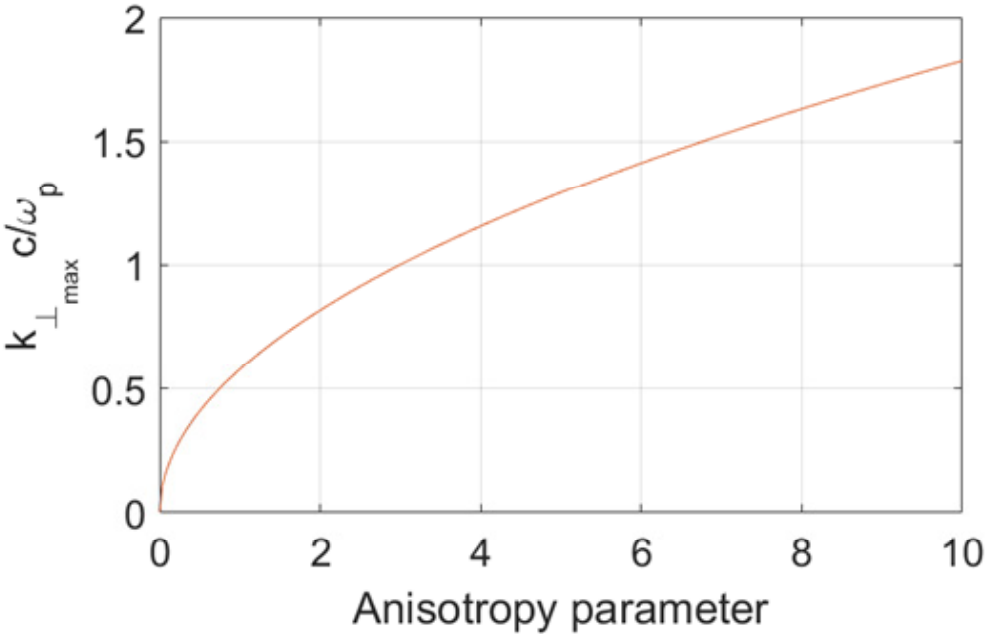

Fig. 1 Anisotropy dependence of a wavenumber of the utmost unstable harmonic

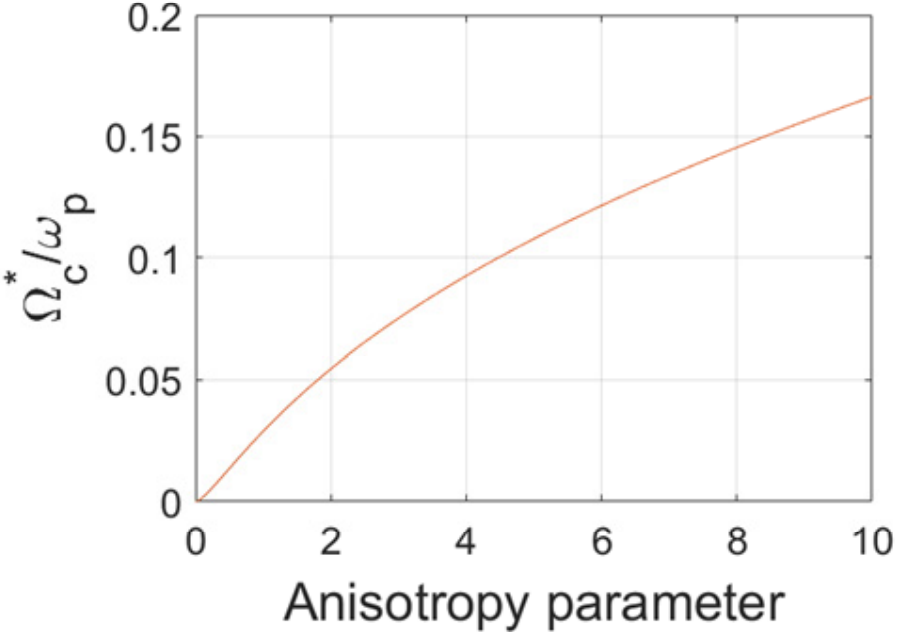

Fig. 2 Anisotropy dependence of the critical external magnetic field

For details see the talk of Emelyanov at seminar 3 (Nov. 9), hall 1.

Approximate results in the hydrodynamic and kinetic regimes of the Weibel instability

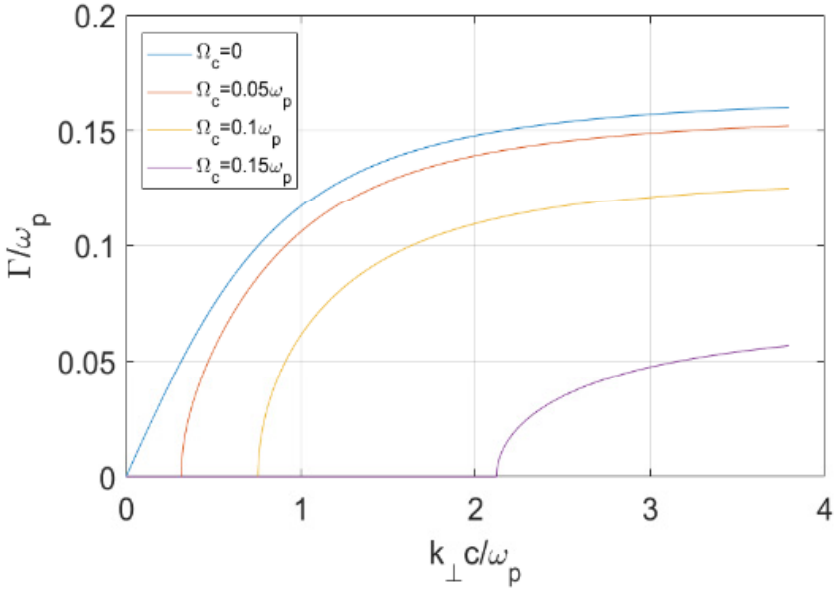

Fig. 3 Hydrodynamic regime $|\Gamma| >> |k_\perp u_\perp|$

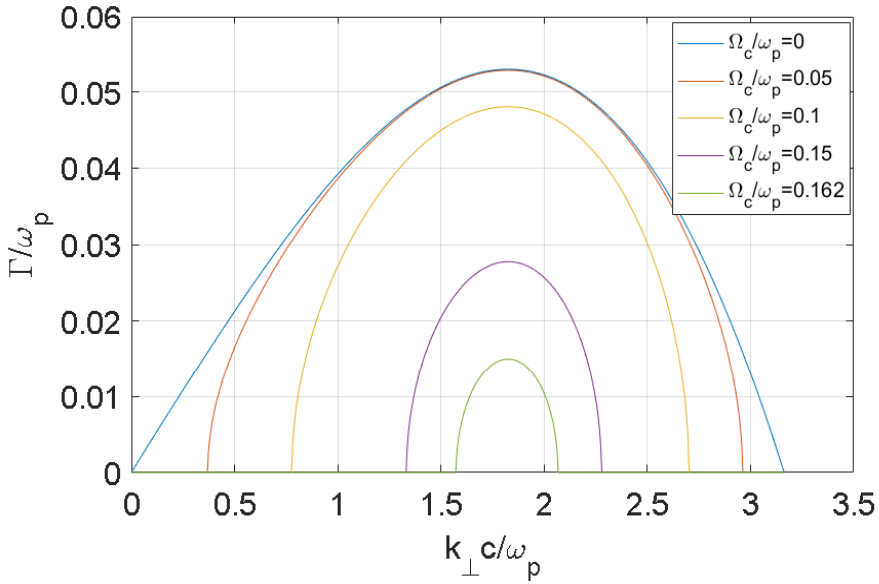

Fig. 4 Kinetic regime $|\Gamma| << |k_\perp u_\perp|$

The dependence of the growth rate on a wavenumber for the anisotropy parameter $A=(\frac{u_z^2}{u_\perp^2}-1)=10$, $u_\perp = 0.06c$ and different values of the external magnetic field. A growth rate of the Weibel instability is found from the linearized Maxwell-Vlasov equations with the initial bi-Maxwellian particle distribution for the case of a strictly transverse wave propagation, $\mathbf{k} \perp \mathbf{B_0}$, demonstrating the highest growth rate.

Typical (optimistic) estimates for a plasma of the coronal arches

A collisionless electron-ion plasma with typical density $N_{bkg} \sim 10^{10}$ - 10^{12} cm^{-3}

and a smooth inhomogeneity scale L ~ 100 – 1000 km.

The background electrons and ions are quite cold: $T_i \sim T_{e,bkg} \sim$ 10 eV - 1 keV.

The injected hot electrons with a temperature $T_e \sim$ 1 - 30 keV may be highly anisotropic,

$A=T_l / T_t - 1 \geq 1$, and have a high density up to the value $N \sim 0.1 N_{bkg} \sim 10^{11}$ cm^{-3}.

An injection time period is of the order of several seconds, i.e., much greater than

an inverse growth rate of the Weibel instability which exceeds the value $\omega_p^{-1} c / u_t$.

An electron velocity anisotropy A ~ 1 corresponds to velocities $u_l^2 \sim 2u_t^2 \sim 10^{-2} c$.

A saturation magnetic field: $\omega_B \sim \omega_p u_t / c \Rightarrow B_s^2 / 8\pi \sim N m u_t^2 / 2 \Rightarrow B_s \sim 100G$.

An optimal Weibel wavenumber is of the order or less than $k_W = 2\pi / R_{filament} \sim \omega_p / c$.

The quasi-magnetostatic Weibel turbulance can have a scale of the order of 1 m – 1 km

and the energy density comparable to the energy density of the coronal magnetic field.

See, e.g., Zaitsev V.V., Stepanov A.V. Coronal magnetic loops, *Phys. Usp.* **51,** 1123 (2008); Zaitsev V.V., Stepanov A.V. *Solar Phys.* **292**, 141 (2017) and references therein.

Schematic representation of the coronal loops (according to SOHO, TRACE, SMM data)

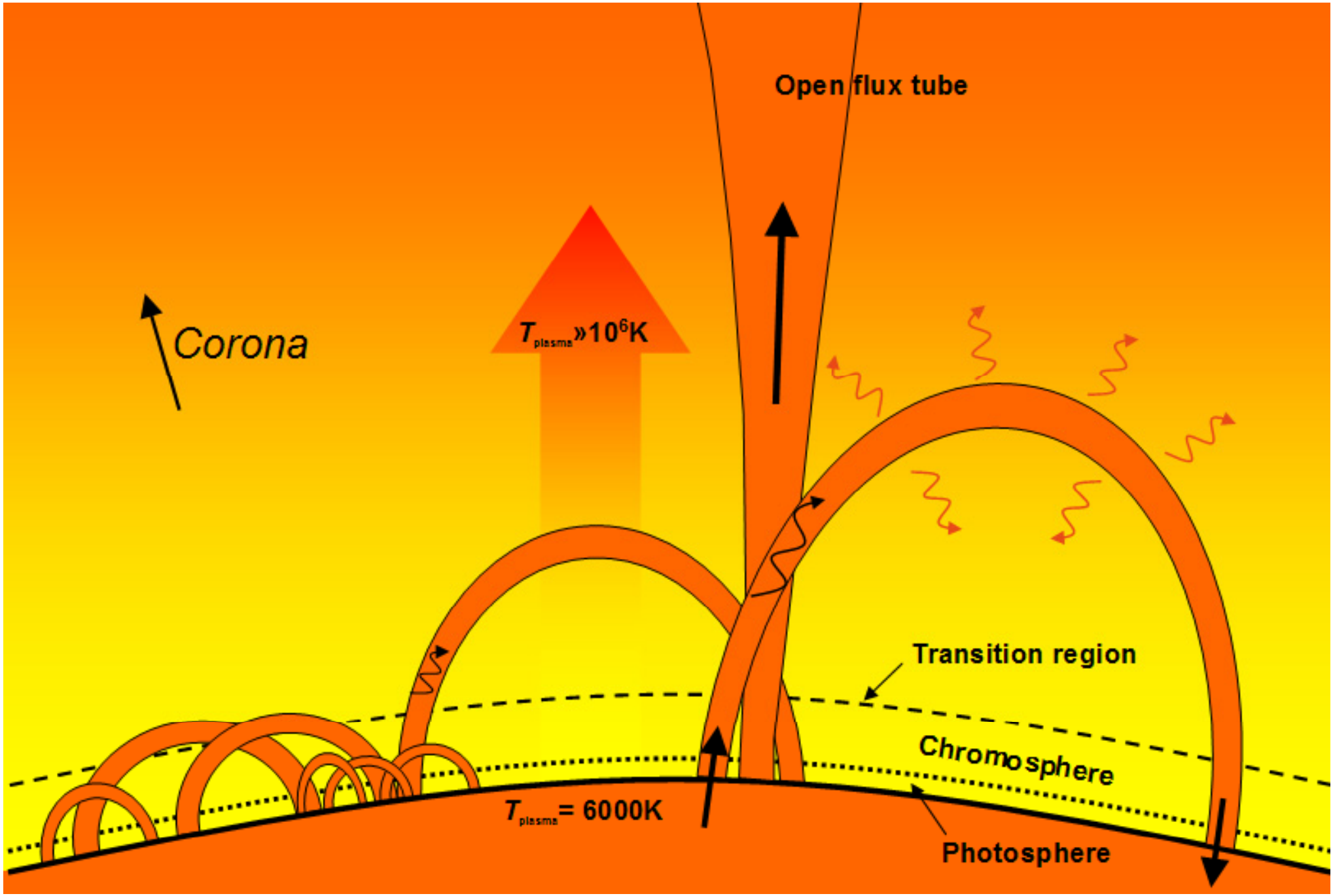

Energy emitted is from 10^{20} to 10^{25} joules.

From Wikipedia

Numerical modeling of the formation and nonlinear evolution of the Weibel quasi-magnetostatic turbulence

Numerical 2D3V PIC-modeling of the Weibel-type instability is demonstrated below for the case of two counterstreaming beams in a cold background plasma placed in the external magnetic field

(i) parallel to Y axis of the plane of the calculation XY (XY-geometry) and
(ii) orthogonal to this plane (Z-geometry).

The temperature of the background plasma is either 50 eV or 1 keV, the electron energy in the beams is approximately 10 keV (an efficient temperature is 1 keV).

A density of each beam is $10^{11}\ cm^{-3}$, a density of the background plasma is either ten times higher or equal to the total beam density.

The results are shown for several values of the external magnetic field, including 50 G and 100 G.

In the initial value problem, the periodic boundary conditions are used along both X and Y axes.

Injection of the counter-propagating beams along a vertical axis Y (a boundary problem)

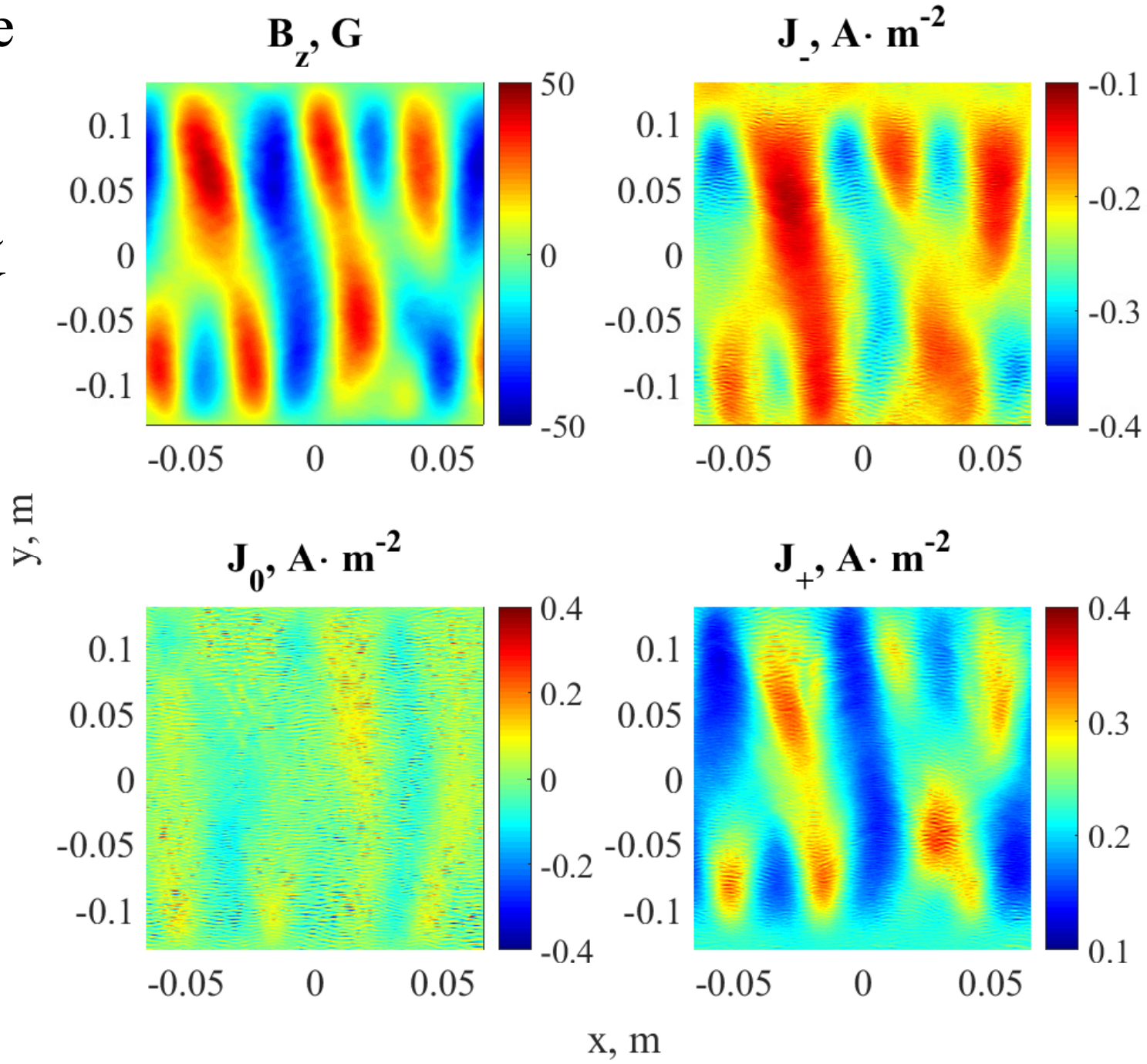

3D modeling of the streaming instability in a background plasma

Parameters of the 3D PIC simulation by EPOCH code are the following:

$n_b = 10^{11}\ cm^{-3}$, $n_0 = 2 \cdot 10^{11}\ cm^{-3}$, $B_{Y0} = 50$ G, $T_e = 1$ keV for all sorts of electrons, the electron energy in the beams is approximately 10 keV. The plots are given for the moment of time $180\omega_p^{-1}$

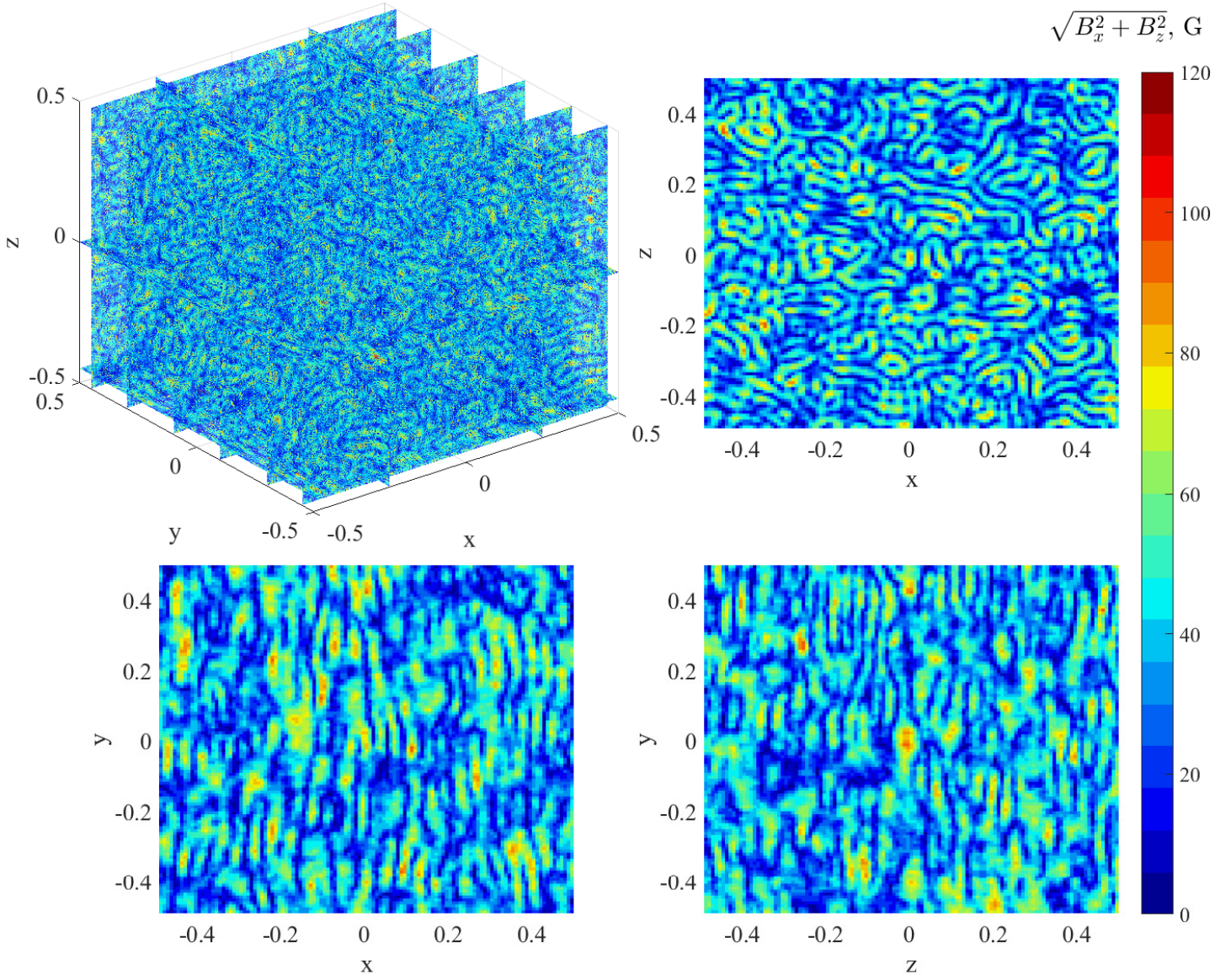

2D modeling in XY-geometry. 1keV beam

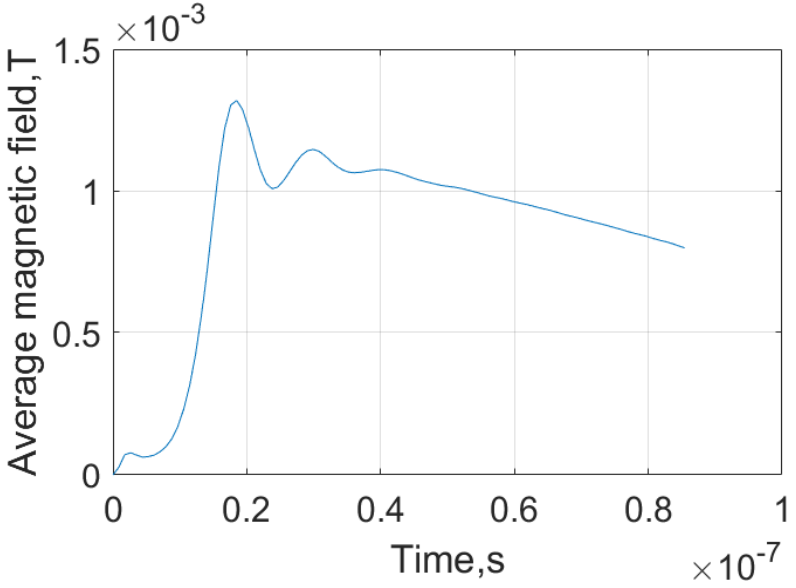

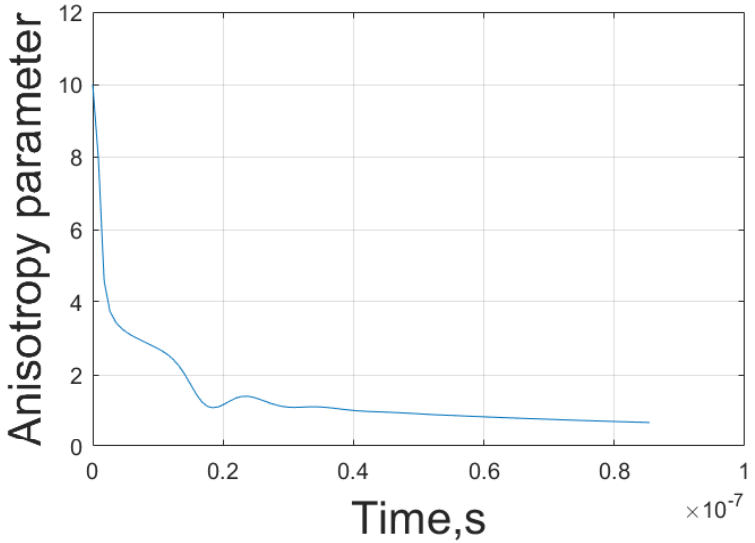

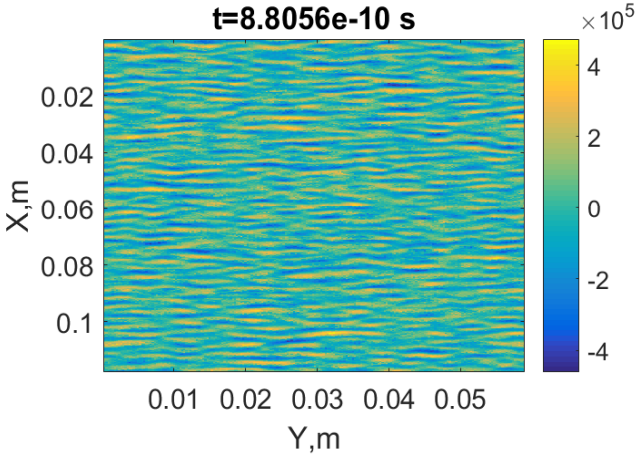

Fig.1 Current density component Jx at the moment of time 0.9 ns without external field

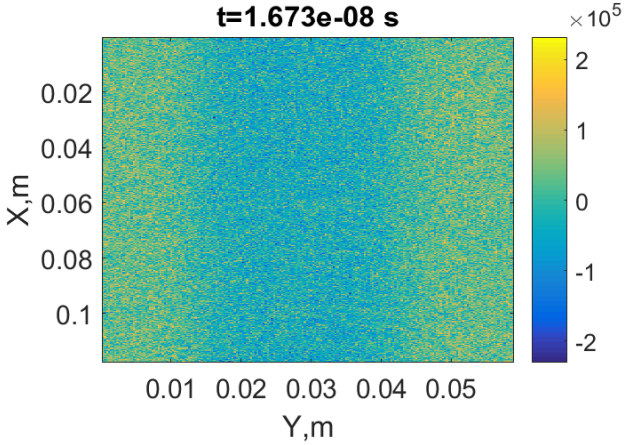

Fig.2 Current density component Jx at the moment of time 16.7 ns without external field

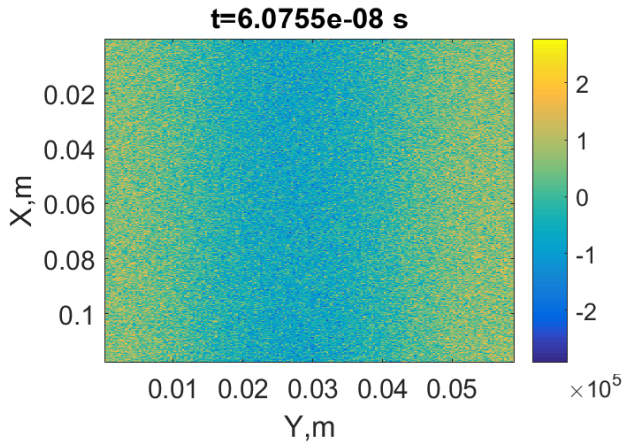

Fig.3 Current density component Jx at the moment of time 60.8 ns without external field

Density of various particles. XY-geometry. 1keV beam

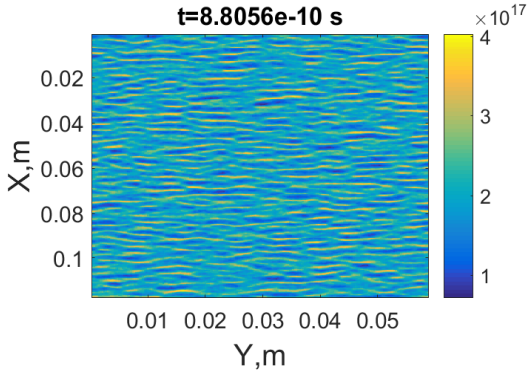

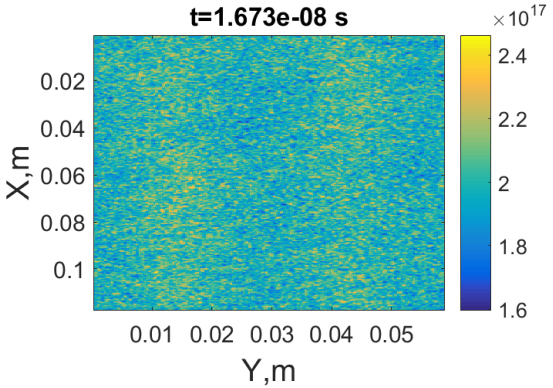

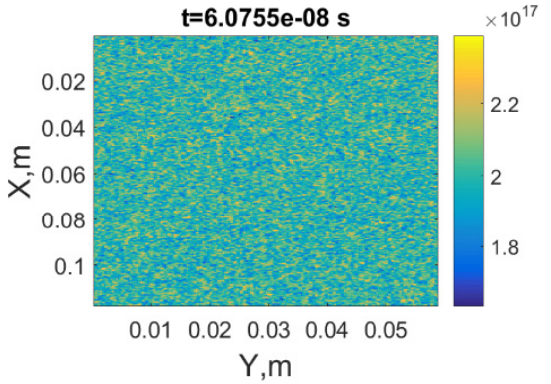

Back-ground electrons

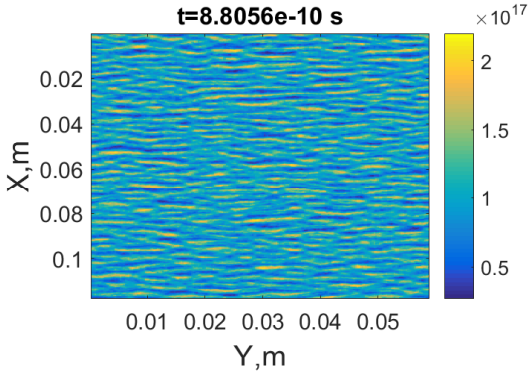

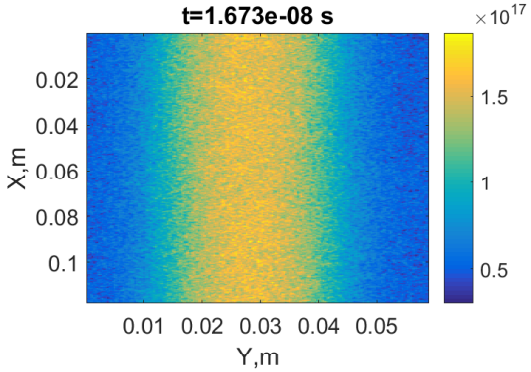

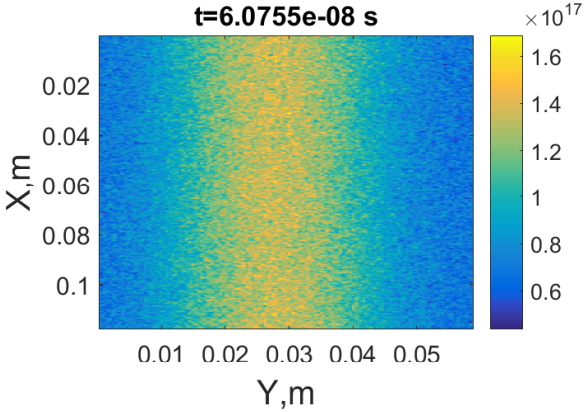

Beam electrons

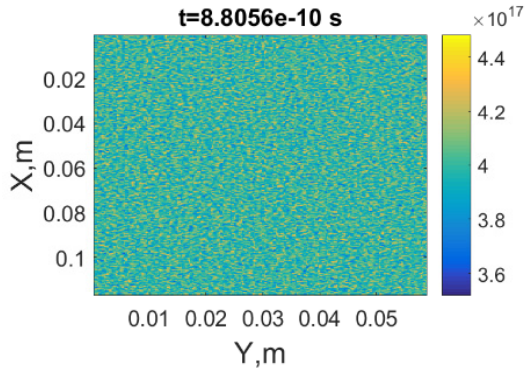

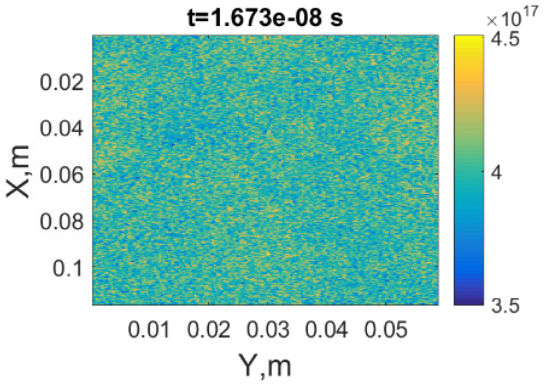

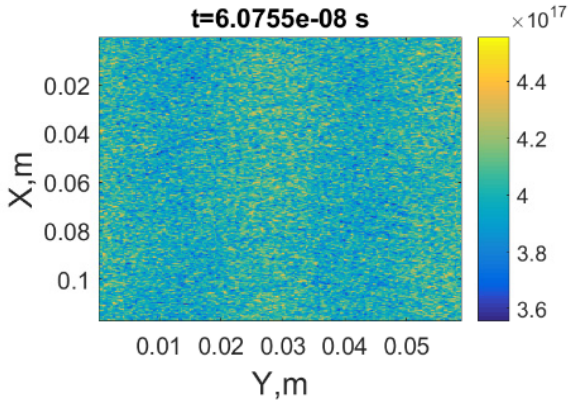

Total ions

Density of various particles in XY-geometry. 10keV beam

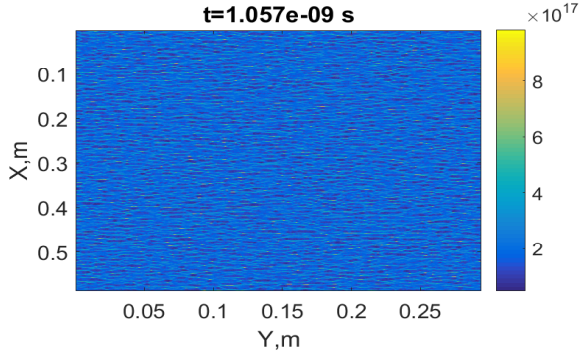

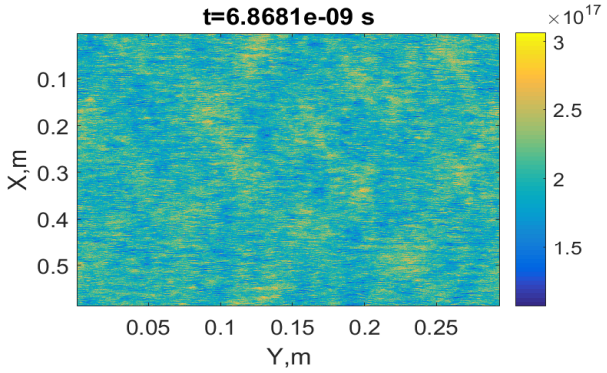

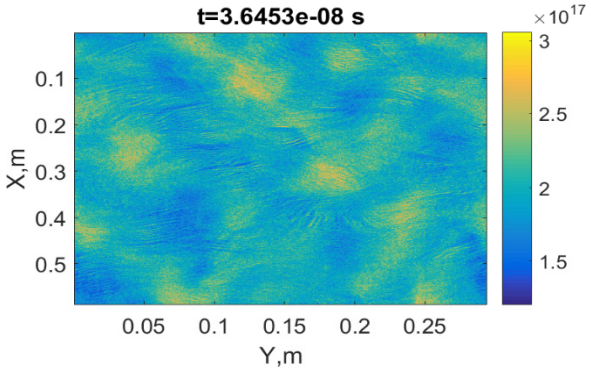

Back-ground elect-rons

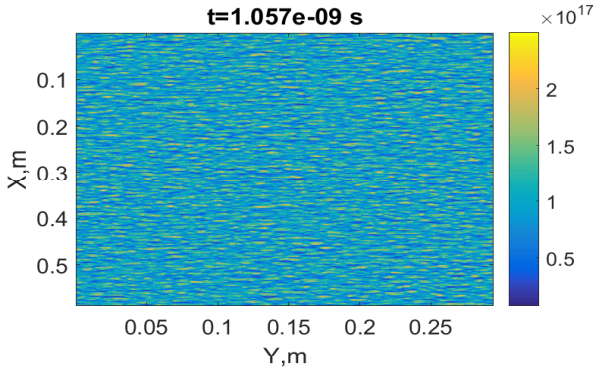

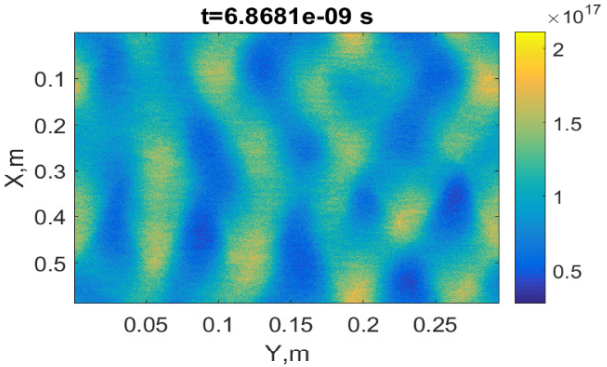

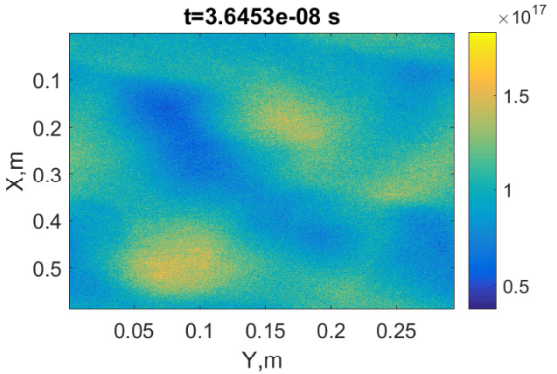

Beam electrons

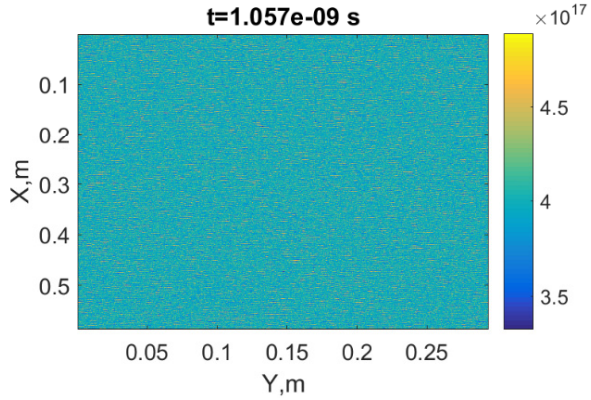

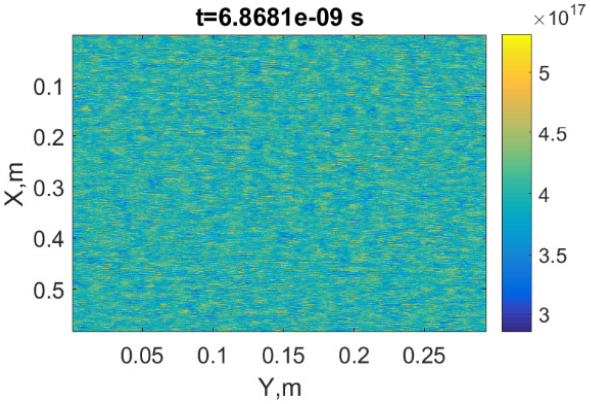

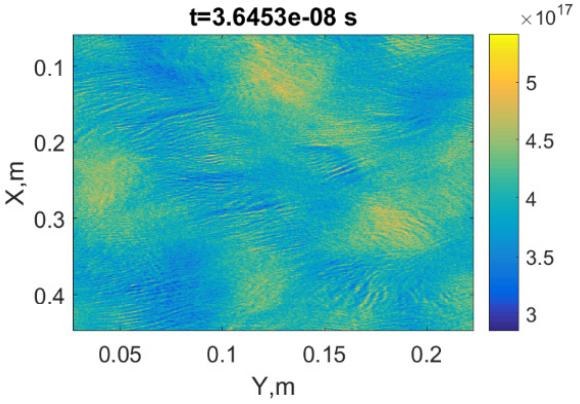

Total ions

Density of various particles. Z-geometry. 10keV beam

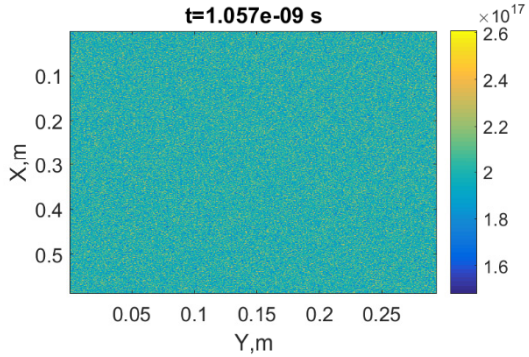

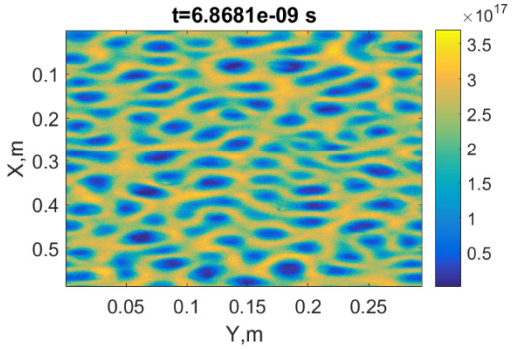

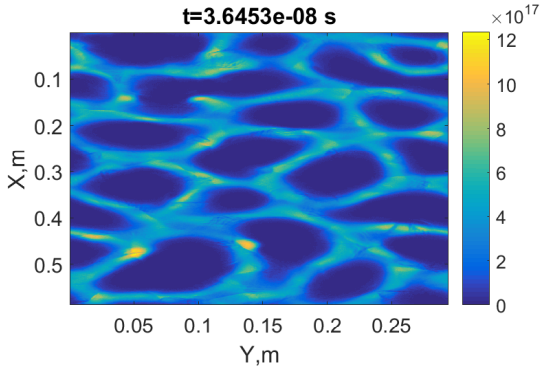

Back-ground electrons

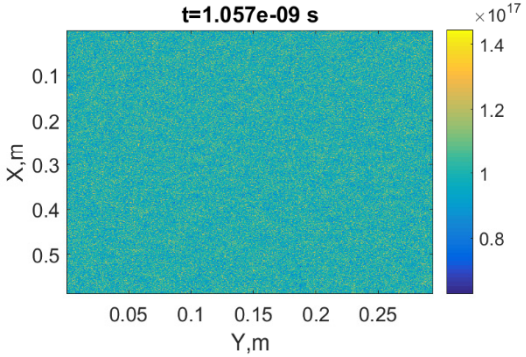

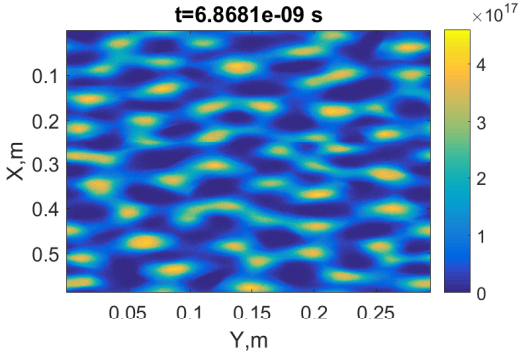

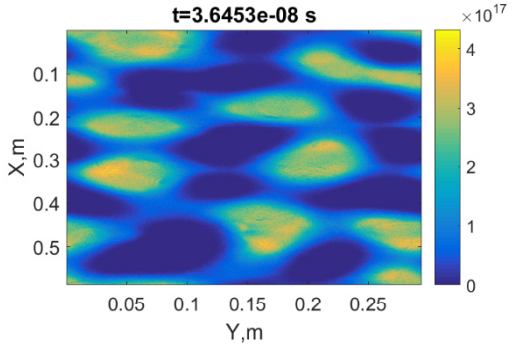

Beam electrons

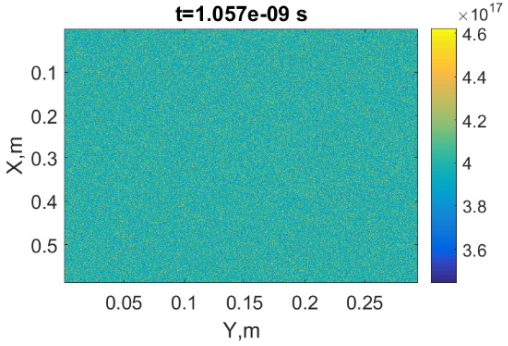

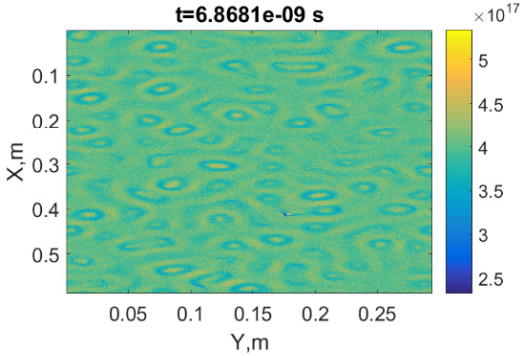

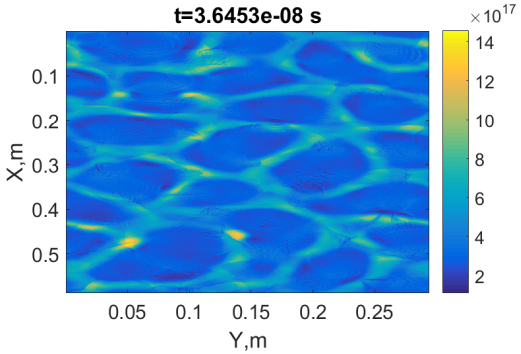

Total ions

Current filaments in the XY- and Z-geometries

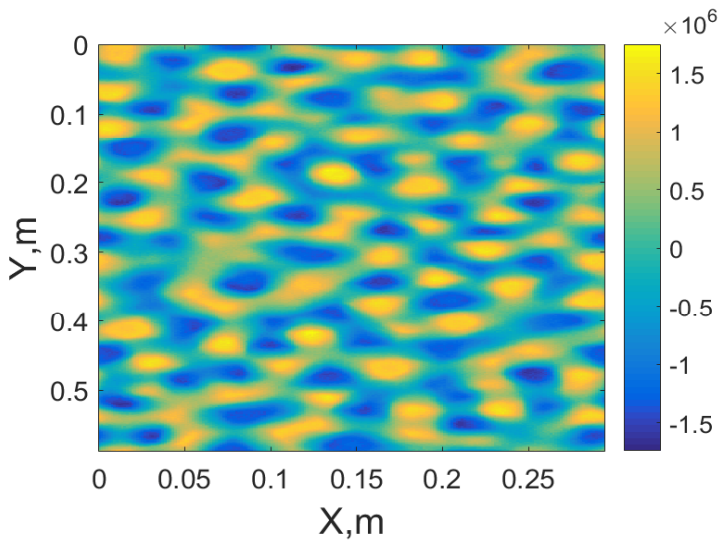

Fig. 1 Current density component Jz at the moment of time 5.2 ns without external field

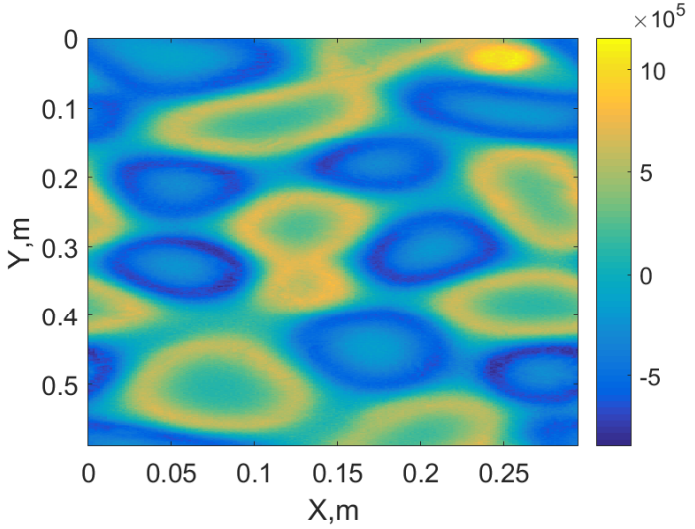

Z-geometry

Fig. 3 Current density component Jz at the moment of time 52 ns without external field

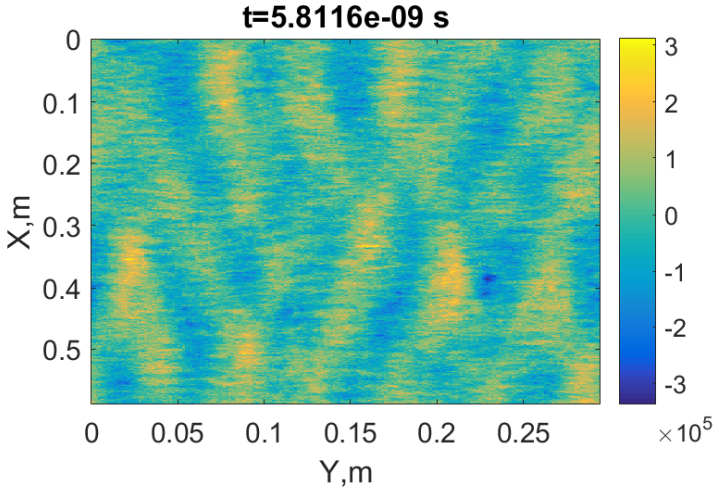

Fig. 2 Current density component Jx at the moment of time 5.8 ns without external field

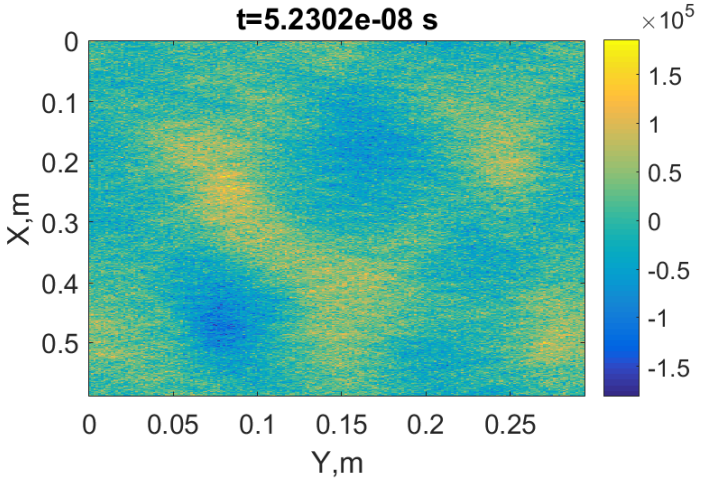

XY-geometry

Fig. 4 Current density component Jx at the moment of time 52 ns without external field

Evolution of the average magnetic field, the typical wavenumber and the anisotropy parameter

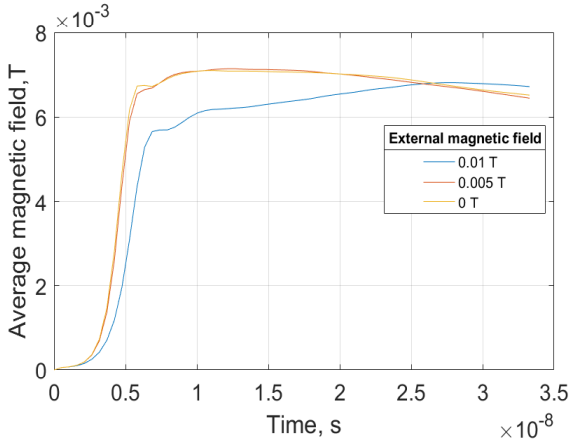

Fig. 1 Evolution of the average magnetic field in the presence of external magnetic field

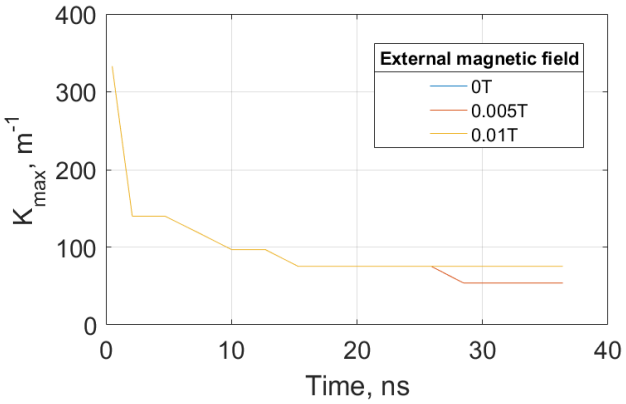

Fig. 2 Evolution of the wavenumber K_{max}

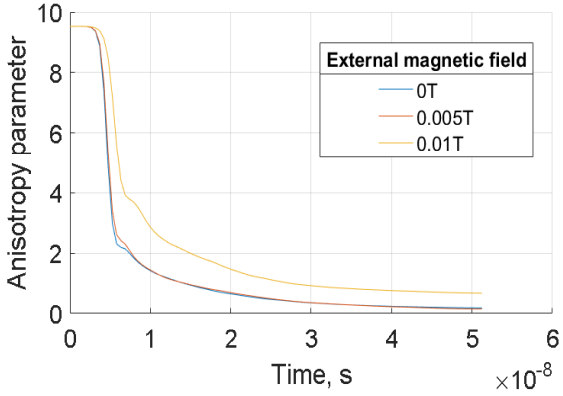

Fig. 3 Evolution of the anisotropy parameter

Analytical estimations and numerical calculations of the growth rate of the magnetic turbulence show close values (about $10^{10} s^{-1}$as per fig. 1). The value of the saturating magnetic field can be higher or of the same order as the value of the external field (see fig. 1). After saturation, a typical scale of the current filaments increases many times while the energy density of the turbulent magnetic field decays very slowly (see figs. 2 and 1). For a typical plasma density $\sim 10^{10} - 10^{12}\ cm^{-3}$ and a strength of magnetic field from tens to hundreds Gauss, a Weibel-instability scale can change from sub-meter to multiple meters. Anisotropy parameter significantly drops before the saturation and continues to decrease during the non-linear stage of the instability (fig. 3).

Density of various particles. Z-geometry. 10keV beam. 2*10^12 cm^-3 background plasma

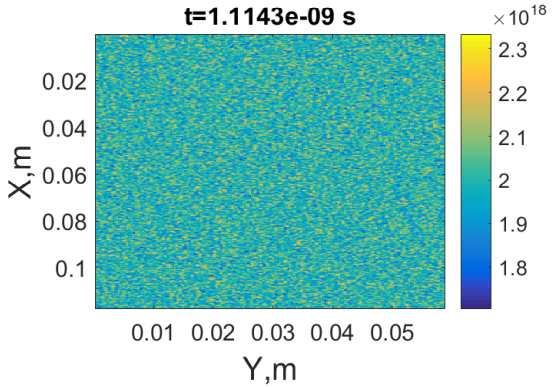

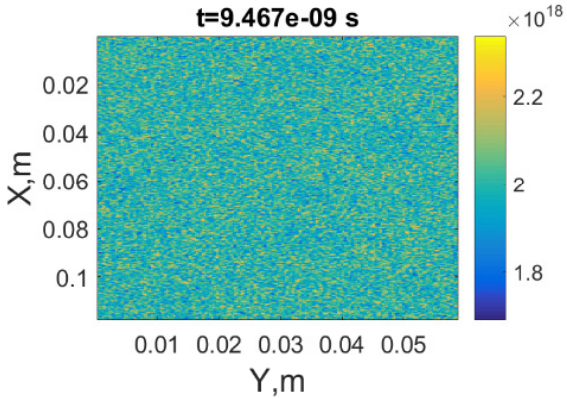

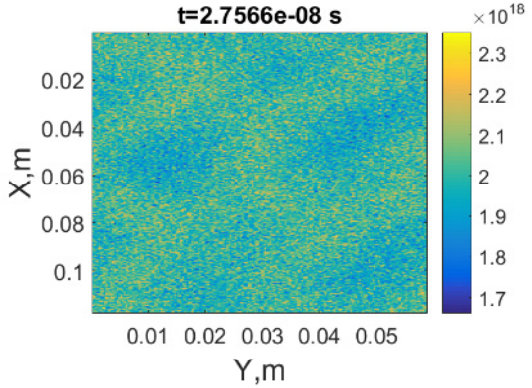

Background electrons

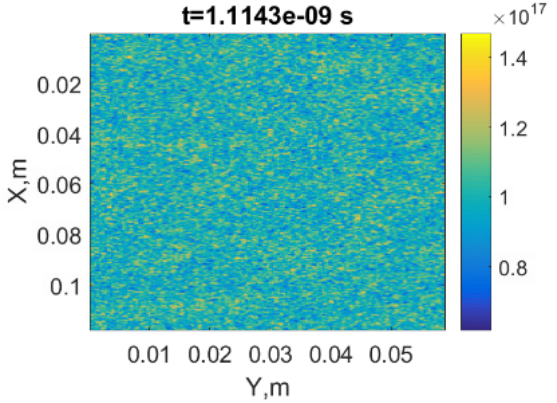

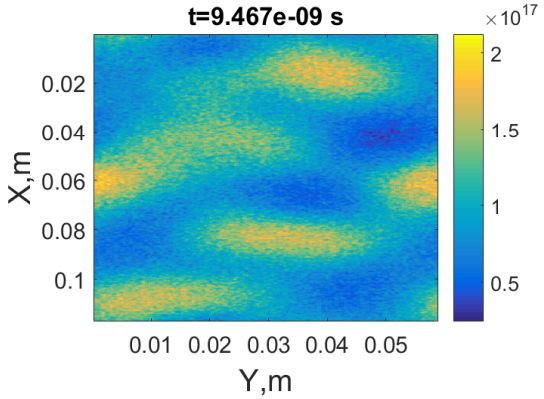

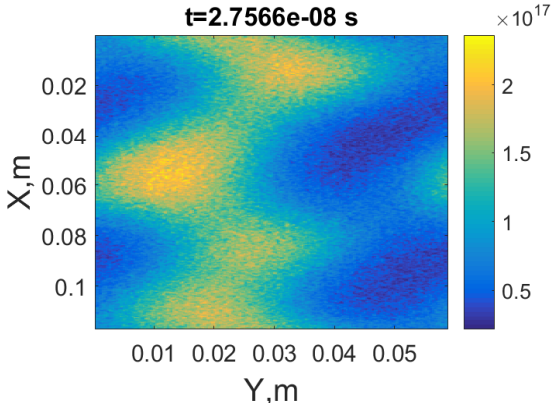

Beam electrons

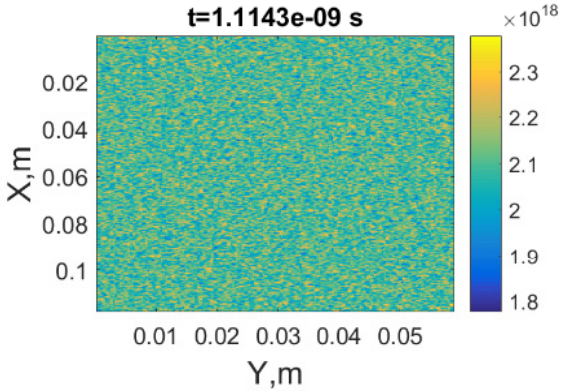

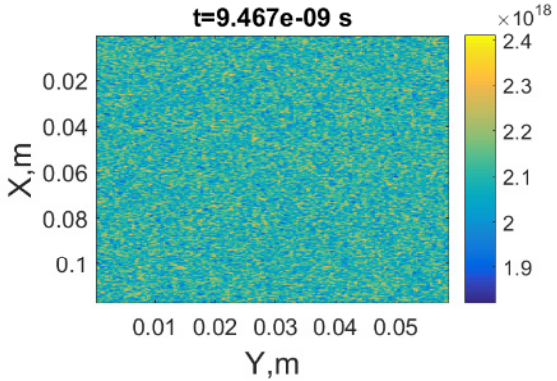

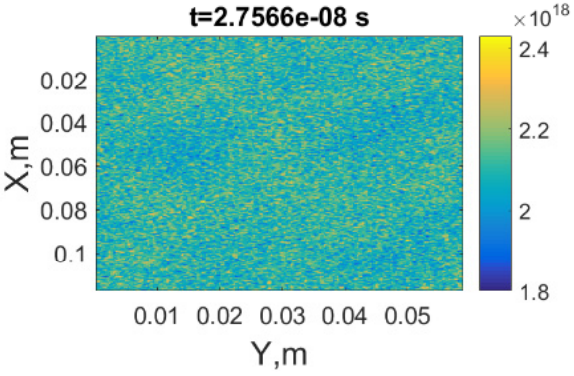

Total ions

Evolution of an average magnetic field and an anisotropy parameter. 2*10^12 cm^-3 background plasma. 10keV beam

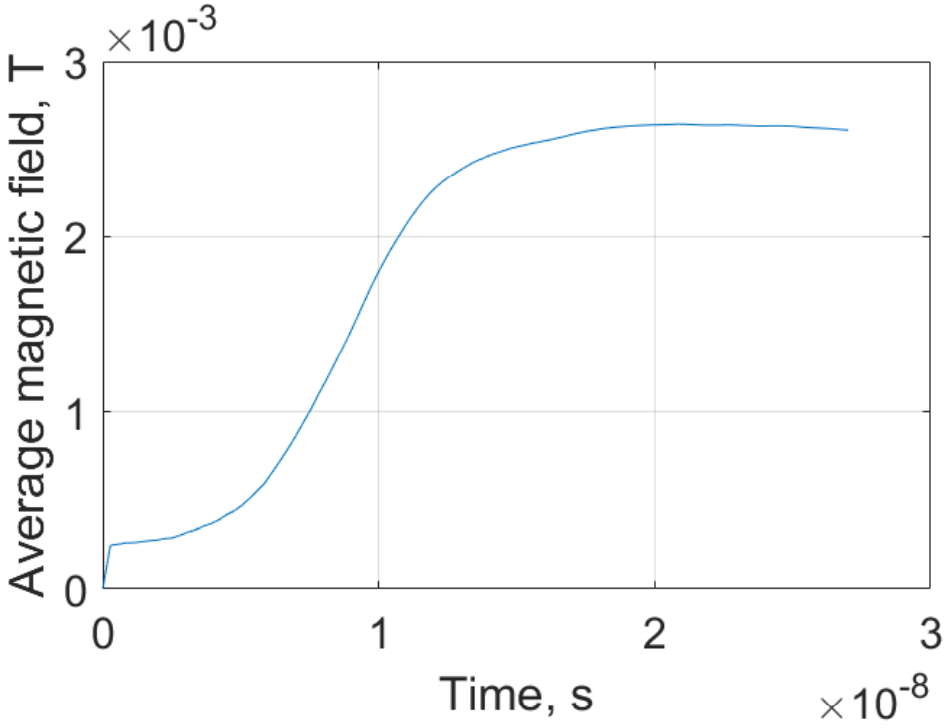

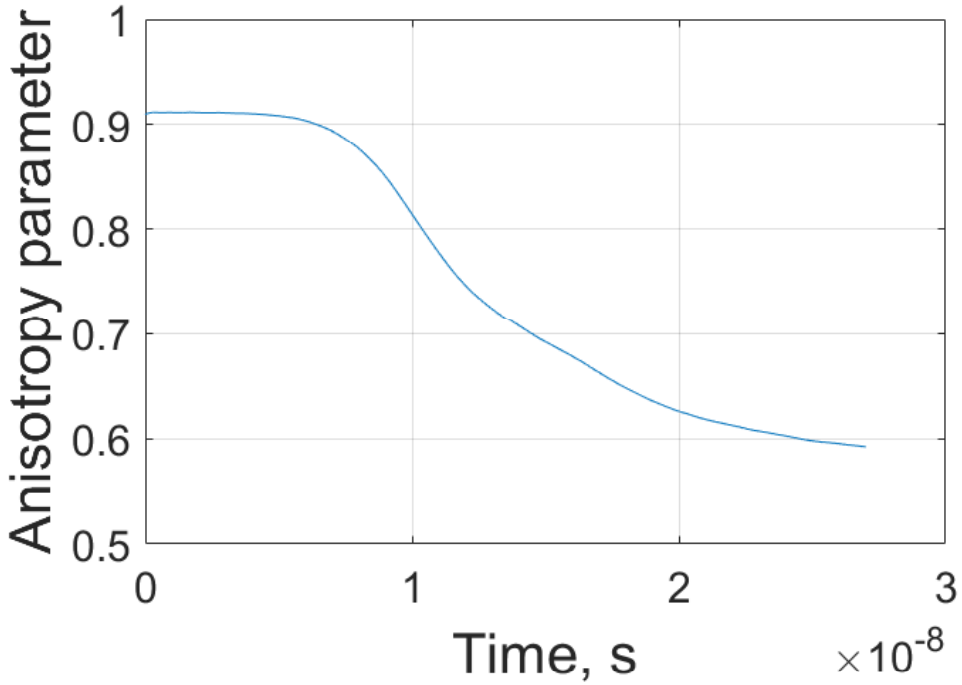

2D modeling on the basis of a harmonic decomposition

An original (quasi-linear) code for 2D modeling of the nonlinear development of the spatial harmonics of the Weibel TEM-instability described by the Maxwell-Vlasov equations is used. A number of their numerical solutions are found by the Leapfrog method for many hundreds of harmonics with wave vectors lying in the simulation plane XY transverse to the external magnetic field $\mathbf{B_0}$ and the anisotropy axis Z defined by the maximum effective particle temperature.

Perturbation technique based on weak nonlinearity of the problem leads to the following Eqs.

$$\frac{\partial \psi_0}{\partial \tau} + \sum_{n_x,n_y=1}^{m,s} \left(\hat{\Phi}(b_{K_\mathbf{n}}, \psi^*_{K_\mathbf{n}}) + \hat{\Phi}^*(b^*_{K_\mathbf{n}}, \psi_{K_\mathbf{n}}) \right) = 0,$$

$$\frac{\partial \psi_{K_\mathbf{n}}}{\partial \tau} + iK_{n_x}\beta_x\psi_{K_\mathbf{n}} + iK_{n_y}\beta_y\psi_{K_\mathbf{n}} + 2\hat{\Phi}(b_{K_\mathbf{n}}, \Psi(\mathbf{v}) + \psi_0) + \hat{\Phi}^*(b^*_{K_\mathbf{n}}, \psi_{2K_\mathbf{n}}) = 0,$$

$$\frac{\partial \psi_{2K_\mathbf{n}}}{\partial \tau} + 2iK_{n_x}\beta_x\psi_{2K_\mathbf{n}} + 2iK_{n_y}\beta_y\psi_{2K_\mathbf{n}} + \hat{\Phi}(b_{K_\mathbf{n}}, \psi_{K_\mathbf{n}}) = 0,$$

$$\frac{\partial b_{K_\mathbf{n}}}{\partial \tau} = -ie_{yK_\mathbf{n}}K_{n_x} + ie_{xK_\mathbf{n}}K_{n_y},$$

$$\frac{\partial e_{xK_\mathbf{n}}}{\partial \tau} = ib_{K_\mathbf{n}}K_{n_y} - \beta_\parallel^{-1} \iint_{-\infty}^{+\infty} \beta_x \psi_{K_\mathbf{n}}(\tau, \beta_x, \beta_y) d\beta_x d\beta_y.$$

$$b_{K_\mathbf{n}} = \frac{B_{K_\mathbf{n}}}{\sqrt{8\pi N T_\parallel}},\ T_\parallel = \frac{m_e c^2 \beta_\parallel^2}{2};\ \psi_{\ell \cdot K_\mathbf{n}} = \frac{c^2 f_{\ell \cdot K_\mathbf{n}}}{N},\ \ell = 0,\ 1,\ 2.$$

$$\frac{\partial e_{yK_\mathbf{n}}}{\partial \tau} = -ib_{K_\mathbf{n}}K_{n_x} + \beta_\parallel^{-1} \iint_{-\infty}^{+\infty} \beta_y \psi_{K_\mathbf{n}}(\tau, \beta_x, \beta_y) d\beta_x d\beta_y.$$

$$\hat{\Phi}(b_{K_n}, \psi(\beta)) = \frac{1}{2}e_{yK_\mathbf{n}}\frac{\partial \psi(\beta)}{\partial \beta_y} + \frac{1}{2}e_{xK_\mathbf{n}}\frac{\partial \psi(\beta)}{\partial \beta_x} - \frac{1}{2}b_{K_\mathbf{n}}\left(\beta_x\frac{\partial \psi(\beta)}{\partial \beta_y} - \beta_y\frac{\partial \psi(\beta)}{\partial \beta_x}\right)$$

Kuznetsov A.A. et al.
Plasma Physics Reports
2022, No. 6, in press.

2D modeling of the saturation phase by means of a harmonic decomposition

Parameters of the Leapfrog simulation of the Weibel (filamentation) instability in a background plasma are shown on the plots.

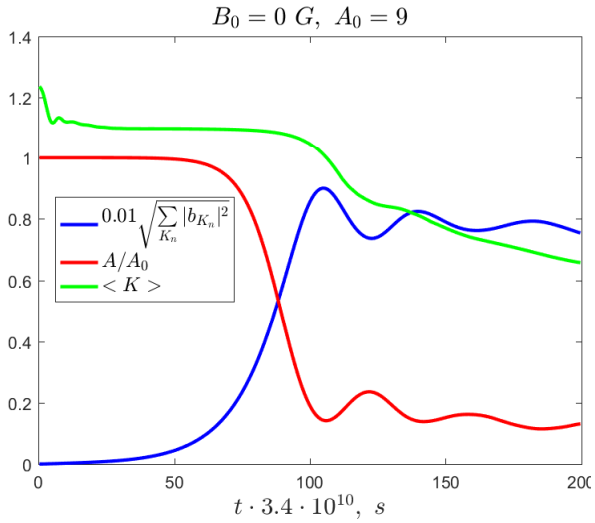

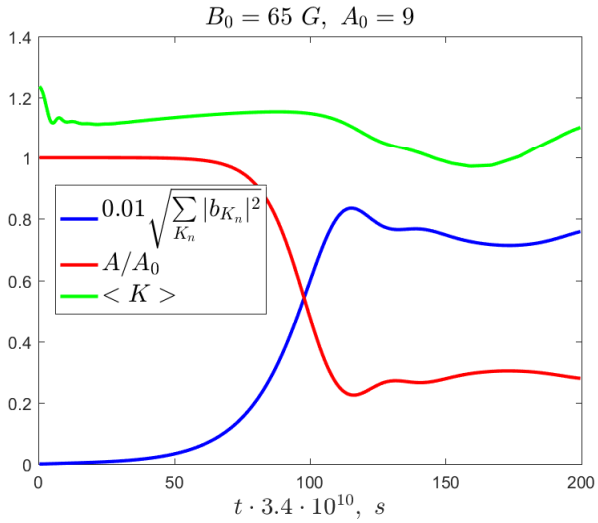

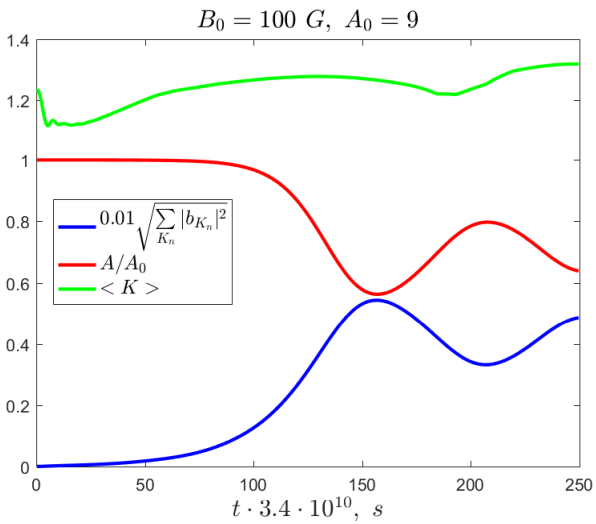

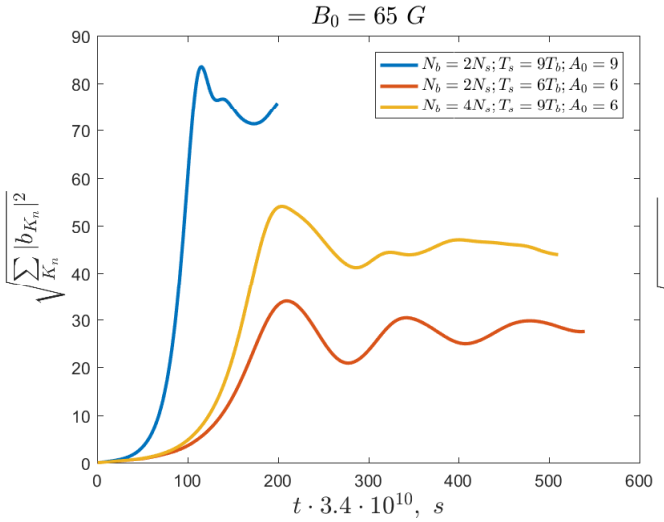

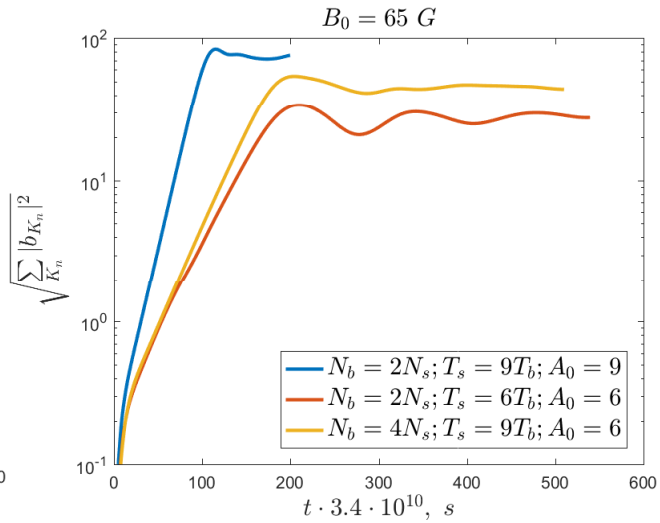

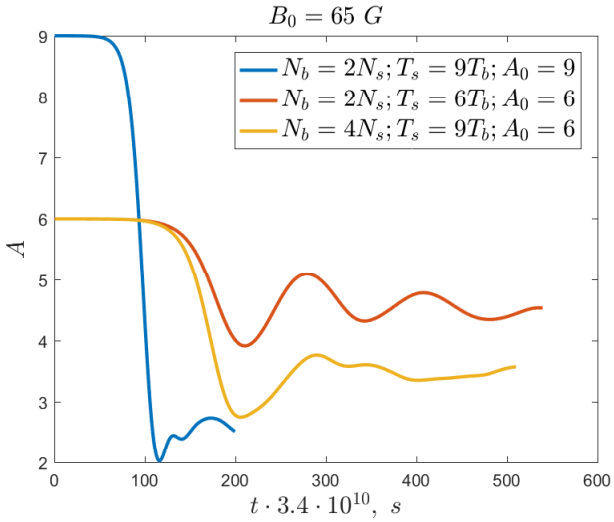

Conclusions on the problem # 5

1. We find a dependence of the Weibel growth rate on the electron anisotropy, temperature and density of plasma as well as on the strength of the external magnetic field and the value and orientation of a wave vector of a magnetic-field perturbation.
2. We estimate an intensity of a quasi-magnetostatic turbulence arising in an upper part of a coronal loop and prove that **a saturated small-scale magnetic field can be greater than or of the order of a typical magnetic field of the loop, thus leading to nanoflares.**
3. We argue that a strong X-ray flare, a small-scale reconnection of the magnetic-field lines, a partial destruction of the large-scale magnetic field, and even a coronal mass ejection are possible **if there is a sufficiently high degree of the electron anisotropy**.

Thus, the unveiled features of the Weibel (filamentation) instability process in the presence of an external magnetic field indicate the possibility of **the solar (stellar) flare to be initiated in an individual coronal loop**. As a result, in particular, a fast growth of the transverse particle temperature and a simultaneous strong decay of the plasma conductivity along the coronal magnetic field are expected. Also, an accompanying small-scale magnetic-field reconnection process and a turbulent ion flow will follow and lead to an imbalance of the magnetic-field and kinetic-plasma pressure.

However, a numerical analysis of such peculiarities of the long-term nonlinear stage of the Weibel instability in a magnetized collisionless plasma with a long enough and powerful injection of hot electrons into a region with a transverse size comparable to a coronal-loop diameter is still a challenging problem: today one can't describe up to 10^9 nanoflares.

General scenario of a flare from a coronal loop on the Sun and stars of late spectral classes

The injection of energetic (multi-keV) electrons into a rather cold (sub-keV) weakly collisional plasma is due to a strong quasi-static electric field directed along the loop and can be created, for example, at its base due to the photospheric-plasma motion or in the lower part of the loop due to the propagation of a powerful Alfvén wave.

Energetic electrons reach the rarefied upper part of the loop, and their **anisotropic velocity distribution leads to the Weibel (streaming) instability** producing small-scale (from meters to kilometers) current filaments (z-pinches) along the loop. As a result, a strong quasi-magnetostatic field directed mainly across the loop appears, the effective (anomalous) resistance of the plasma increases by several orders of magnitude, many synchronized nanoflares take place, a plasma is heated explosively, and a small-scale reconnection of magnetic field lines occurs. Thus, the balance between kinetic and magnetic pressures is disturbed, and a flare and a deformation of the large-scale magnetic field become possible. The mechanism can explain the phenomenon of **collective nanoflares and X-rays emission**.

We carry out the analytical estimates of the development of the linear stage and saturation of the Weibel-type instability for the characteristic parameters of plasma in the coronal loops of the Sun and stars of late spectral classes. For the optimal ranges of parameters of the background plasma, the magnetic field of the loop, and the flux of energetic electrons in it, we present typical results of modeling (by the particle-in-cell and harmonic-decomposition methods) of the long-term nonlinear development of this instability, leading to the X-ray flare from a single loop as well as to additional heating of the coronal plasma.

Discussion

We describe the development of anisotropic particle distributions and Weibel-type instabilities during the strong discontinuity decay in an inhomogeneous plasma. We illustrated the evolution of the current structures of different scales and the interaction between the self-generated and external fields, as well as the dynamics of the plasma during its penetration into the region of the strong external field and the expulsion of the plasma from regions of the strong self-generated field.

Particular attention was paid to the deformation of the particle distribution functions, e.g., by magnetic trapping, and the modification of the emerging plasma layers (shock waves) by the flow of hot electrons and the turbulent magnetic field created by them, as well as the formation of stratified plasma flows and current sheets or filaments, i.e., structures of reduced dimensionality, in the regions initially occupied by the magnetic field or without this field.

We focused on phenomena that can't be described within the MHD approximation, including the interplay between the electron and ion Weibel instabilities and the nonlinear evolution of the spatial spectrum of the self-generated quasi-magnetostatic turbulence.

The presented results of the study of the kinetic mechanisms of the creation of long-lived current structures supporting strong turbulent magnetic fields at various scales and modifying plasma flows could help to answer some open questions and determine the prospects for research in this field of plasma physics, astrophysics, and laser applications.

In particular, these results are important for the understanding the processes in the solar (stellar) flares and wind formation as well as the interaction of plasma clouds of different density, temperature and internal magnetic field.